NONLINEAR PHENOMENA INDUCED BY MILLIJOULE FEMTOSECOND LASER PULSES AT AN AIR-WATER INTERFACE

A Dissertation

by

BENJAMIN DAVID STRYCKER

Submitted to the Office of Graduate and Professional Studies of
Texas A&M University
in partial fulfillment of the requirements for the degree of

DOCTOR OF PHILOSOPHY

Chair of Committee,	Alexei Sokolov
Committee Members,	George Kattawar
	Aleksei Zheltikov
	Jaan Laane
Head of Department,	George Welch

December 2013

Major Subject: Applied Physics

ABSTRACT

Femtosecond laser pulses with millijoule energy have the potential to be used in many applications for remote sensing in marine environments. In this dissertation, we investigate some of the basic phenomena involved when a loosely focused, potentially filament-forming millijoule femtosecond laser pulse propagating in air interacts with an air-water interface.

As an introduction to the primary investigation, we discuss concepts and experiments relevant to the primary investigation: the interaction of millijoule femtosecond laser pulses with an air-water interface. We first discuss linear femtosecond pulse propagation in water and describe an experiment investigating pulse attenuation behavior in water in the linear pulse propagation regime. We find no deviations from exponential attenuation, in contradiction to some earlier works. We then discuss nonlinear pulse propagation in water and describe an experiment investigating the onset of nonlinear pulse propagation and spectral transformation in water. We find that nonlinear femtosecond pulse propagation begins at a peak pulse intensity of about 10^{10} W/cm^2. This experiment provides a convenient segway into the discussion and investigation of femtosecond laser filaments. We describe an experiment in which two filaments interact within liquid methanol and exchange energy. We then discuss laser-induced breakdown spectroscopy and demonstrate that different LIBS signal intensity thresholds can be utilized to image shallowly buried objects.

Finally, all of these concepts are brought together to discuss the interaction of millijoule femtosecond laser pulses with an air-water interface. We catalogue and describe the main phenomena involved, which span about 12 orders of magnitude in time. We then describe the characteristics of the acoustic shockwaves generated by this interaction and demonstrate the usefulness of millijoule femtosecond laser pulses in several remote sensing applications in marine environments.

DEDICATION

To my parents

ACKNOWLEDGEMENTS

I would like to thank the many people who made this dissertation possible and also to mention a few by name. First, I would like to thank the man who introduced me to Texas A&M University, Prof. George Kattawar. His warmth and open personality were the context within which I performed my early studies, and his enthusiasm for the mysteries of water was contagious and set me on my path of discovery. Second, I would like to thank Prof. Alexei Sokolov for his tireless patience in teaching me experimental optics. The many discussions we have had served to enlighten and deepen my understanding, foster my imagination, curb my recklessness, and guide my efforts. This dissertation is in many ways a direct result of the intellectual freedom given to me under his leadership. Both of these teachers, Prof. George Kattawar and Prof. Alexei Sokolov, taught me the art of asking relevant and poignant questions and the art of looking for enlightening and practical answers.

I would like to thank my lab-mates, who helped to make the research contained within this dissertation a reality. Foremost among these is Matthew Springer, whose expertise and kindness have been indispensable to me. His knowledge and keen insight have served to sharpen my ideas, while his kind and understanding manner have been very greatly appreciated.

Finally, I would like to thank my family for their love and support, without which, quite simply, this research would never have taken place.

TABLE OF CONTENTS

LIST OF FIGURES

FIGURE Page

FIGURE Page

CHAPTER I

INTRODUCTION

1.1 MOTIVATION AND OBJECTIVES

The applications of femtosecond laser pulse filaments are rapidly increasing. They have been used in remote filament-induced breakdown spectroscopy applications [1–3], as well as analyzing airborne biological materials [4]. Schemes for remote sensing in the atmosphere have been proposed [5]. Arrays of filaments are being considered as potential waveguides for long-distance radar and microwave propagation in the atmosphere [6,7]. These types of applications are becoming increasingly feasible as femtosecond lasers produce pulses with more and more energy.

To date, most applications utilizing femtosecond laser filaments have focused upon their uses in the atmosphere or in spectroscopic detection of land-based solid targets. However, femtosecond laser filaments also have the potential to be used in many marine environments, both in fresh and saltwater ecologies. We envision an air-based platform capable of delivering energetic femtosecond laser pulses to surface or subsurface targets using femtosecond laser filaments and retrieving the relevant information of interest remotely. Physical quantities of interest may include water temperature, salinity, and the presence of biological agents, toxins, or pollutants. It may also be possible to realize schemes for subsurface target detection. However, a system capable of retrieving such information has yet to be implemented.

In addition, the basic science of the interaction of a femtosecond laser filament propagating in air with a water surface is not yet completely understood. An understanding of the underlying physical processes that accompany air-borne femtosecond laser filament interaction with a water surface is prerequisite to developing relevant and potent applications for remote sensing in marine environments. It is the investigation of the interaction of potentially filament-forming pulses with a water surface that motivates this dissertation and guides its argument. It is to be hoped that the basic phenomena that are detailed in this work will provide the basis for an ongoing effort to bring femtosecond laser filaments into use in marine environments.

1.2 OUTLINE

This dissertation follows a logical argument in providing theoretical introductions and backgrounds to the complex phenomena involved in millijoule femtosecond laser pulse interaction with a water surface. Explanatory and introductory material is intended to provide an intuitive and fundamental understanding of the relevant material. As such, theoretical equations, illustrations, and figures are included toward this end. Where a more detailed discussion is warranted, relevant works are cited to provide the reader with a starting point in investigating the intricacies of a complex subject. Each chapter is accompanied by a research experiment involving the theoretical concepts previously outlined in the text. For each experiment, the author of this dissertation was a lead or co-author, and the work has been published or accepted for publication in a scientific journal.

Chapter II begins the theoretical introduction by detailing the basics of linear optics. Linear susceptibility is investigated from both a classical and quantum mechanical perspective. The relationship between the optical susceptibility of a medium and its refractive index is also investigated. The linear refractive index of liquid water is briefly discussed. Also, the basic properties and characteristics of ultrashort laser pulses are detailed for further use. Finally, an experiment investigating the linear propagation of femtosecond laser pulses through liquid water is described, in which a previous claim of having observed non-exponential absorption in the linear pulse propagation regime in water is refuted [8].

Chapter III builds upon the concepts introduced in Chapter II and goes further to provide a basic understanding of nonlinear optics. A quantum mechanical model of 2^{nd} and 3^{rd} order nonlinear susceptibility is outlined, and the relationship between nonlinear susceptibility and nonlinear refractive index is outlined. The nonlinear Schrödinger equation is introduced as a basic theoretical framework within which to investigate nonlinear pulse propagation through a medium. Major nonlinear phenomena involved in pulse propagation, such as self-phase modulation and self-steepening, are detailed. Finally, an experiment investigating the onset of nonlinear pulse propagation in liquid water is described [9].

Chapter IV continues to build upon the concepts outlined in the previous chapters in describing the phenomenon of pulse filamentation. A minimal definition of an optical filament is described in the first part of the chapter. Subsequent sections provide an intuitive theoretical understanding of important filamentation mechanisms such as pulse

self-focusing and ionization of the propagating medium. How these phenomena work together to produce a laser pulse filament is described. Finally, an experiment investigating energy exchange between two crossed filaments in liquid methanol is described [10].

Chapter V discusses the highly nonlinear phenomenon of laser pulse ablation of materials and laser-induced breakdown spectroscopy (LIBS). An experiment utilizing the different breakdown thresholds of materials is described in which shallowly buried objects are imaged with chemical specificity using their retrieved LIBS signals [11].

Finally, Chapter VI brings all the concepts and phenomena described in the previous chapters together to describe an experiment detailing the interaction of millijoule femtosecond laser pulses interacting with an air-water interface [12]. In this experiment, we outline the various phenomena that occur, which include plasma generation and subsequent LIBS signal emission, ablation, generation of shock waves, and, tens of microseconds after the initial pulse, the formation of a cavity and bubble in the water. This experiment can serve as a basis for further investigations into how potentially filament-forming femtosecond laser pulses can be used in marine environments for various remote sensing applications.

Chapter VII contains a summary and conclusion of the dissertation.

CHAPTER II

LINEAR OPTICS AND PULSE PROPAGATION*

2.1 MAXWELL'S EQUATIONS AND BASIC DEFINITIONS OF SUSCEPTIBILITY

Maxwell's Equations describe the relationship between electric and magnetic fields in vacuum and within various materials*. Maxwell's macroscopic equations, valid within bulk materials where the wavelength of radiation is much greater than the spacing between constituent particles, molecules, or atoms, are given as follows:

$$\nabla \cdot \vec{D} = \rho \tag{2.1}$$

$$\nabla \cdot \vec{B} = 0 \tag{2.2}$$

$$\nabla \times \vec{E} = -\frac{\partial \vec{B}}{\partial t} \tag{2.3}$$

$$\nabla \times \vec{H} = \vec{J} + \frac{\partial \vec{D}}{\partial t} \ , \tag{2.4}$$

where ρ is the charge density, $\vec{J}$ is the current density, $\vec{E}$ and $\vec{H}$ are the electric and magnetic fields, respectively, and $\vec{D}$ and $\vec{B}$ are the electric and magnetic flux densities, respectively. $\vec{D}$ and $\vec{B}$ are defined by the following relations:

$$\vec{D} = \varepsilon_0 \vec{E} + \vec{P} \tag{2.5}$$

---

* Reprinted with permission from "Propagation of femtosecond laser pulses through water in the linear absorption regime" by L. M. Naveira, B. D. Strycker, J. Wang, G. O. Ariunbold, A. V. Sokolov, and G. W. Kattawar, 2009. *Applied Optics*, 48, 1828-1836, Copyright 2009 by Optical Society of America.

$$\vec{B} = \mu_0 \left(\vec{H} + \vec{M} \right) , \tag{2.6}$$

where ε_0 and μ_0 are the permittivity and permeability of the vacuum, respectively. $\vec{P}$ and $\vec{M}$ are the polarization and magnetization densities, respectively, quantities which include the many contributions of the individual atoms and/or molecules. For example, the magnetization density $\vec{M}$ is defined by the relation

$$\vec{M} = \frac{1}{V} \sum_{i=1}^{N} \vec{m}_i \ , \tag{2.7}$$

where $\vec{m}$ is the magnetic moment of an individual atom or molecule in the sample, and V is the volume over which the summation is taken. While the magnetization includes the magnetic contributions from many microscopic and individual atoms and/or molecules, we may regard Maxwell's Equations within a bulk material as macroscopic, a type of "smoothing over" the many individual components to describe a cohesive whole (for an extended discussion of this property of the macroscopic Maxwell Equations, see Chapter 4 of [13]). This may be seen in the common practice of writing Eq. 2.6 in the form

$$\vec{B} = \mu_0 \left(1 + \chi_m \right) \vec{H} \ , \tag{2.8}$$

where the quantity χ_m is known as the *magnetic susceptibility*. Hence, we have defined the magnetization shown in Eq. 2.7 to be

$$\vec{M} = \chi_m \vec{H} \ . \tag{2.9}$$

Effectively, this type of definition ensures a macroscopic description of the magnetic flux density $\vec{B}$.

The same type of reasoning may be used to describe the relationship between the polarization density $\vec{P}$ and the electric field $\vec{E}$, where the many electric dipole moments of the individual atoms and/or molecules within a material medium add together to form a macroscopic response. The polarization density at a location specified by the vector $\vec{r}$ is given as

$$\vec{P}(\vec{r}) = \frac{1}{V}\sum_{i}^{N} q_i\left(\vec{r}_i - \vec{r}\right) \ , \tag{2.10}$$

where q_i is the charge located at position $\vec{r}_i$, and V is the volume of the sample. For a continuous charge distribution, Eq. 2.10 is commonly written as

$$\vec{P}(\vec{r}) = \frac{1}{V}\int_{V} \rho(\vec{r}_0 - \vec{r})\left(\vec{r}_0 - \vec{r}\right) d^3 r_0 \ , \tag{2.11}$$

where $\rho(\vec{r}_0)$ is the charge density at a location $\vec{r}_0$. An alternative definition of the polarization density is accomplished through writing Eq. 2.5 in the form

$$\vec{D} = \varepsilon_0\left(1 + \chi_e\right)\vec{E} \ , \tag{2.12}$$

where the quantity χ_e is known as the *electric susceptibility*. Eq. 2.12 effectively defines the polarization density as

$$\vec{P} = \varepsilon_0 \chi_e \vec{E} \ . \tag{2.13}$$

Eq. 2.13 is one of the key relations in what is known as *linear optics*.

2.2 ELECTROMAGNETIC WAVE EQUATION AND RELATIVE PERMITTIVITY

In describing the electromagnetic wave equation, we assume that within the material volume under consideration, the charge density ρ and the current density $\vec{J}$ are both zero, that is, there is no net charge or current density within the volume under consideration. Hence we may write Maxwell's Equations as

$$\nabla \cdot \vec{D} = 0 \tag{2.14}$$

$$\nabla \cdot \vec{B} = 0 \tag{2.15}$$

$$\nabla \times \vec{E} = -\frac{\partial \vec{B}}{\partial t} \tag{2.16}$$

$$\nabla \times \vec{H} = \frac{\partial \vec{D}}{\partial t} \ . \tag{2.17}$$

By taking the curl of Eq. 2.16, we get

$$\nabla \times \nabla \times \vec{E} = \nabla \times \left(-\frac{\partial \vec{B}}{\partial t} \right) . \tag{2.18}$$

We here utilize a vector identity for any vector quantity $\vec{A}$:

$$\nabla \times \nabla \times \vec{A} = \nabla \left(\nabla \cdot \vec{A} \right) - \nabla^2 \vec{A} \, . \tag{2.19}$$

We now rewrite Eq. 2.18 as

$$\nabla \left(\nabla \cdot \vec{E} \right) - \nabla^2 \vec{E} = \nabla \times \left(-\frac{\partial \vec{B}}{\partial t} \right) . \tag{2.20}$$

Similarly, the time derivative of Eq. 2.17 may be written

$$\nabla \times \left(\frac{\partial \vec{B}}{\partial t} \right) = \mu_0 \left(1 + \chi_m \right) \frac{\partial^2 \vec{D}}{\partial t^2} \ . \tag{2.21}$$

Since we know from Eq. 2.14 that $\nabla \cdot E = 0$, and substituting Eq. 2.21 into Eq. 2.20, we obtain the relation

$$\nabla^2 \vec{E} = \mu_0 \varepsilon_0 (1+\chi_m)(1+\chi_e)\frac{\partial^2 \vec{E}}{\partial t^2} \ , \tag{2.22}$$

which is the electromagnetic wave equation. In the case that both χ_m and χ_e are zero, i.e. when the wave propagates in vacuum, the speed of the propagating wave is governed by the permittivity and permeability of free space. The speed of light *c* in vacuum is then given by

$$c = \frac{1}{\sqrt{\mu_0 \varepsilon_0}} \ . \tag{2.23}$$

In the case when the wave propagates in a material medium, however, the speed of light is modified by a factor *n* known as the *refractive index*. The speed of light υ_p in the material for a particular wavelength is then given by

$$\upsilon_p = c / n \ , \tag{2.24}$$

where

$$n^2 = (1+\chi_m)(1+\chi_e) \ . \tag{2.25}$$

The quantity υ_p is known as the *phase velocity*, for reasons outlined later. Equation 2.25 is often written as

$$n^2 = \mu_r \varepsilon_r \ , \tag{2.26}$$

where

$$(1+\chi_m) \equiv \mu_r \tag{2.27}$$

$$\left(1+\chi_e\right) \equiv \varepsilon_r \ . \tag{2.28}$$

μ_r and ε_r are known as the *relative permeability* and *relative permittivity* of the medium, respectively. In most media, $\mu_r = 1$, so that the electromagnetic wave equation written in Eq. 2.22 can be written for a single wavelength as

$$\nabla^2 \vec{E} = \frac{n^2}{c^2}\frac{\partial^2 \vec{E}}{\partial t^2} = \frac{1}{\upsilon_p^2}\frac{\partial^2 \vec{E}}{\partial t^2} \ , \tag{2.29}$$

where υ_p is defined by Eq. 2.24 and the refractive index *n* by

$$n^2 = \varepsilon_r = \left(1+\chi_e\right) \ . \tag{2.30}$$

For the remainder of this dissertation, we will focus only on the electric relative permittivity and electric susceptibility, assuming that for all systems and materials under study, the relative magnetic permeability is $\mu_r = 1$. Henceforth, whenever susceptibility is mentioned, it is the electric susceptibility that is under consideration. We therefore refrain from including the *e* in the subscript and denote the electric susceptibility only as χ.

2.3 THE COMPLEX NATURE OF THE SUSCEPTIBILITY AND REFRACTIVE INDEX

The electric susceptibility of a material is, in general, a complex quantity which we denote as

$$\chi = \chi' + i\chi'' \ , \tag{2.31}$$

where χ' and χ'' are real quantities and

$$i = \sqrt{-1}\,. \tag{2.32}$$

The refractive index is, then, also a complex quantity since it is defined with relation to the susceptibility. It is common to denote the complex refractive index as $\tilde{n}$ and define it as

$$\tilde{n} = n + i\kappa \tag{2.33}$$

where n and κ are real quantities. We may relate the complex refractive index to the complex susceptibility through an extension of Eq. 2.30:

$$\tilde{n}^2 = n^2 + 2in\kappa - \kappa^2 = 1 + \chi' + i\chi''\,. \tag{2.34}$$

By equating the real and imaginary parts of the left and right sides of Eq. 2.34, we can relate the real and imaginary parts of the refractive index to the real and imaginary parts of the susceptibility:

$$n^2 - \kappa^2 = 1 + \chi' \tag{2.35}$$

$$2n\kappa = \chi''\,. \tag{2.36}$$

It is straightforward to show that, by substituting Eq. 2.36 into Eq. 2.35 and rearranging, the complex refractive index is related to the complex susceptibility in the following manner:

$$n = \sqrt{\frac{\sqrt{\left(1+\chi'\right)^2 + \chi''^2} + \left(1+\chi'\right)}{2}} \tag{2.37}$$

$$\kappa = \sqrt{\frac{\sqrt{\left(1+\chi'\right)^2 + \chi''^2} - \left(1+\chi'\right)}{2}}\,. \tag{2.38}$$

The physical nature of Eqs. 2.37 and 2.38 are seen in the solution to the electromagnetic wave equation as shown in Eq. 2.29. For an electromagnetic wave in one dimension propagating in the z-direction, The solution of Eq. 2.29 is of the form

$$E(z,t) = E_0 \exp\left[i\left(\omega t - kz + \phi\right)\right] + c.c. \ , \tag{2.39}$$

where E_0 is the initial amplitude, ω is the angular frequency of oscillation, k is the wavenumber, and ϕ is a constant phase. The angular frequency of oscillation is defined as

$$\omega = 2\pi f = \frac{2\pi c}{\lambda_0} \ , \tag{2.40}$$

where λ_0 is the wavelength of the electromagnetic wave in vacuum. The wavenumber is defined by the relation

$$k = \frac{\omega}{\upsilon_p} = \frac{\omega \tilde{n}}{c} = \frac{\omega\left(n + i\kappa\right)}{c} \ . \tag{2.41}$$

Substituting Eq. 2.41 into Eq. 2.39 yields the following result:

$$E(z,t) = E_0 \exp\left[-\frac{\omega\kappa}{c} \right] \exp\left[i\left(\omega t - \frac{\omega n}{c} z + \phi \right)\right] + c.c. \tag{2.42}$$

The exponential decay factor in Eq. 2.42 indicates the presence of attenuation through optical absorption. Hence the imaginary part κ of the complex refractive index $\tilde{n}$ of a medium is directly related to absorption, while the real part n of the complex refractive index $\tilde{n}$ is directly related to the speed of the electromagnetic wave in the medium, or the phase velocity υ_p as defined in Eq. 2.24. It is customary, when speaking about

attenuation and optical absorption, to define an absorption coefficient α with respect to attenuation of an optical intensity *I*, such that

$$I(z) = \frac{cn\varepsilon_0}{2} E(z,t)E^*(z,t) = I_0 \exp[-\alpha z] \ . \tag{2.43}$$

Here, the intensity I_0 is defined by

$$I_0 = \frac{cn\varepsilon_0}{2} |E(0,t)|^2 \ , \tag{2.44}$$

and the absorption coefficient α is given by

$$\alpha = \frac{2\omega\kappa}{c} \ . \tag{2.45}$$

It is interesting to note that should $\kappa = 0$, the absorption coefficient α would also be zero. It can be seen from Eq. 2.38 that the imaginary part κ of the complex refractive index $\tilde{n}$ is zero only when the imaginary part χ'' of the susceptibility χ is zero, i.e. $\kappa = 0$ only when $\chi'' = 0$. Hence we see that χ'' is responsible for optical absorption.

We note that in Eq. 2.45, the optical absorption coefficient $\alpha = \alpha(\omega)$, i.e. the optical absorption coefficient is a function of the frequency of the electromagnetic wave. The same is true about the complex refractive index $\tilde{n}$ as well as the complex susceptibility χ, although we keep in mind that $\tilde{n} = \tilde{n}(\omega)$ because $\chi = \chi(\omega)$. In the following sections, we shall see that the real part $\chi' = \chi'(\omega)$ and the imaginary part $\chi'' = \chi''(\omega)$ of the complex susceptibility are not independent; rather, they are related, and their relationship may be approximated by theoretical models.

2.4 CLASSICAL MODEL OF LINEAR SUSCEPTIBILITY: THE LORENTZ DIELECTRIC

The Lorentz model of light propagation through dielectric media is a classical linear model of light-matter interaction. In essence, it is a bridge between the atomic, albeit classical, interaction with light and the bulk macroscopic properties of a dielectric medium. It is named for H.A. Lorenz, a Dutch physicist who investigated these matters in the late 1800's and early 1900's [13–15]. In the Lorentz dielectric model, the various neutral atoms and/or molecules that make up the medium are pictured as stationary positively charged nuclei surrounded by bound and mobile electrons. The attraction of the electron to the nucleus is accounted for by modeling the force experienced by the electron as that of a harmonic oscillator, namely that the force is linearly proportional to the distance of the electron from the nucleus (Hooke's Law). A phenomenological damping ratio γ is included to account for optical absorption, and in essence the position $\vec{r}(t)$ of the electron with respect to the nucleus is sought as a function of time under the driving force of an incidence electric field $\vec{E}(t)$. The driving force $\vec{F}(t)$ experienced by the electron is then

$$\vec{F}(t) = -e\vec{E}(t) \ , \tag{2.46}$$

where -*e* is the charge of the electron. Consequently, the position of the electron with respect to the nucleus may be written as

$$m_e\left[\frac{d^2\vec{r}(t)}{dt^2} + 2\gamma\frac{d\vec{r}(t)}{dt} + \omega_0^2\vec{r}(t)\right] = -e\vec{E}(t)\,, \tag{2.47}$$

where $\omega_0^2 = k / m_e$ is the resonant undamped angular frequency of the oscillator, with k being the harmonic force constant.

Equation 2.47 may be solved easily in the frequency domain through a Fourier transformation. A Fourier transform from the time domain $f(t)$ to the frequency domain $f(\omega)$ is defined as [16]

$$f(\omega) = \int_{-\infty}^{\infty} f(t) \exp\left[-i\omega t\right] dt \ . \tag{2.48}$$

Applying Eq. 2.48 to the right side of Eq. 2.47 yields the quantity $e\vec{E}(\omega)$. The left side of Eq. 2.47 may be solved easily by assuming that the incident electric field $\vec{E}(t)$ is of the form

$$\vec{E}(t) = \vec{E}_0 \exp\left[-i\omega t\right] + c.c. \tag{2.49}$$

If this is the case, then the position of the electron must also be a function of this form:

$$\vec{r}(t) = \vec{r}_0 \exp\left[-i\left(\omega t + \phi\right)\right] + c.c. \tag{2.50}$$

where ϕ is a phase constant. We then see that the time derivative of the electron position is a simple constant frequency:

$$\frac{d\vec{r}(t)}{dt} = -i\omega\vec{r}(t) \ . \tag{2.51}$$

It is then straightforward to show that the Fourier transform of Eq. 2.47 from the time domain to the frequency domain results in the equation

$$m_e\left[-\omega^2 \vec{r}(\omega) - 2i\gamma\omega\,\vec{r}(\omega) + \omega_0^2 \vec{r}(\omega)\right] = e\vec{E}(\omega) \ . \tag{2.52}$$

Solving for the position of the electron as a function of frequency yields

$$\vec{r}(\omega) = \frac{e/m_e}{\omega_0^2 - \omega^2 - 2i\gamma\omega}\vec{E}(\omega) \ . \tag{2.53}$$

We may substitute Eq. 2.53 into Eq. 2.10, yielding a polarization density in a bulk medium of

$$\vec{P}(\omega) = \frac{1}{V}\sum_i^N e\vec{r}(\omega) = \frac{N}{V}\frac{e^2/m_e}{\omega_0^2 - \omega^2 - 2i\gamma\omega}\vec{E}(\omega) \ . \tag{2.54}$$

We recall from Eq. 2.13 that the polarization density can be written as $\vec{P}(\omega) = \varepsilon_0 \chi \vec{E}(\omega)$. We then see that in the Lorentz dielectric model, the susceptibility χ is a function of frequency and is of the form

$$\chi(\omega) = \frac{ne^2/\varepsilon_0 m_e}{\omega_0^2 - \omega^2 - 2i\gamma\omega} \ , \tag{2.55}$$

where $n = N/V$ is the number density per unit volume of oscillators in the medium. From the above equation, we see that the real and imaginary parts of the susceptibility $\chi(\omega) = \chi'(\omega) + i\chi''(\omega)$ are pictures of the same phenomenon, the real part $\chi'(\omega)$ describing the phase shift and the imaginary part $\chi''(\omega)$ describing the attenuation of a driven, damped harmonic oscillator:

$$\chi'(\omega) = \frac{ne^2}{\varepsilon_0 m_e}\frac{\left(\omega_0^2 - \omega^2\right)}{\left(\omega_0^2 - \omega^2\right)^2 + \left(2\gamma\omega\right)^2} \tag{2.56}$$

$$\chi''(\omega) = -\frac{ne^2}{\varepsilon_0 m_e}\frac{2\gamma\omega}{\left(\omega_0^2 - \omega^2\right)^2 + \left(2\gamma\omega\right)^2} \ . \tag{2.57}$$

Figure 2.1 shows the real and imaginary parts of the susceptibility, according to Eqs. 2.56 and 2.57, of a collection of oscillators having the number density of an ideal gas at atmospheric pressure and 20° C. The number density is 0.02504 cm^{-3}, while the resonant frequency is 2.3562 rad/fs, corresponding to a wavelength of 800 nm in vacuum. The damping ratio is $\gamma = \omega_0 / 100$. The shape of the two curves is characteristic of a susceptibility resonance. In later sections, it will be shown that the features of each curve have consequences in the characteristics of pulse propagation through a medium.

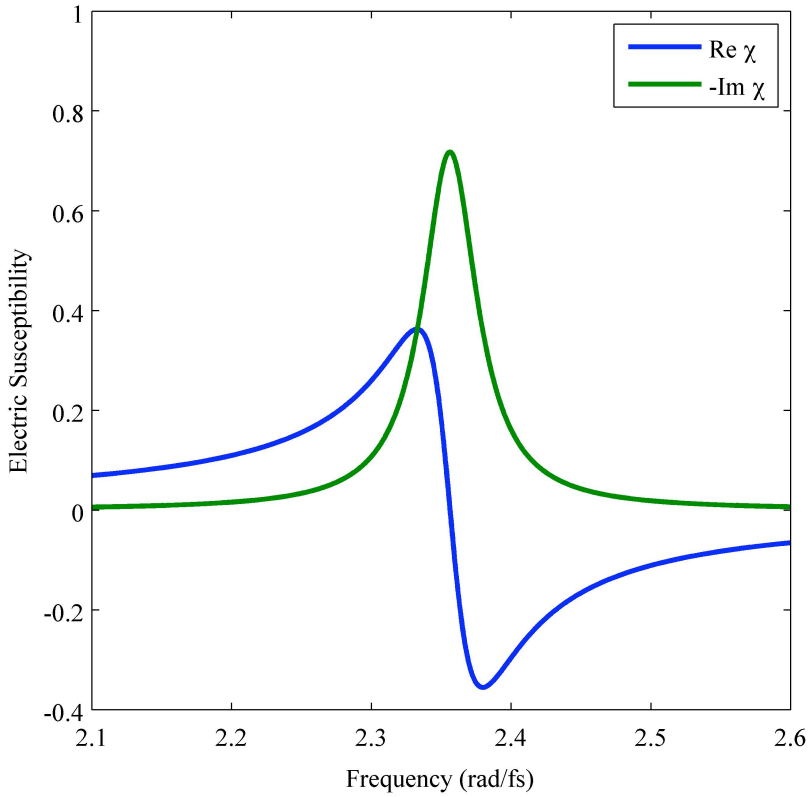

Fig. 2.1 Real and imaginary parts of the susceptibility of a Lorentz dielectric, according to Eqs. 2.56 and 2.57, having a number density of $n = 0.02504$ cm^{-3}, resonant frequency $\omega_0 = 2.3562$ rad/fs, and damping ratio $\gamma = \omega_0 / 100$.

The above equations outline the classical model for linear susceptibility. However, while real physical systems can often be approximated, sometimes to great accuracy, by classical models, physical systems are at the basic level quantum mechanical in nature. The following section outlines the quantum mechanical approach to linear susceptibility.

2.5 QUANTUM MECHANICAL MODEL OF LINEAR SUSCEPTIBILITY: SEMICLASSICAL APPROXIMATION

The semiclassical approximation, atomic systems are treated quantum mechanically while electromagnetic fields are treated classically [17]. The semiclassical model is very often sufficient to describe and predict many interesting optical phenomena involved in light-matter interaction [18], although a more rigorous and fully quantum mechanical model is needed to describe such phenomena as spontaneous emission between two atomic levels in atoms [17]. In the following section, we look at the semiclassical description of linear susceptibility. In particular, we consider linear susceptibility from the perspective of perturbations of atomic wave functions. While this model is accurate only for a non-resonant response of the light-matter interaction, it has the advantage of presenting a more intuitive physical insight. A more rigorous calculation of linear susceptibility must utilize the density matrix formalism, which takes account of the uncertainty in the wavefunction due to interaction processes in atomic and molecular ensembles. A good discussion of the density matrix formalism is found in [17,18]. For our purposes, however, the atomic wavefunction perturbation theory

will suffice to provide an intuitive physical insight into the origin of susceptibility in a quantum mechanical system.

We begin with the fundamental assumption of quantum mechanics that an atomic system may be fully described by its atomic wavefunction $\psi(\vec{r},t)$. The atomic wavefunction is a solution to the time-dependent Schrödinger equation

$$i\hbar\frac{\partial\psi}{\partial t}=\hat{H}\psi \ , \tag{2.58}$$

where $\hbar$ is the Dirac constant and the Hamiltonian operator $\hat{H}$ is given by

$$\hat{H}=\hat{H}_0+\hat{V}(t) \ , \tag{2.59}$$

with $\hat{H}_0$ corresponding to the Hamiltonian for the free atom and $\hat{V}(t)$ describing the interaction Hamiltonian. We take the interaction Hamiltonian to be

$$\hat{V}(t)=-\hat{\vec{\mu}}\cdot\vec{E}(t) \ , \tag{2.60}$$

where we follow Boyd's [18] nomenclature in describing the electric dipole operator

$$\hat{\vec{\mu}}=-e\vec{r} \ . \tag{2.61}$$

We recall that the energy eigenstates of the unperturbed Hamiltonian operator $\hat{H}_0$ constitute a complete, orthonormal basis set in terms of which any atomic state may be expanded [19]. These eigenstates have the form

$$\psi_n(\vec{r},t)=u_n(\vec{r})\exp\left[-i\omega_n t\right] \ , \tag{2.62}$$

where $\omega_n=E_n/\hbar$, with E_n denoting the energy of the *n*th eigenstate solution. The orthonormality of the eigenstates is described mathematically through the equation

$$\int u_m^* u_n \, d^3r=\delta_{mn} \ . \tag{2.63}$$

In perturbation theory, we replace the Hamiltonian in Eq. 2.59 with

$$\hat{H} = \hat{H}_0 + \lambda \hat{V}(t) \ , \tag{2.64}$$

where λ is a continuous parameter ranging between zero and one and describes the strength of the interaction between the electromagnetic field and the atomic system. We now seek a solution to Eq. 2.58 of the form

$$\psi(\vec{r},t) = \psi^{(0)}(\vec{r},t) + \lambda\psi^{(1)}(\vec{r},t) + \lambda^2\psi^{(2)}(\vec{r},t) + ... \tag{2.65}$$

Substituting this solution into Eq. 2.58 and requiring that all terms proportional to λ^N satisfy the equation separately yields

$$i\hbar\frac{\partial\psi^{(0)}}{\partial t} = \hat{H}_0\psi^{(0)} \tag{2.66}$$

$$i\hbar\frac{\partial\psi^{(N)}}{\partial t} = \hat{H}_0\psi^{(N)} + \hat{V}\psi^{(N-1)} \ , \tag{2.67}$$

where $N = 1,2,3...$ Equation 2.66 has a solution of the form

$$\psi^{(0)}(\vec{r},t) = u_g(\vec{r})\exp\left[-iE_g t/\hbar\right] \ , \tag{2.68}$$

where g denotes the ground state of the atom. In solving Eq. 2.67, we make use of the fact that any atomic state may be expanded in terms of the unperturbed energy eigenfunctions of the form in Eq. 2.62. Hence we may write the solution to Eq. 2.67 as

$$\psi^{(N)}(\vec{r},t) = \sum_l a_l^{(N)}(t)u_l(\vec{r})\exp\left[-i\omega_n t\right] \ , \tag{2.69}$$

where $a_l^{(N)}(t)$ is the probability amplitude that the atom is found in energy eigenstate l at time t. By substituting Eq. 2.69 into Eq. 2.67, we find the relation between probability amplitudes of orders *N* and *N*-1:

$$i\hbar\sum_l \dot{a}_l^{(N)} u_l(\vec{r})\exp\left[-i\omega_l t\right] = \sum_l a_l^{(N-1)} \hat{V} u_l(\vec{r})\exp\left[-i\omega_l t\right] \ . \tag{2.70}$$

The above equation can be simplified by multiplying each side of Eq. 2.70 by u_m^* and integrating, utilizing the orthonormality of the eigenfunctions. This yields

$$\dot{a}_m^{(N)}(t) = \frac{1}{i\hbar}\sum_l a_l^{(N-1)}(t) V_{ml}(t)\exp\left[i\omega_{ml} t\right] \ , \tag{2.71}$$

where

$$V_{ml} \equiv \left\langle u_m \middle| \hat{V} \middle| u_l \right\rangle = \int u_m^* \hat{V} u_l \, d^3 r \tag{2.72}$$

and

$$\omega_{ml} \equiv \omega_m - \omega_l \ . \tag{2.73}$$

Equation 2.71 may be rewritten in the form

$$a_m^{(N)}(t) = \frac{1}{i\hbar}\sum_l \int_{-\infty}^{t} V_{ml}(t') a_l^{(N-1)}(t')\exp\left[i\omega_{ml} t'\right] dt' \ . \tag{2.74}$$

The utility of Eq. 2.74 is evident in the fact that, if one knows the probability amplitudes of order N-1, the probability amplitudes of order N may also be calculated.

In order to calculate the linear susceptibility using the atomic wavefunction perturbation method, we assume that to zeroth order, the atom is in the ground state. Mathematically speaking, this corresponds to setting

$$a_l^{(0)} = \delta_{gl} \ . \tag{2.75}$$

We also represent the incident electric field $\vec{E}(t)$ as a sum of positive and negative frequency plane waves:

$$\vec{E}(t) = \sum_p \vec{E}(\omega_p)\exp\left[-i\omega_p t\right] \ . \tag{2.76}$$

We now substitute Eqs. 2.76 and 2.75 into Eq. 2.74, assuming that the contribution from the lower limit in the integral vanishes, yielding

$$a_m^{(1)} = \frac{1}{\hbar}\sum_p \frac{\vec{\mu}_{mg}\cdot\vec{E}(\omega_p)}{\omega_{mg}-\omega_p}\exp\left[i\left(\omega_{mg}-\omega_p\right)t\right] , \tag{2.77}$$

where the electric dipole transition moment $\vec{\mu}_{ml}$ is given by

$$\vec{\mu}_{ml} = \int u_m^* \hat{\vec{\mu}}\, u_l \, d^3r \ . \tag{2.78}$$

Equation 2.77 may be used to calculate the linear susceptibility in the following manner. The expectation value of the electric dipole moment $\langle \vec{p} \rangle$ is given by

$$\langle \vec{p} \rangle = \langle \psi | \hat{\vec{\mu}} | \psi \rangle \ . \tag{2.79}$$

We recall that we seek a solution ψ in powers of λ according to Eq. 2.65. This means that the first order contribution to the electric dipole moment (which is linear in the applied electric field) is of the form

$$\langle \vec{p}^{(1)} \rangle = \langle \psi^{(0)} | \hat{\vec{\mu}} | \psi^{(1)} \rangle + \langle \psi^{(1)} | \hat{\vec{\mu}} | \psi^{(0)} \rangle \ . \tag{2.80}$$

We recall that $\psi^{(0)}$ and $\psi^{(1)}$ are given by Eqs. 2.68 and 2.69, respectively. Hence we find that the first order contribution to the electric dipole moment is

$$\langle \vec{p}^{(1)} \rangle = \frac{1}{\hbar}\sum_p \sum_m \left(\frac{\vec{\mu}_{gm}\left(\vec{\mu}_{mg}\cdot\vec{E}(\omega_p)\right)}{\omega_{mg}-\omega_p}\exp\left[-i\omega_p t\right] + \frac{\left(\vec{\mu}_{mg}\cdot\vec{E}(\omega_p)\right)^* \vec{\mu}_{mg}}{\omega_{mg}-\omega_p}\exp\left[i\omega_p t\right] \right) . \tag{2.81}$$

The linear polarization density $\vec{P}^{(1)} = n\langle \vec{p}^{(1)} \rangle$, where *n* is the number density per unit volume. Since in Eq. 2.81 the summation is over all frequencies both positive and

negative, we may replace ω_p with $-\omega_p$: the value of the summation remains the same. Also, recalling that

$$P_i^{(1)}(\omega_p) = \varepsilon_0 \sum_j \chi_{ij}^{(1)} E_j(\omega_p) \ , \tag{2.82}$$

we see that the linear susceptibility is given by

$$\chi_{ij}^{(1)} = \frac{N}{\varepsilon_0 \hbar} \sum_m \left(\frac{\mu_{gm}^i \mu_{mg}^j}{\omega_{mg} - \omega_p} + \frac{\mu_{gm}^j \mu_{mg}^i}{\omega_{mg} + \omega_p} \right) . \tag{2.83}$$

The first term on the right side of Eq. 2.83 is called the resonant term, while the second term on the right side of the equation is called the anti-resonant term. It is often customary to ignore the anti-resonant term near resonance, as the value of the susceptibility is primarily determined by the resonant term. However, the linear susceptibility as shown in Eq. 2.83 is only valid near but off resonance. Directly on resonance, the susceptibility as described by Eq. 2.83 is infinite; this is unrealistic and unphysical. One solution to this problem that is often utilized is the inclusion of a phenomenological damping constant [18]; interestingly, even in the density matrix formalism, the damping constant remains phenomenological. It is included in the present model by modifying the transition frequency ω_{mg} from Eq. 2.73 to

$$\omega_{mg} = \left(E_m - E_g \right) / \hbar - i\gamma_m \tag{2.84}$$

where γ_m is taken as a decay rate of level m. Strictly speaking, the inclusion of such a phenomenological parameter using the method in Eq. 2.84 cannot describe population cascades among excited states nor dephasing processes. However, for many purposes it

remains a reasonable and not too inaccurate inclusion of damping affects. This is the case for our purposes here.

In substituting Eq. 2.84 into Eqs. 2.81 and 2.83, it is necessary to remember that in the anti-resonant term, the complex conjugate of the transition frequency of Eq. 2.84 is required. This is easily done, and the result is

$$\chi_{ij}^{(1)} = \frac{N}{\varepsilon_0 \hbar} \sum_m \left(\frac{\mu_{gm}^i \mu_{mg}^j}{\left(\omega_{mg} - \omega_p\right) - i\gamma_m} + \frac{\mu_{gm}^j \mu_{mg}^i}{\left(\omega_{mg} + \omega_p\right) + i\gamma_m} \right) . \tag{2.85}$$

The linear susceptibility in the form of Eq. 2.85 is already in a similar form to the Lorentz dielectric model of the previous section. However, we will show how, for an isotropic medium, the linear susceptibility is essentially identical to a Lorentzian dielectric. In an isotropic medium, the polarization density vector $\vec{P}$ is parallel to the electric field $\vec{E}$, and therefore the susceptibility is a scalar quantity. Because, on average, only 1/3 of the dipole transition moments will be oriented along the electric field an contribute to the susceptibility, we may write the susceptibility as

$$\chi^{(1)} = \frac{N}{\varepsilon_0 \hbar} \sum_m \frac{1}{3} \left|\vec{\mu}_{mg}\right|^2 \left(\frac{1}{\left(\omega_{mg} - \omega\right) - i\gamma_m / 2} + \frac{1}{\left(\omega_{mg} + \omega\right) + i\gamma_m / 2} \right) , \tag{2.86}$$

where, in addition to dropping the indices on $\chi^{(1)}$ due to its scalar quality, we have dropped the indices on the electric field frequency ω. We here introduce an oscillator strength f_{mg} defined as

$$f_{mg} = \frac{2m\omega_{mg} \left|\vec{\mu}_{mg}\right|^2}{3\hbar e^2} . \tag{2.87}$$

The oscillator strength obeys a sum rule

$$\sum_m f_{mg} = 1 \ , \tag{2.88}$$

such that it functions as an indicator of the strength of a particular transition in relation to all other transitions in the atomic system. Including the oscillator strength according to Eq. 2.87 in the equation for the susceptibility yields

$$\begin{aligned} \chi^{(1)} &= \sum_m \frac{N f_{mg} e^2}{2\varepsilon_0 m_e \omega_{mg}} \frac{1}{\left(\omega_{mg} - \omega\right) - i\gamma_m} + \frac{1}{\left(\omega_{mg} + \omega\right) + i\gamma_m} \\ &\simeq \sum_m f_{mg} \left[\frac{N e^2 / \varepsilon_0 m_e}{\left(\omega_{mg}^2 - \omega^2\right) - 2i\omega_{mg}\gamma_m} \right] \end{aligned} \ . \tag{2.89}$$

The lower expression for susceptibility in Eq. 2.89 is identical in form to the classical Lorentz dielectric susceptibility shown in Eq. 2.55, except for the fact that in Eq. 2.89 multiple resonances are accounted for, the strength of each being given by the oscillator strength parameter f_{mg}. Thus we see that, in certain systems, even a (semiclassical) quantum mechanical description of susceptibility can reproduce a Lorentzian resonance in the susceptibility. In the following section, we will discuss the refractive index of liquid water and how the simplified models of susceptibility outlined above are not adequate to describe it.

2.6 THE REFRACTIVE INDEX OF LIQUID WATER

In the previous sections, we outlined simple models of dielectric susceptibility in an attempt to provide an intuitive physical picture of the relationship between the real and imaginary parts of the susceptibility. In the laboratory and in theoretical models, however, it is often more convenient to investigate the material response to an incident

light field in terms of the complex refractive index $\tilde{n} = n + i\kappa$, as n and κ are parameters that are more accessible within the solutions to the electromagnetic wave equation, as shown in Eq. 2.42. We recall that the real and imaginary parts of the susceptibility are related to the real and imaginary parts of the refractive index through Eqs. 2.37 and 2.38. Figure 2.2 shows the real and imaginary parts of the refractive index calculated from the susceptibility shown in Fig. 2.1, which was calculated using the Lorentz dielectric model. The overall shape of the curves is preserved, and this type of behavior remains characteristic of a resonance.

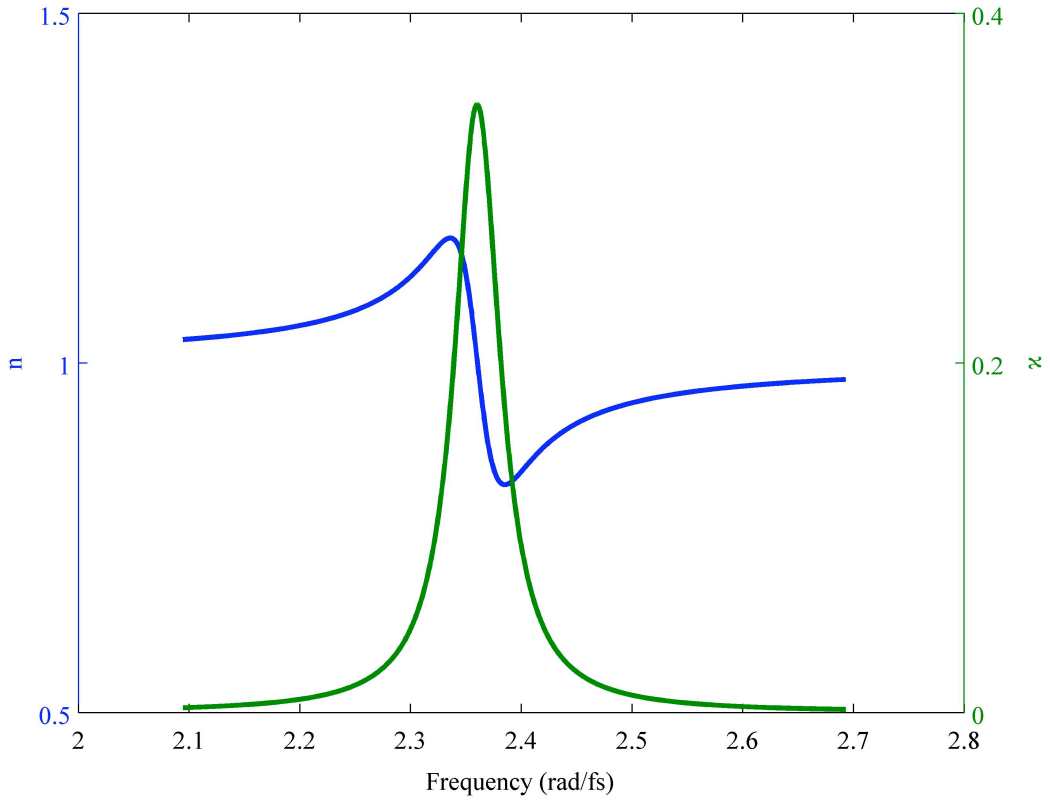

Fig. 2.2 Real and imaginary parts of the refractive index of a Lorentz dielectric, calculated using the susceptibility shown in Fig. 2.1.

This type of behavior, however, while valid for some systems, remains insufficient to describe the behavior of liquid water. Liquid water, while composed of a collection of the relatively simple H_2O molecule, is a highly complex network of strong hydrogen bonds that to this day is not fully understood [20]. Needless to say, while the refractive index of water does exhibit resonances of the water molecule, the intermolecular interactions due to hydrogen bonding has, so far, defied a purely theoretical description of the refractive index. Consequently, most models are empirical fits to experimental data. A review of several empirical models for the refractive index of liquid water is found in [21].

The measurement of the refractive index of water has an interesting history. While a complete history and review of all the measurements and publications that have appeared in the literature is beyond the scope of this dissertation, we point out that perhaps the most useful measurements of the refractive index have been made by Segelstein [22], Kou *et al*. [23], and Pope and Fry [24]. Pope and Fry have achieved the most accurate measurements of the absorption coefficient of water to date through use of integrating cavity technology [25]. While the data for the complex refractive index of water presented by Kou *et al*. is somewhat more accurate than Segelstein's measurements near 800 nm [8], Segelstein presents data over a broader range of wavelengths. A graph of Segelstein's data is shown in Fig. 2.3.

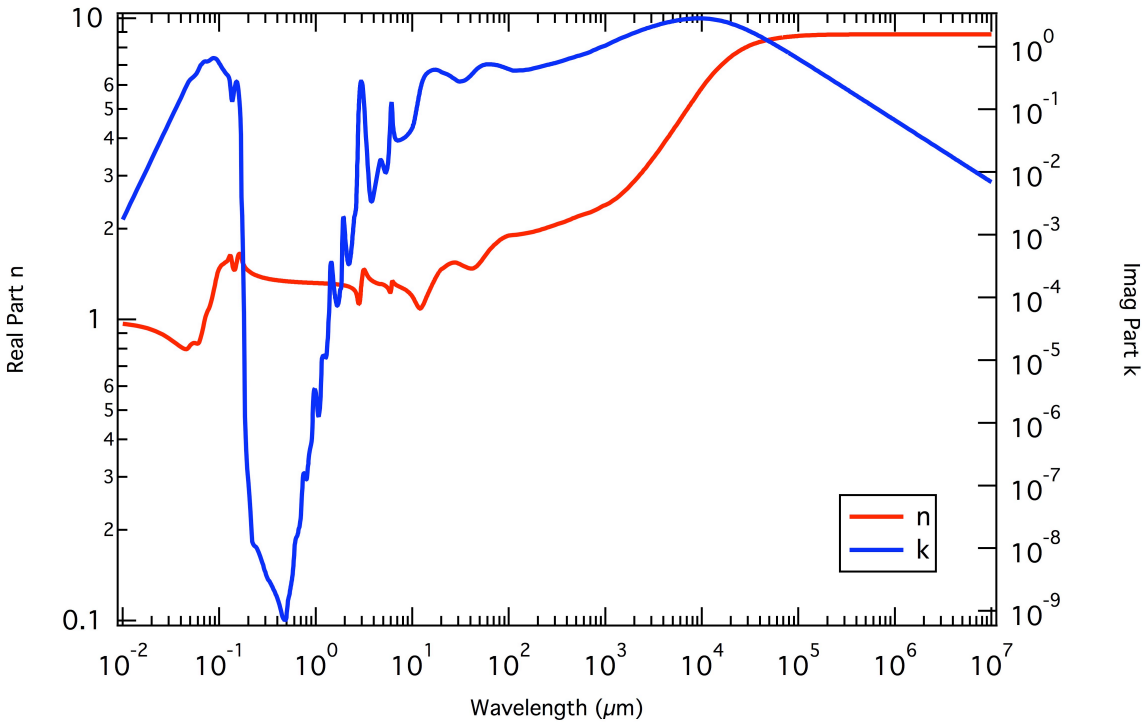

Fig. 2.3 Real and imaginary parts of the refractive index of liquid water as measured by Segelstein [22].

The data present several resonances in addition to an overall more complex behavior. The resonances are due to the vibrational modes of the water molecule; it is interesting that combinations of vibrational modes can also be extracted from the data [24].

In the past three sections, we have shown that the complex susceptibility and refractive index of a material are a function of the frequency of incident radiation. This has dramatic consequences in the behavior of laser pulse propagation through these media. In the following section, we review some of the basics of laser pulses and laser pulse propagation through dispersive media.

2.7 BASICS OF ULTRASHORT PULSES

We first consider the electromagnetic wave equation of Eq. 2.29. Assuming that the electric field propagates in the z-direction and is pointed along the x- or y-axis, we can write the electromagnetic wave equation as

$$\frac{\partial^2 E}{\partial z^2} - \frac{n^2(\omega)}{c^2}\frac{\partial^2 E}{\partial t^2} = 0 \ . \tag{2.90}$$

It is straightforward to show that

$$E(z,t) = \int E_0(\omega)\exp\left[-ik(\omega)z - i\omega t + i\phi\right]d\omega \tag{2.91}$$

is a solution to Eq. 2.90, where ϕ is phase constant independent of frequency. This is the principle of superposition: in linear optics, electric field plane waves of varying frequencies and amplitudes satisfy the electromagnetic wave equation individually. The total solution is the summation of all the solutions of each frequency component. We point out that, at $z = 0$, Eq. 2.91 is written as

$$E(0,t) = \exp\left[-i\phi\right]\int E_0(\omega)\exp\left[-i\omega t\right]d\omega \ , \tag{2.92}$$

which we recognize as a Fourier transform. The temporal behavior of the pulse at $z = 0$ is determined by the spectrum of the pulse $E_0(\omega)$ in the frequency domain. For ultrashort laser pulses, the frequency spectrum is often Gaussian in shape [26]:

$$E_0(\omega) = \frac{1}{\sqrt{2\pi}}\exp\left[-\frac{(\omega-\omega_0)^2\tau_0^2}{8\ln 2}\right], \tag{2.93}$$

where ω_0 is the central frequency, or carrier frequency, of the pulse and τ_0 is the intensity full width at half maximum (FWHM) of the pulse. The factor 8 ln 2 in the

denominator of the exponent in Eq. 2.93 is conventional for describing the temporal duration of the pulse with the intensity FWHM. Substituting Eq. 2.93 into Eq. 2.92 results in a temporal waveform of

$$E(0,t) = \exp\left[-\frac{(2\ln 2)t^2}{\tau_0^2}\right]\exp\left[-i\omega_0 t - i\phi\right], \tag{2.94}$$

whose intensity is

$$I(0,t) = \left|E(0,t)E(0,t)^*\right| = \exp\left[-\frac{(4\ln 2)t^2}{\tau_0^2}\right], \tag{2.95}$$

where τ_0 is, again, the intensity FWHM duration of the pulse. For $z \neq 0$, however, we must take account of the dependence of the wavenumber on frequency. We recall that

$$k(\omega) = \frac{\omega \tilde{n}(\omega)}{c}, \tag{2.96}$$

where $\tilde{n}(\omega)$ is the complex refractive index as a function frequency. In order to take account of the frequency dependence of the wavenumber, it is common practice to expand the frequency-dependent phase terms on the right side of Eq. 2.91 in Taylor series centered around ω_0:

$$ik(\omega)z - i\omega t = ik(\omega_0)z - i\omega_0 t + \left[i\left.\frac{dk}{d\omega}\right|_{\omega_0} z - it\right](\omega - \omega_0) + \frac{1}{2}\left[i\left.\frac{d^2k}{d\omega^2}\right|_{\omega_0} z\right](\omega - \omega_0)^2 + \ldots \tag{2.97}$$

We follow the nomenclature of [27] and let

$$\beta_n = \left.\frac{d^n k}{d\omega^n}\right|_{\omega_0} . \tag{2.98}$$

We note that

$$\beta_1 = \upsilon_g^{-1} , \tag{2.99}$$

where υ_g is known as the *group velocity*. The group velocity is the speed at which energy travels through the medium. It is also important to note that the phase velocity, as defined by Eq. 2.24, is in general not equivalent to the group velocity. Another important quantity is

$$\beta_2 = \left.\frac{d^2 k}{d\omega^2}\right|_{\omega_0} . \tag{2.100}$$

This quantity is important because it contains information about the type of *temporal dispersion* the laser pulse experiences in the propagating medium. The term "temporal dispersion" refers to the fact that different frequencies may propagate with different speeds through a particular medium, resulting in temporal evolution (an increase or decrease in the temporal duration) of the pulse. The following relationships contain information regarding the type of dispersion in a medium:

$$\begin{aligned} \beta_2 = \left.\frac{d^2 k}{d\omega^2}\right|_{\omega_0} > 0 \qquad & \textit{normal dispersion} \\ \beta_2 = \left.\frac{d^2 k}{d\omega^2}\right|_{\omega_0} < 0 \qquad & \textit{anomalous dispersion} \end{aligned} . \tag{2.101}$$

Normal and anomalous dispersion are also known as positive and negative dispersion, respectively. In normal dispersion, the group velocity decreases as frequency increases. In anomalous dispersion, the group velocity increases as frequency increases.

We can gain some insight into the characteristic of an ultrashort pulse that has propagated a distance z in a dispersive medium by substituting a pulse with Gaussian spectrum like Eq. 2.93 with expanded wavenumber according to Eq. 2.97 into Eq. 2.91 and integrating. This yields a pulse with temporal behavior

$$E(z,t)=\frac{e^{-i\phi}}{\sqrt{\frac{2\tau_0^2}{\gamma}-iz\beta_2}}\exp\left[-\frac{\gamma}{4}\frac{\left(t-\beta_1 z\right)^2}{\tau_0^2+\left(\frac{\gamma\beta_2}{2\tau_0}\right)^2 z^2}\right] \times\exp\left[i\left(k(\omega_0)z-\omega_0 t\right)+i\frac{2\gamma^2\beta_2 z\left(t^2+2zt\beta_1-z^2\beta_1^2\right)}{\left(4\tau_0^2\right)^2+\left(2\gamma z\beta_2\right)^2}\right], \qquad (2.102)$$

where we have let $\gamma=8\ln 2$. Many useful insights can be gained from the expression in Eq. 2.102. We first point out that the numerator in the top exponential is of the form $t-\beta_1 z$, meaning that the electromagnetic wave is a Gaussian pulse that travels at velocity $\upsilon_g=\beta_1^{-1}$. The denominator of the top exponential shows the effects of dispersion upon the pulse duration as it propagates, as a result of different frequencies possessing different group velocities. The intensity FWHM pulse duration $\tau(z)$ as a function of propagation distance z is then

$$\tau(z)=\sqrt{\tau_0^2+\left(\frac{\gamma\beta_2}{2\tau_0}\right)^2 z^2}\ . \qquad (2.103)$$

Because we have assumed in the above analysis that the pulse is transform limited at $z = 0$, the pulse duration only increases as the pulse propagates, regardless of the sign of β_2.

Another important parameter that can be gleaned from Eq. 2.102 is the *pulse chirp*. Pulse chirp describes how the frequency of oscillation of the pulse develops through time. For a pulse with zero chirp, the frequency of oscillation remains constant. However, for a pulse with positive or negative chirp, the frequency of oscillation increases or decreases as a function of time, respectively. In Eq. 2.102, if we say that the oscillation of the electric field has the form $i\omega t$, we can see that the frequency ω has the form

$$\omega = a + bt , \tag{2.104}$$

where a and b are, in general, functions of the propagation distance z. The sign of the parameter b in Eq. 2.104 is determined, in Eq. 2.102, by the sign of the parameter β_2, so that positive and negative dispersion results in positive and negative pulse chirp, respectively, as the pulse propagates through a dispersive medium.

We point out that these phenomena, namely increase in pulse duration and the development of pulse chirp, are individual aspects of the same effect. As the pulse gains chirp, it also spreads out in time. This results in a third effect, the decrease in maximum pulse amplitude as a function of propagation distance through a dispersive medium (having assumed a transform-limited pulse at $z = 0$). This can be seen in the denominator of the multiplicative prefactor in Eq. 2.102.

It is interesting to note that pulse chirp results in a quadratic phase relationship as a function of frequency in the frequency domain, as can be seen in Eq. 2.97. A linear phase relationship merely results in propagation of a transform limited pulse. Because we have truncated Eq. 2.97 after the quadratic terms, we have omitted spectral phase relationships that are cubic and quartic functions of the frequency. In general, these cubic and quartic spectral phase components also result in contributions to the pulse chirp. In practice, however, it is often reasonably sufficient to consider only the quadratic spectral phase contribution to the pulse chirp.

Having reviewed the basic characteristics of susceptibility, refractive index in water, and characteristics of ultrashort pulse propagation in a dispersive medium, we now describe an experiment investigating the propagation of ultrashort pulses of water in the linear regime.

2.8 PROPAGATION OF FEMTOSECOND LASER PULSES THROUGH WATER IN THE LINEAR ABSORPTION REGIME

2.8.1 Controversy over optical precursors in water

Optical precursors are a linear phenomenon resulting from ultrashort pulse propagation through a dispersive medium. The conditions under which optical precursors form were first described theoretically by Arnold Sommerfeld and Leon Brillouin in 1914 [28]. Their results were later refined by Oughstun and Sherman [29]. In order for optical precursors to form, the frequency spectrum of the ultrashort pulse

must span a resonance in the refractive index of the medium through which the pulse propagates. Shown in Figure 2.4 is the frequency spectrum of an ultrashort pulse spanning a resonance in the refractive index of a dispersive medium. The complex refractive index is calculated from a susceptibility of the form

$$\chi(\omega) = \frac{A}{\omega_0^2 - \omega^2 - 2i\gamma\omega} \quad , \tag{2.105}$$

where $A = 0.01\ fs^{-2}$, $\omega_0 = 2.3562\ fs^{-1}$, and $\rho = 0.008\ fs^{-1}$.

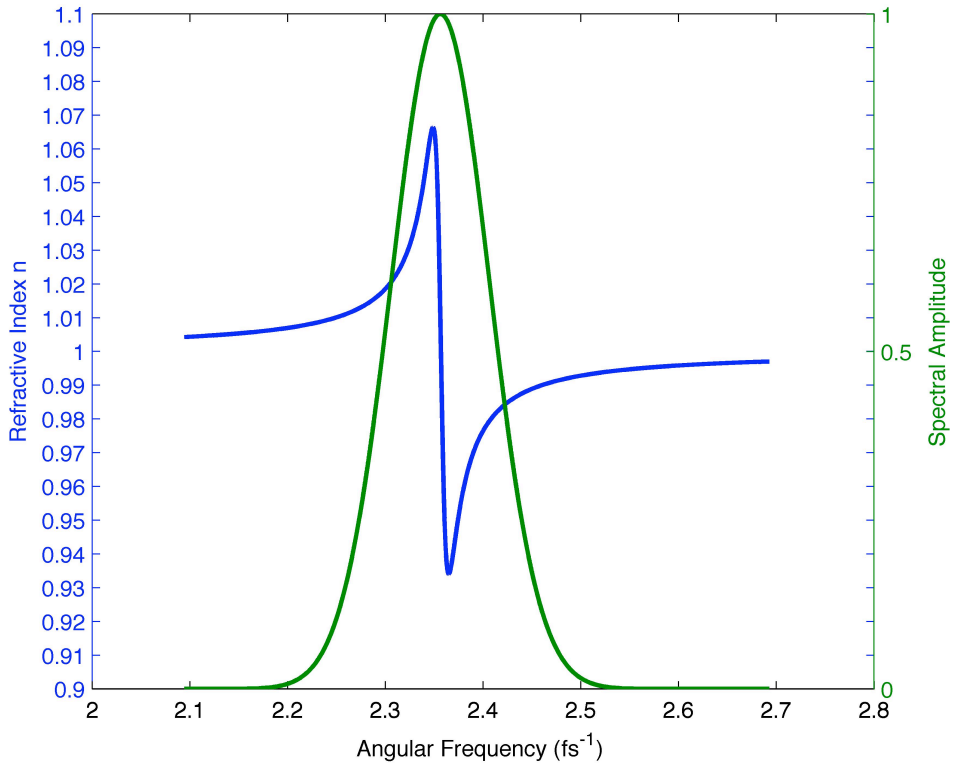

Fig. 2.4 Frequency spectrum of an ultrashort pulse that spans a resonance in the refractive index *n*. Only the real part of the refractive index is shown.

We point out that the above parameters most likely do not represent a real physical medium. However, they are amenable to the calculation at hand and lend themselves to our illustrative purposes. The pulse experiences normal dispersion for low and high frequencies; however, the resonance in the refractive index centered at the carrier frequency of the pulse results in a region of anomalous dispersion for the central frequency of the pulse. Consequently, after propagation through a certain distance z through the medium, the pulse begins to split into smaller sub-pulses, some which propagate faster or slower than the main body of the pulse. This is demonstrated in Figure 2.5, which shows the temporal form of the pulse, in the frame traveling with the pulse, whose spectrum is shown in Figure 2.4 after a propagation distance of 0.02 nm in the medium.

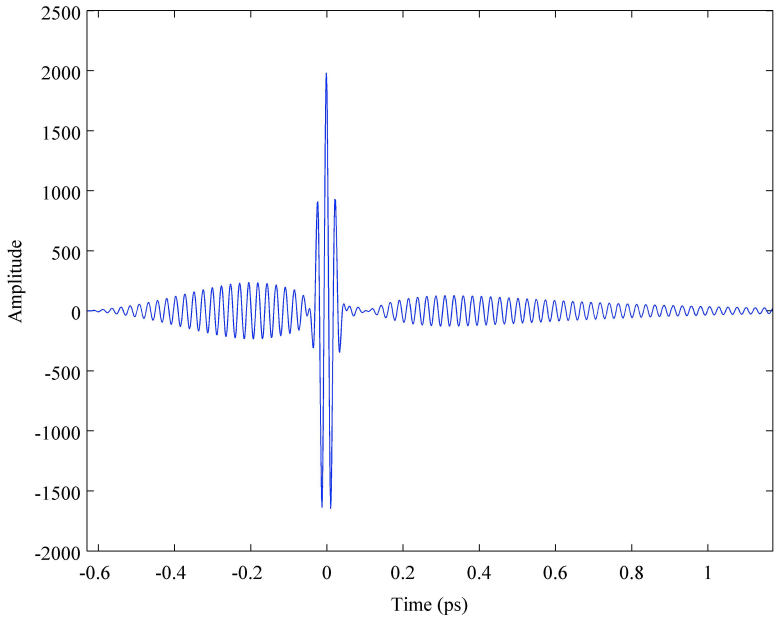

Fig. 2.5 Temporal behavior of the pulse whose spectrum is given in Fig. 2.4 after propagating 0.02 nm in the medium whose susceptibility is given by Eq. 2.105, with reference to the frame traveling with the pulse. The main pulse (middle) has split into several subpulses which propagate faster and slower than the main pulse.

The main body of the pulse (shown in the middle of the Figure 2.5) has split into several subpulses that travel faster and slower than the main pulse. The pulses that travel faster are known as *precursors*. Precursors of frequency higher than the central frequency of the pulse are known as Sommerfeld precursors, while precursors having a frequency less than that of the central frequency of the pulse are known as Brillouin precursors [28].

Beginning in 2004 through early 2009, a controversy over a claim of observed precursors in water was addressed by various works in the literature [8]. The controversy began with a paper by Choi and Österberg [30] in which they claimed to have observed non-exponentially attenuated 60 fs pulses in water. Their results were, however, questioned by Alfano *et al*. [31] and Roberts [32]. In another paper, Fox and Österberg [33] claimed to again have seen non-exponential attenuation of 60 fs laser pulses. This conclusion was again asserted in a paper by Gibson and Österberg [34]. However, subsequent experiments to reproduce the results of Österberg were undertaken by Li *et al.* [35] and Okawachi *et al.* [36], in which they witnessed no violation of the expected exponential attenuation of radiation after laser pulse propagation through several meters of water.

We note that the exponential attenuation of electromagnetic radiation in dispersive media is known as the Bouguer-Lambert-Beer (BLB) law and is of the form

$$I(z) = I_0 \exp[-\alpha(\omega)z] \ , \tag{2.106}$$

where $I(z)$ is the optical intensity and $\alpha(\omega)$ is the absorption coefficient given by Eq. 2.45. It is valid on a single frequency basis, that is, each individual frequency in a laser pulse spectrum satisfies the BLB law separately.

Claims that the BLB law are violated in water in the linear propagation regime have been shown to be false through the experiment outlined in the following subsections.

2.8.2 Experimental setup to resolve controversy

In our experiment, we measure the frequency-resolved transmission of a laser pulse through a propagation distance in water of varying length, thereby retrieving the absorption coefficient. With such a setup, it is possible to determine whether any deviations from the linear BLB law have occurred.

We use a Ti:sapphire-based laser system consisting of an oscillator (Mira, Coherent: 800 nm center wavelength, 80 nm FWHM bandwidth, 500 mW average power, 76 MHz repetition rate) and an amplifier (Legend, Coherent: 35 fs pulse duration, 1kHz repetition rate, 1 mJ pulse energy). Such pulse characteristics closely resemble the experimental conditions of previous works. An experimental schematic is shown in Fig. 2.6.

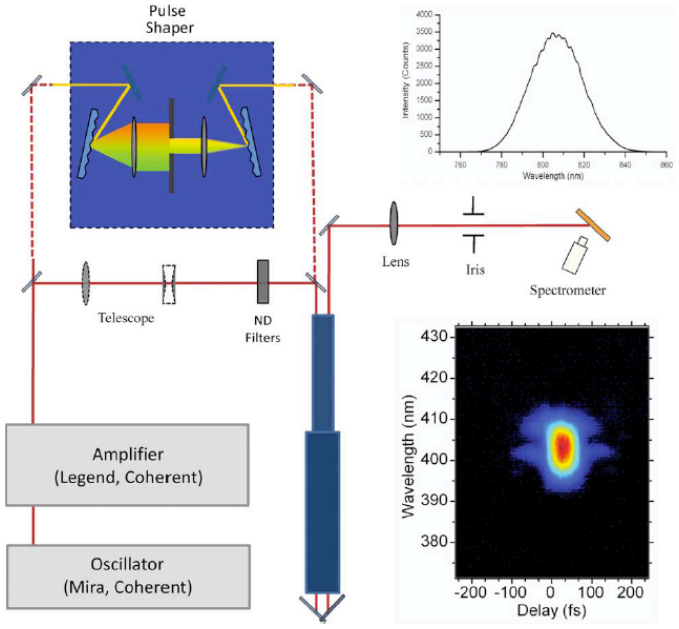

Fig. 2.6 Experimental schematic to measure frequency-resolved ultrashort laser pulse transmission through water [8].

Before entering the water sample, amplified pulses are attenuated by neutral density filters. Laser oscillator pulses are sent through a telescope to reduce the beam size; they are subsequently also sent through neutral density filters. The beam sizes used in our experiment are 10 mm and 2 mm for the amplified and oscillator beams, respectively. Both types of laser pulses are then sent through a cylindrical glass cell manufactured such that pathlength the pulse traverses through water may be varied from 150 to 450 cm. Each pulse is directed through the cell exactly twice. Pulses emerging from the cell are then passed through a focusing lens and an iris that serves as an alignment tool. They are reflected off a white screen attached to a speaker vibrating at 50 Hz (in order to reduce speckle) and measured with a spectrometer (USB2000, Ocean Optics). The spectrometer measurements are accompanied by powermeter measurements (1815-C,

Newport) of the transmitted beam power. At the beginning of each experiment, the spectrometer position is optimized; the alignment is subsequently maintained through the adjustment of the retroreflector and iris mentioned above.

In order to establish that each experimental measurement of laser pulse transmission through water is completed within the linear pulse propagation regime, we measure the spectrum and total transmitted pulse power through 1.5 m of deionized water as a function of pulse power. Fig. 2.7 shows the transmitted pulse power as measured with the powermeter and the spectrometer as a function of incident power of amplified pulses. Each integrated spectrum is normalized to the incident pulse power. A total of 300 spectra compose the data in Fig. 2.7. We see that as long as the pulse power remains below 8.6 mW, the pulse propagates according to linear pulse propagation behavior. All experiments are, therefore, conducted at or below this power level.

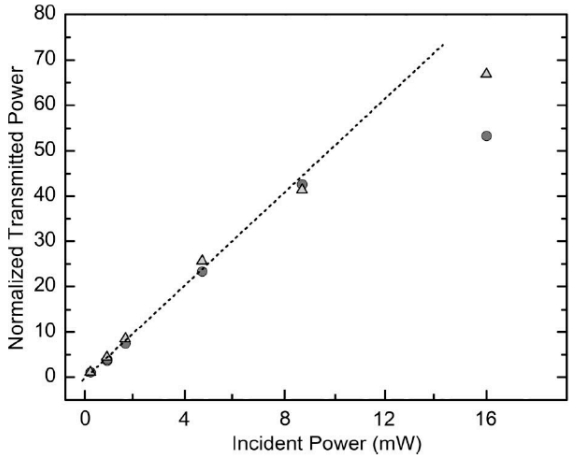

Fig. 2.7 Normalized transmitted power for amplified pulses propagating through 150 cm of the water sample as a function of incident power. The triangles denote powermeter measurements, while the circles denote the integrated spectrometer measurements. The dashed line is the expected behavior for linear behavior. Above 8.6 mW, the transmitted power deviates from linear behavior. All experiments are, therefore, conducted at power levels below 8.6 mW to ensure linear behavior [8].

2.8.3 Linear BLB law confirmed through experiment

Total transmitted pulse power as a function of propagation length is shown in Figs. 2.8. and 2.9 with theoretical curves of the expected behavior. The attenuation data are consistent with the BLB law. We stress, however, that the apparent exponential nature of the power decay is simply a result of the location of the input pulse peak intensity at 800 nm and the relatively narrow pule bandwidth; such exponential behavior of the total transmitted power attenuation is the exception rather than the rule.

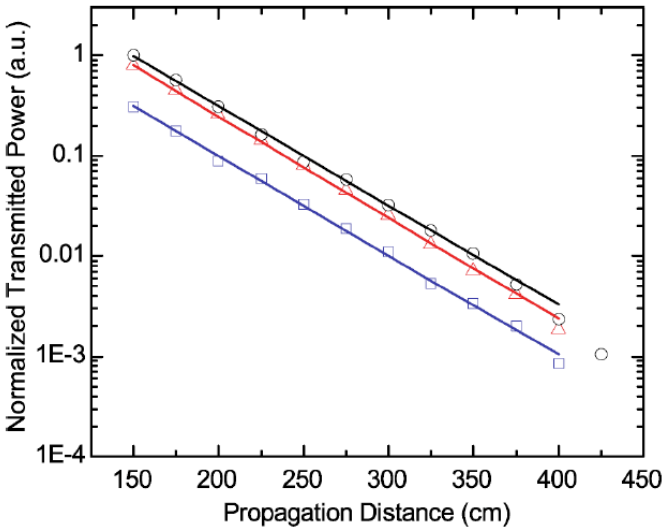

Fig. 2.8 Total measured integrated power as a function of propagation distance as measured by the spectrometer. The circles and squares represent amplified pulses with total incident powers of 8.6 and 4.8 mW, respectively. The triangles denote oscillator pulses with total incident power of 43 mW; solid lines indicate the predicted simulated behavior for each pulse. All error bars are smaller than the symbols [8].

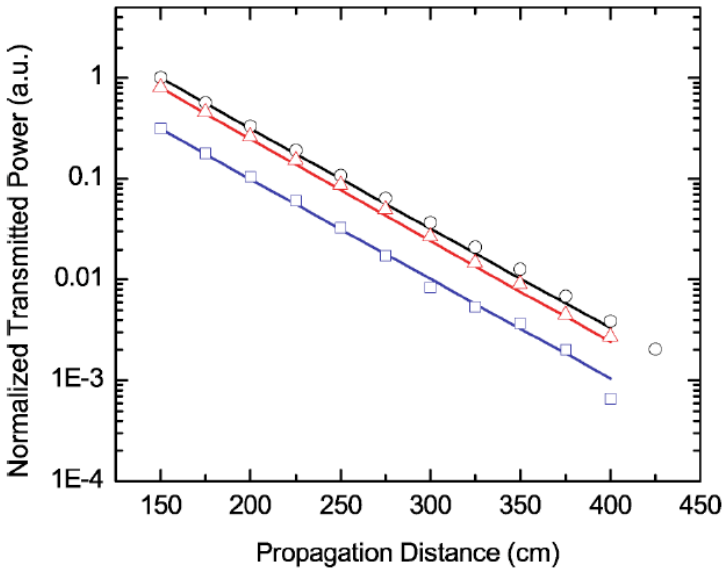

Fig. 2.9 Total measured integrated power as a function of propagation distance as measured by the powermeter. The circles and squares represent amplified pulses with total incident powers of 8.6 and 4.8 mW, respectively. The triangles denote oscillator pulses with total incident power of 43 mW; solid lines indicate the predicted simulated behavior for each pulse. All error bars are smaller than the symbols [8].

The intensity attenuation of each spectral component of the pulses is shown in Figs. 2.10-2.12. As predicted by the BLB law, each spectral component decays exponentially with propagation distance. The absorption coefficient for each spectral component is the slope of the fit line, weighted with the uncertainty, on a log plot. The absorption coefficients for several frequencies are calculated in this manner and shown in Fig. 2.13.

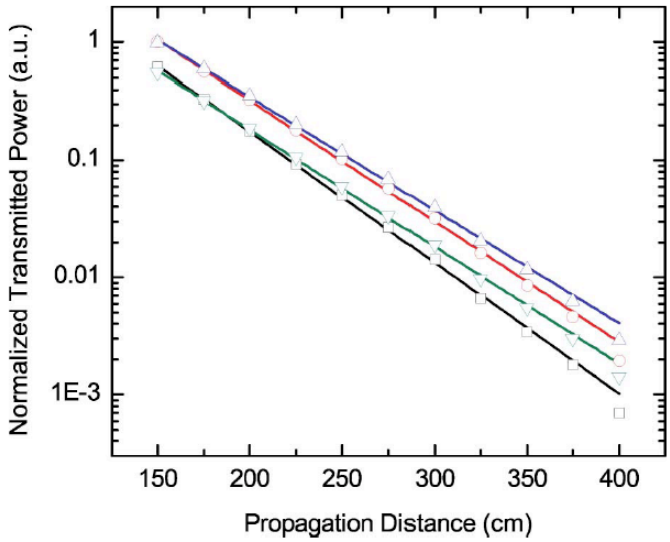

Fig. 2.10 Spectral power for various wavelengths as a function of propagation distance for laser oscillator pulses with total incident power of 43 mW. Squares, circles, and triangles with apices up and down represent wavelengths of 790, 800, 810, and 820 nm, respectively. The solid lines are exponential fits weighted with uncertainty. All error bars are smaller than the symbols [8].

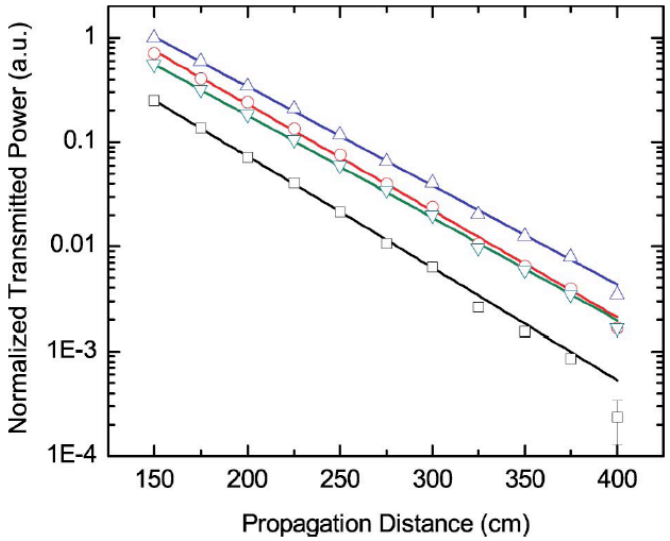

Fig. 2.11 Spectral power for various wavelengths as a function of propagation distance for amplified pulses with total incident power of 4.8 mW. Squares, circles, and triangles with apices up and down represent wavelengths of 790, 800, 810, and 820 nm, respectively. The solid lines are exponential fits weighted with uncertainty. All error bars are smaller than the symbols [8].

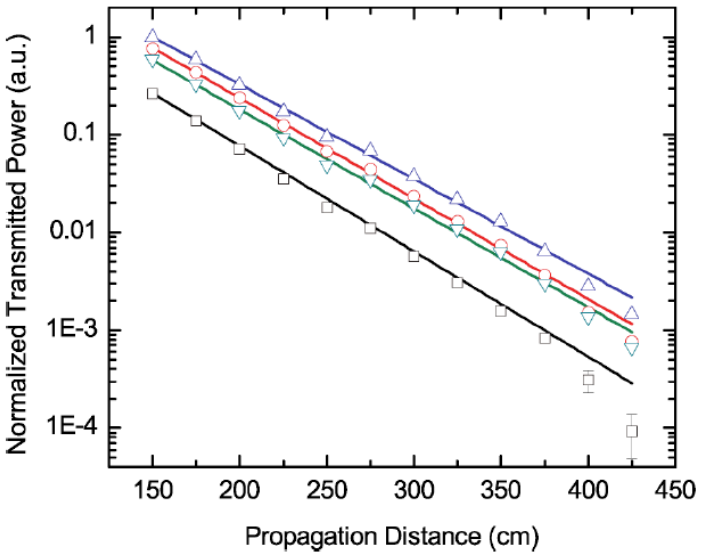

Fig. 2.12 Spectral power for various wavelengths as a function of propagation distance for amplified pulses with total incident power of 8.6 mW. Squares, circles, and triangles with apices up and down represent wavelengths of 790, 800, 810, and 820 nm, respectively. The solid lines are exponential fits weighted with uncertainty. All error bars are smaller than the symbols [8].

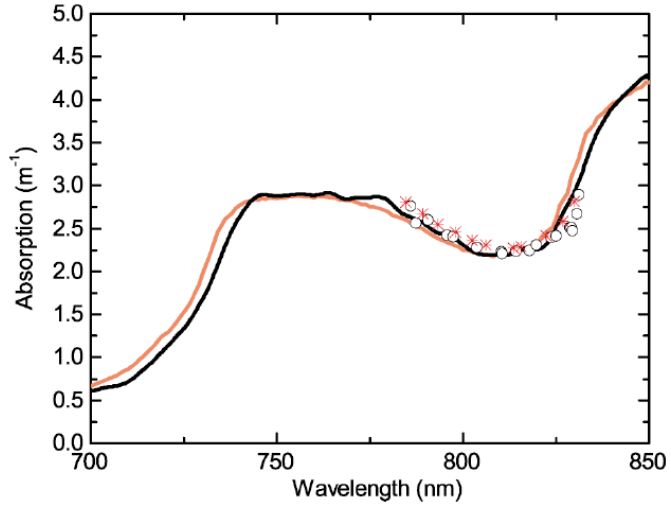

Fig. 2.13 Absorption curve of water, as measured by Kou *et al.* [23] (lighter curve), and the deionized water sample used in the experiments outlined above [8]. Also shown are absorption coefficients measured by laser oscillator pulses (asterisks) and amplified pulses (circles) with total incident powers of 43 and 4.8 mW, respectively [8].

Total transmitted pulse power and intensity of spectral pulse components as a function of chirp are shown in Figs 2.14 and 2.15. In this experiment, the average amplified laser power is fixed at 8.6 mW. The propagation distance of the pulses through the water sample is 350 cm. We vary the input pulse chirp from -10000 fs^2 to 5000 fs^2; for this range of chirps, the variation of the pulse duration is from 800 fs negatively chirped, to the transform-limited value of 35 fs, to 400 fs positively chirped. Over this range of pulse duration, the variation of the measured water transmission is of the order of our experimental uncertainty, which is about ±10% of the average value of power transmission.

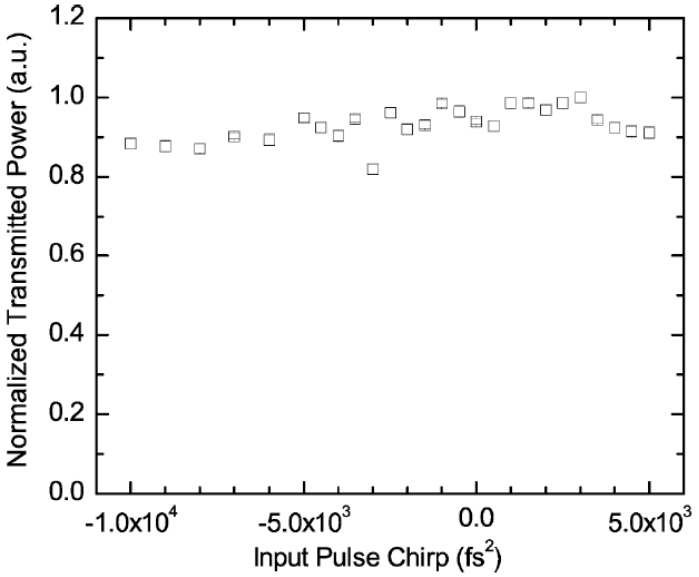

Fig. 2.14 Total integrated power as a function of pulse chirp and duration as measured by the spectrometer for amplified pulses having total incident power of 8.6 mW. Where error bars do not show, they are smaller than the symbols [8].

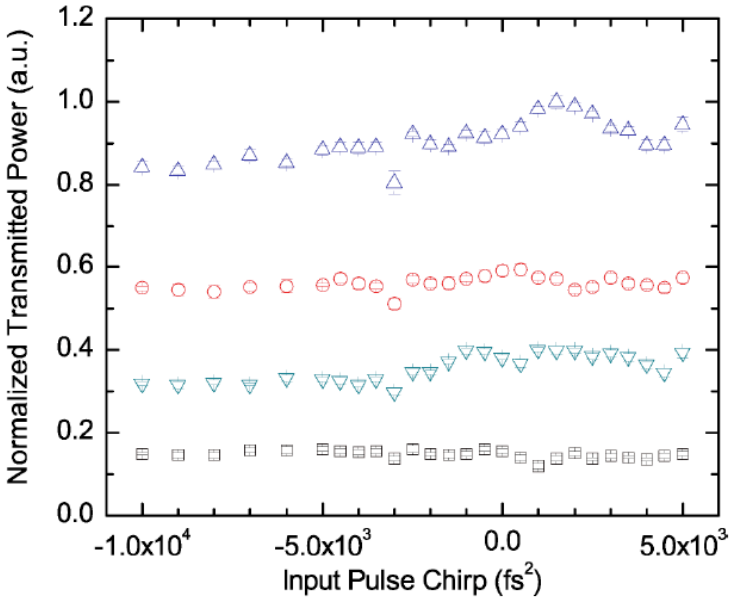

Fig. 2.15 Spectral power for various wavelengths as a function of pulse chirp and duration as measured by the spectrometer for amplified pulses with total incident power of 8.6 mW. Squares, circles, and triangles with apices up and down represent wavelengths of 790, 800, 810, and 820 nm, respectively [8].

2.8.4 No violation of linear optics observed

Our results indicate that no violations of the properly interpreted BLB law occur in the linear regime for femtosecond laser pulses with varying repetition rates, chirps, and pulse durations propagating through water. Our conclusions are commensurate with Li *et al.* [35] and Okawachi *et al.* [36], both of whom have concluded that pulse power attenuation is dependent upon the pulse spectrum bandwidth. Our results are inconsistent, however, with claims that femtosecond pulses propagating through water violate BLB behavior and result in reduced absorption [30,33,34]. On the contrary, not only are our results in complete agreement with BLB, but we are able to reproduce, with reasonable accuracy, the absorption curve of water as measured by Kou *et al.* [23]. This

leads us to conclude that no violations of the BLB law have, to date, been reproduced for femtosecond laser pulses propagating through water in the linear regime.

CHAPTER III

NONLINEAR OPTICS AND PULSE PROPAGATION*

3.1 QUANTUM MECHANICAL MODEL OF THE NONLINEAR SUSCEPTIBLITY: SEMICLASSICAL APPROXIMATION

In sections 2.4 and 2.5 we investigated both the classical and quantum mechanical models, respectively, of the optical linear susceptibility of a medium*. In Chapter III we investigate nonlinear optical phenomena. While both classical and quantum mechanical models exist as models for the nonlinear optical susceptibility, the classical model is considerably limited in the physical phenomena which it can accurately describe. In essence, the classical model of nonlinear susceptibility begins at the same point as the linear Lorentz model of susceptibility in that an equation of motion for an electron in a potential well is sought. In the linear Lorentzian model, the potential well is harmonic in form and corresponds to a restoring force $F(r) = -m_e \omega_0^2 r$. In classical models of the nonlinear susceptibility, the form of the potential well in which the electron oscillates deviates from a purely harmonic form, and the restoring force on the electron is written in the form

$$F(r) = -m_e \omega_0^2 r - m_e a r^2 \tag{3.1}$$

---

* Reprinted with permission from "Propagation of ultrashort laser pulses in water: linear absorption and onset of nonlinear spectral transformation" by A. V. Sokolov, L. M. Naveira, M. P. Poudel, J. Strohaber, C. S. Trendafilova, W. C. Buck, J. Wang, B. D. Strycker, C. Wang, H. Schuessler, A. Kolomenskii, and G. W. Kattawar, 2010. *Applied Optics*, 49, 513-519, Copyright 2010 by Optical Society of America.

$$F(r) = -m_e\omega_0^2 r + m_e b r^3 \ , \tag{3.2}$$

where Eqs. 3.1 and 3.2 represent the responses of noncentrosymmetric and centrosymmetric media, respectively, and a and b characterize the strength of the nonlinearity. Such restoring forces result in equations of motion of the form

$$\ddot{r} + 2\gamma\dot{r} + \omega_0^2 r + ar^2 = -eE(t)/m_e \tag{3.3}$$

$$\ddot{r} + 2\gamma\dot{r} + \omega_0^2 r - br^3 = -eE(t)/m_e \ , \tag{3.4}$$

where Eqs. 3.3 and 3.4 correspond to noncentrosymmetric and centrosymmetric media, respectively. This is a phenomenological treatment of the nonlinear susceptibility; as we mentioned above, the physical insight that can be gained from this classical treatment is limited. Nevertheless, it can function as a type of illustrative model of a more complex phenomenon. A treatment of the classical picture of the nonlinear susceptibility, as well as the solutions to the equations of motion shown in Eqs. 3.3 and 3.4, can be found in [37] and [18]. For the rest of the section, we outline the quantum mechanical description of the nonlinear optical susceptibility.

A quantum mechanical description of the nonlinear optical susceptibility can be gained from an extension of the method outlined in Section 2.5, which outlines the atomic wavefunction perturbation method for calculating the linear optical susceptibility. The possibility for an extension to a description of the nonlinear optical susceptibility can be seen from Eq. 2.74, which has the form [18]

$$a_m^{(N)}(t) = \frac{1}{i\hbar}\sum_l \int_{-\infty}^{t} V_{ml}(t') a_l^{(N-1)}(t') \exp\left[i\omega_{ml}t'\right] dt' \ , \tag{3.5}$$

where, we recall, $a_l^{(N)}(t)$ is the probability amplitude that, to the *N*th order in the perturbation, the atom is in energy eigenstate l at time t. Likewise, we recall that

$$V_{ml} \equiv \langle u_m | \hat{V} | u_l \rangle = \int u_m^* \hat{V} u_l \, d^3 r \tag{3.6}$$

and

$$\omega_{ml} \equiv \omega_m - \omega_l \ . \tag{3.7}$$

In Section 2.5, we saw that to 1st order in the perturbation,

$$a_m^{(1)}(t) = \frac{1}{\hbar} \sum_p \frac{\vec{\mu}_{mg} \cdot \vec{E}(\omega_p)}{\omega_{mg} - \omega_p} \exp\left[i\left(\omega_{mg} - \omega_p\right) t \right] , \tag{3.8}$$

where

$$\vec{\mu}_{ml} = \int u_m^* \hat{\mu} u_l \, d^3 r \ . \tag{3.9}$$

From Eq. 3.8 we were able to calculate the linear susceptibility. In order to calculate the 2nd order nonlinear contributions to the susceptibility, we substitute Eq. 3.8 into Eq. 3.5, yielding

$$a_n^{(2)}(t) = \frac{1}{\hbar^2} \sum_{pq} \sum_m \frac{\left[\vec{\mu}_{nm} \cdot \vec{E}(\omega_q)\right]\left[\vec{\mu}_{mg} \cdot \vec{E}(\omega_p)\right]}{\left(\omega_{ng} - \omega_p - \omega_q\right)\left(\omega_{mg} - \omega_p\right)} \exp\left[i\left(\omega_{ng} - \omega_p - \omega_q\right) t \right] . \tag{3.10}$$

In the same way, in order to calculate the 3rd order nonlinear contribution to susceptibility, we substitute Eq. 3.10 into Eq. 3.5 which yields

$$a_v^{(3)}(t) = \frac{1}{\hbar^3} \sum_{pqr} \sum_{mn} \frac{\left[\vec{\mu}_{vn} \cdot \vec{E}(\omega_r)\right]\left[\vec{\mu}_{nm} \cdot \vec{E}(\omega_q)\right]\left[\vec{\mu}_{mg} \cdot \vec{E}(\omega_p)\right]}{\left(\omega_{vg} - \omega_p - \omega_q - \omega_r\right)\left(\omega_{ng} - \omega_p - \omega_q\right)\left(\omega_{mg} - \omega_p\right)} \cdot \times \exp\left[i\left(\omega_{vg} - \omega_p - \omega_q - \omega_r\right) t \right] \tag{3.11}$$

We recall that the polarization density is of the form $\vec{P} = n\langle \vec{p} \rangle$ with n being the number density of dipoles per unit volume and $\langle \vec{p} \rangle$ being the electric dipole moment given by

$$\langle \vec{p} \rangle = \langle \psi | \hat{\mu} | \psi \rangle \ . \tag{3.12}$$

Since we seek a solution of the form

$$\psi(\vec{r},t) = \psi^{(0)}(\vec{r},t) + \lambda\psi^{(1)}(\vec{r},t) + \lambda^2\psi^{(2)}(\vec{r},t) + \lambda^3\psi^{(3)}(\vec{r},t) + ... \tag{3.13}$$

we can rewrite Eq. 3.12 as

$$\begin{aligned}\langle \psi | \hat{\mu} | \psi \rangle = \langle \psi^{(0)} | \hat{\mu} | \psi^{(0)} \rangle &+ \lambda\left[\langle \psi^{(0)} | \hat{\mu} | \psi^{(1)} \rangle + \langle \psi^{(1)} | \hat{\mu} | \psi^{(0)} \rangle\right] \\ &+ \lambda^2\left[\langle \psi^{(0)} | \hat{\mu} | \psi^{(2)} \rangle + \langle \psi^{(1)} | \hat{\mu} | \psi^{(1)} \rangle + \langle \psi^{(2)} | \hat{\mu} | \psi^{(0)} \rangle\right] \\ &+ \lambda^3\left[\langle \psi^{(0)} | \hat{\mu} | \psi^{(3)} \rangle + \langle \psi^{(1)} | \hat{\mu} | \psi^{(2)} \rangle + \langle \psi^{(2)} | \hat{\mu} | \psi^{(1)} \rangle + \langle \psi^{(3)} | \hat{\mu} | \psi^{(0)} \rangle\right] \\ &+ ...\end{aligned} \tag{3.14}$$

We require that all terms proportional to λ^N satisfy the Hamiltonian in Eq. 2.58 separately. In Section 2.5, we showed that the term proportional to λ yields the linear optical susceptibility through the first order contribution to $\langle \vec{p} \rangle$, defined as

$$\langle \vec{p}^{(1)} \rangle = \langle \psi^{(0)} | \hat{\mu} | \psi^{(1)} \rangle + \langle \psi^{(1)} | \hat{\mu} | \psi^{(0)} \rangle \ . \tag{3.15}$$

In Eq. 3.14, the terms proportional to λ^2 and λ^3 yield the 2nd and 3rd order contributions to $\langle \vec{p} \rangle$, respectively, and have the forms

$$\langle \vec{p}^{(2)} \rangle = \langle \psi^{(0)} | \hat{\mu} | \psi^{(2)} \rangle + \langle \psi^{(1)} | \hat{\mu} | \psi^{(1)} \rangle + \langle \psi^{(2)} | \hat{\mu} | \psi^{(0)} \rangle \tag{3.16}$$

$$\langle \vec{p}^{(3)} \rangle = \langle \psi^{(0)} | \hat{\mu} | \psi^{(3)} \rangle + \langle \psi^{(1)} | \hat{\mu} | \psi^{(2)} \rangle + \langle \psi^{(2)} | \hat{\mu} | \psi^{(1)} \rangle + \langle \psi^{(3)} | \hat{\mu} | \psi^{(0)} \rangle \ . \tag{3.17}$$

When we recall that

$$\psi^{(N)}(\vec{r},t)=\sum_{l}a_{l}^{(N)}(t)u_{l}(\vec{r})\exp\left[-i\omega_{l}t\right], \tag{3.18}$$

we can solve for $\left\langle \vec{p}^{(2)}\right\rangle$ and $\left\langle \vec{p}^{(3)}\right\rangle$, and through these quantities we can calculate the 2nd and 3rd order nonlinear contributions to the optical susceptibility.

We solve first for the 2nd order nonlinear contribution to the optical susceptibility. Solving for $\left\langle \vec{p}^{(2)}\right\rangle$ we see that

$$\left\langle \vec{p}^{(2)}\right\rangle=\frac{1}{\hbar^{2}}\sum_{pq}\sum_{mn}\left(\begin{array}{l}\dfrac{\vec{\mu}_{gn}\left[\vec{\mu}_{nm}\cdot\vec{E}(\omega_{q})\right]\left[\vec{\mu}_{mg}\cdot\vec{E}(\omega_{p})\right]}{\left(\omega_{ng}-\omega_{p}-\omega_{q}\right)\left(\omega_{mg}-\omega_{p}\right)}\exp\left[-i\left(\omega_{p}+\omega_{q}\right)t\right]\\ +\dfrac{\left[\vec{\mu}_{ng}\cdot\vec{E}(\omega_{q})\right]^{*}\vec{\mu}_{nm}\left[\vec{\mu}_{mg}\cdot\vec{E}(\omega_{q})\right]}{\left(\omega_{ng}^{*}-\omega_{q}\right)\left(\omega_{mg}-\omega_{p}\right)}\exp\left[-i\left(\omega_{p}-\omega_{q}\right)t\right]\\ +\dfrac{\left[\vec{\mu}_{ng}\cdot\vec{E}(\omega_{q})\right]^{*}\left[\vec{\mu}_{nm}\cdot\vec{E}(\omega_{p})\right]^{*}\vec{\mu}_{mg}}{\left(\omega_{ng}^{*}-\omega_{q}\right)\left(\omega_{mg}^{*}-\omega_{q}-\omega_{q}\right)}\exp\left[i\left(\omega_{p}+\omega_{q}\right)t\right]\end{array}\right). \tag{3.19}$$

Because the frequencies ω_{p} and ω_{q} are summed over all positive and negative frequencies, we have the freedom to substitute negative frequencies for positive ones where convenient in Eq. 3.19, resulting in an equation of the form

$$\left\langle \vec{p}^{(2)} \right\rangle = \frac{1}{\hbar^2} \sum_{pq} \sum_{mn} \left(\begin{array}{l} \dfrac{\vec{\mu}_{gn} \left[\vec{\mu}_{nm} \cdot \vec{E}(\omega_q) \right] \left[\vec{\mu}_{mg} \cdot \vec{E}(\omega_p) \right]}{\left(\omega_{ng} - \omega_p - \omega_q \right) \left(\omega_{mg} - \omega_p \right)} \\ + \dfrac{\left[\vec{\mu}_{ng} \cdot \vec{E}(\omega_q) \right]^* \vec{\mu}_{nm} \left[\vec{\mu}_{mg} \cdot \vec{E}(\omega_q) \right]}{\left(\omega_{ng}^* + \omega_q \right) \left(\omega_{mg} - \omega_p \right)} \\ + \dfrac{\left[\vec{\mu}_{ng} \cdot \vec{E}(\omega_q) \right]^* \left[\vec{\mu}_{nm} \cdot \vec{E}(\omega_p) \right]^* \vec{\mu}_{mg}}{\left(\omega_{ng}^* + \omega_q \right) \left(\omega_{mg}^* + \omega_q + \omega_q \right)} \end{array} \right) \exp\left[-i \left(\omega_p + \omega_q \right) t \right] . \tag{3.20}$$

The second order polarization density is defined to be

$$\vec{P}^{(2)} = n \left\langle \vec{p}^{(2)} \right\rangle , \tag{3.21}$$

where n is the number density of dipoles per unit volume. In addition, we write the polarization density in terms of frequency components such that

$$\vec{P}^{(2)} = \sum_r \vec{P}_0(\omega_r) \exp\left[-i \omega_r t \right] , \tag{3.22}$$

and write the definition of the 2nd order nonlinear susceptibility as

$$P_i^{(2)} = \varepsilon_0 \sum_{jk} \sum_{pq} \chi_{ijk}^{(2)}(\omega_p + \omega_q, \omega_q, \omega_p) E_j(\omega_q) E_k(\omega_p) . \tag{3.23}$$

Hence, the 2nd order nonlinear susceptibility is given as

$$\chi_{ijk}^{(2)}(\omega_p + \omega_q, \omega_q, \omega_p) = \frac{n}{\varepsilon_0 \hbar^2} \wp_I \sum_{mn} \left(\begin{array}{l} \dfrac{\mu_{gn}^i \mu_{nm}^j \mu_{mg}^k}{\left(\omega_{ng} - \omega_p - \omega_q \right) \left(\omega_{mg} - \omega_p \right)} \\ + \dfrac{\mu_{gn}^j \mu_{nm}^i \mu_{mg}^k}{\left(\omega_{ng}^* + \omega_q \right) \left(\omega_{mg} - \omega_p \right)} \\ + \dfrac{\mu_{gn}^j \mu_{nm}^k \mu_{mg}^i}{\left(\omega_{ng}^* + \omega_q \right) \left(\omega_{mg}^* + \omega_q + \omega_q \right)} \end{array} \right) , \tag{3.24}$$

where $\wp_I$ is the intrinsic permutation operator, taken over all permutations of frequencies ω_p and ω_q. In all, in its expanded form, Eq. 3.24 has six terms.

We now solve for the 3rd order nonlinear contribution to the optical susceptibility. Solving for $\left\langle \vec{p}^{(3)} \right\rangle$ we see that

$$\left\langle \vec{p}^{(3)} \right\rangle = \frac{1}{\hbar^3} \sum_{pqr} \sum_{mnv} \left(\begin{array}{l} \dfrac{\vec{\mu}_{gv}\left[\vec{\mu}_{vn}\cdot\vec{E}(\omega_r)\right]\left[\vec{\mu}_{nm}\cdot\vec{E}(\omega_q)\right]\left[\vec{\mu}_{mg}\cdot\vec{E}(\omega_p)\right]}{\left(\omega_{vg}-\omega_r-\omega_p-\omega_q\right)\left(\omega_{ng}-\omega_p-\omega_q\right)\left(\omega_{mg}-\omega_p\right)} \exp\left[-i\left(\omega_p+\omega_q+\omega_r\right)t\right] \\ + \dfrac{\left[\vec{\mu}_{vg}\cdot\vec{E}(\omega_r)\right]^*\vec{\mu}_{vn}\left[\vec{\mu}_{nm}\cdot\vec{E}(\omega_q)\right]\left[\vec{\mu}_{mg}\cdot\vec{E}(\omega_p)\right]}{\left(\omega_{vg}^*-\omega_r\right)\left(\omega_{ng}-\omega_q-\omega_p\right)\left(\omega_{mg}-\omega_p\right)} \exp\left[-i\left(\omega_p+\omega_q-\omega_r\right)t\right] \\ + \dfrac{\left[\vec{\mu}_{vg}\cdot\vec{E}(\omega_r)\right]^*\left[\vec{\mu}_{nv}\cdot\vec{E}(\omega_q)\right]^*\vec{\mu}_{nm}\left[\vec{\mu}_{mg}\cdot\vec{E}(\omega_p)\right]}{\left(\omega_{vg}^*-\omega_r\right)\left(\omega_{ng}^*-\omega_q-\omega_p\right)\left(\omega_{mg}-\omega_p\right)} \exp\left[-i\left(\omega_p-\omega_q-\omega_r\right)t\right] \\ + \dfrac{\left[\vec{\mu}_{vg}\cdot\vec{E}(\omega_r)\right]^*\left[\vec{\mu}_{nv}\cdot\vec{E}(\omega_q)\right]^*\left[\vec{\mu}_{mn}\cdot\vec{E}(\omega_p)\right]^*\vec{\mu}_{mg}}{\left(\omega_{vg}^*-\omega_r\right)\left(\omega_{ng}^*-\omega_q-\omega_r\right)\left(\omega_{mg}^*-\omega_r-\omega_q-\omega_p\right)} \exp\left[i\left(\omega_p+\omega_q+\omega_r\right)t\right] \end{array} \right). \tag{3.25}$$

Again, because the frequencies ω_p, ω_q, and ω_r are summed over all positive and negative frequencies, we have the freedom to substitute negative frequencies for positive ones where convenient in Eq. 3.25, resulting in an equation of the form

$$\left\langle \vec{p}^{(3)} \right\rangle = \frac{1}{\hbar^3} \sum_{pqr} \sum_{mnv} \left(\begin{array}{l} \dfrac{\vec{\mu}_{gv}\left[\vec{\mu}_{vn}\cdot\vec{E}(\omega_r)\right]\left[\vec{\mu}_{nm}\cdot\vec{E}(\omega_q)\right]\left[\vec{\mu}_{mg}\cdot\vec{E}(\omega_p)\right]}{\left(\omega_{vg}-\omega_r-\omega_p-\omega_q\right)\left(\omega_{ng}-\omega_p-\omega_q\right)\left(\omega_{mg}-\omega_p\right)} \\ + \dfrac{\left[\vec{\mu}_{vg}\cdot\vec{E}(\omega_r)\right]^*\vec{\mu}_{vn}\left[\vec{\mu}_{nm}\cdot\vec{E}(\omega_q)\right]\left[\vec{\mu}_{mg}\cdot\vec{E}(\omega_p)\right]}{\left(\omega_{vg}^*+\omega_r\right)\left(\omega_{ng}-\omega_q-\omega_p\right)\left(\omega_{mg}-\omega_p\right)} \\ + \dfrac{\left[\vec{\mu}_{vg}\cdot\vec{E}(\omega_r)\right]^*\left[\vec{\mu}_{nv}\cdot\vec{E}(\omega_q)\right]^*\vec{\mu}_{nm}\left[\vec{\mu}_{mg}\cdot\vec{E}(\omega_p)\right]}{\left(\omega_{vg}^*+\omega_r\right)\left(\omega_{ng}^*+\omega_q+\omega_p\right)\left(\omega_{mg}-\omega_p\right)} \\ + \dfrac{\left[\vec{\mu}_{vg}\cdot\vec{E}(\omega_r)\right]^*\left[\vec{\mu}_{nv}\cdot\vec{E}(\omega_q)\right]^*\left[\vec{\mu}_{mn}\cdot\vec{E}(\omega_p)\right]^*\vec{\mu}_{mg}}{\left(\omega_{vg}^*+\omega_r\right)\left(\omega_{ng}^*+\omega_q+\omega_r\right)\left(\omega_{mg}^*+\omega_r+\omega_q+\omega_p\right)} \end{array} \right) \exp\left[-i\left(\omega_p+\omega_q+\omega_r\right)t\right]. \tag{3.26}$$

Again, we let

$$\vec{P}^{(3)} = n\left\langle \vec{p}^{(3)} \right\rangle = \sum_s \vec{P}_0^{(3)}(\omega_s)\exp\left[-i\omega_s t\right] \tag{3.27}$$

and write the definition of the 3rd order nonlinear susceptibility as

$$P_k^{(3)} = \varepsilon_0 \sum_{hij} \sum_{pqr} \chi_{kjih}^{(3)}(\omega_\sigma, \omega_r, \omega_q, \omega_p) E_j(\omega_r) E_i(\omega_q) E_h(\omega_p) \ . \tag{3.28}$$

We then see that the 3rd order nonlinear susceptibility is

$$\chi_{kjih}^{(3)}(\omega_\sigma, \omega_r, \omega_q, \omega_p) = \frac{n}{\varepsilon_0 \hbar^3} \wp_I \sum_{mnv} \left(\begin{array}{l} \dfrac{\mu_{gv}^k \mu_{vn}^j \mu_{nm}^i \mu_{mg}^h}{\left(\omega_{vg} - \omega_r - \omega_p - \omega_q\right)\left(\omega_{ng} - \omega_p - \omega_q\right)\left(\omega_{mg} - \omega_p\right)} \\ + \dfrac{\mu_{gv}^j \mu_{vn}^k \mu_{nm}^i \mu_{mg}^h}{\left(\omega_{vg}^* + \omega_r\right)\left(\omega_{ng} - \omega_q - \omega_p\right)\left(\omega_{mg} - \omega_p\right)} \\ + \dfrac{\mu_{gv}^j \mu_{vn}^i \mu_{nm}^k \mu_{mg}^h}{\left(\omega_{vg}^* + \omega_r\right)\left(\omega_{ng}^* + \omega_q + \omega_p\right)\left(\omega_{mg} - \omega_p\right)} \\ + \dfrac{\mu_{gv}^j \mu_{vn}^i \mu_{nm}^h \mu_{mg}^k}{\left(\omega_{vg}^* + \omega_r\right)\left(\omega_{ng}^* + \omega_q + \omega_r\right)\left(\omega_{mg}^* + \omega_r + \omega_q + \omega_p\right)} \end{array} \right), \tag{3.29}$$

where again $\wp_I$ is the intrinsic permutation operator taken over the frequencies ω_p, ω_q, and ω_r. In all, the expanded form of Eq. 3.29 has 24 terms.

Several important insights can be gained from the equations for the 2nd and 3rd order nonlinear contributions to the optical susceptibility as given in Eqs. 3.24 and 3.29, respectively. We notice that there are one- and two-photon resonances for the 2nd order susceptibility $\chi^{(2)}$ and one-, two-, and three-photon resonances for the 3rd order susceptibility $\chi^{(3)}$. Our use of the word "photon" here refers to a single mode of the electric field E with a frequency of ω_p, ω_q, or ω_r. The simultaneous presence of these resonances are only described by a quantum mechanical model; a classical model of the nonlinear susceptibility does not account for them.

Another insight may be gained from the expressions for the expectation value of the dipole moments shown in Eqs. 3.20 and 3.26. What is interesting is that the 2nd order average dipole moment $\langle \vec{p}^{(2)} \rangle$ oscillates at a frequency of $\omega = \omega_p + \omega_q$, while the 3rd order average dipole moment $\langle \vec{p}^{(3)} \rangle$ oscillates at a frequency of $\omega = \omega_p + \omega_q + \omega_r$. We note that the frequencies ω_p, ω_q, and ω_r may take on any value, both positive and negative. Hence nonlinear optical interactions between electric field components can give rise to generation of new frequencies. 2nd order processes that take advantage of this are 2nd harmonic generation, sum frequency generation, and difference frequency generation [18]. 3rd order processes that take advantage of this are 3rd harmonic generation, four-wave mixing, self-phase modulation, etc. [18]. The above treatment is not sufficient to adequately explore these various phenomena, especially since we have not touched upon the important factor of phase-matching. However, we will in later sections investigate those nonlinear phenomena which bear upon nonlinear pulse propagation in isotropic media.

The linear, 2nd order, and 3rd order susceptibilities may be combined into a single expression for the polarization density. Recall that the polarization density is

$$\vec{P} = n\langle \vec{p} \rangle = n\langle \psi | \hat{\mu} | \psi \rangle \ , \tag{3.30}$$

where *n* is the number density per unit volume. We have previously expanded the average value of the dipole moment into various orders of a perturbation of a form shown in Eq. 3.14. Neglecting the zeroth order term, the polarization density may be written

$$\begin{aligned}\vec{P} &= n\left\langle \vec{p}^{(1)} \right\rangle + n\left\langle \vec{p}^{(2)} \right\rangle + n\left\langle \vec{p}^{(3)} \right\rangle + \ldots \\ &= \vec{P}^{(1)} + \vec{P}^{(2)} + \vec{P}^{(3)} + \ldots\end{aligned} \quad . \tag{3.31}$$

This in turn may be written as

$$\begin{aligned}P_i = \varepsilon_0 \sum_j \chi_{ij}^{(1)}(\omega_p) E_j(\omega_p) + \varepsilon_0 \sum_{jk}\sum_{pq} \chi_{ijk}^{(2)}(\omega_p + \omega_q, \omega_p, \omega_q) E_j(\omega_q) E_k(\omega_p) \\ + \varepsilon_0 \sum_{hkj}\sum_{pqr} \chi_{ijkh}^{(3)}(\omega_\sigma, \omega_p, \omega_q, \omega_r) E_j(\omega_r) E_k(\omega_q) E_h(\omega_p) + \ldots\end{aligned} \quad , \tag{3.32}$$

where we have truncated the expression after the third order contribution, in accordance with our analysis above. Equation 3.32 is the full expression for the nonlinear optical polarization density, and it depends upon the amplitudes and intensities of the electric field.

We point out that, for centrosymmetric media, the 2nd order susceptibility tensor $\chi_{ij}^{(2)}$ is zero. This may be understood through the following simple proof, which assumes a centrosymmetric medium that generates a 2nd harmonic signal and responds instantaneously to the applied electric field [18]. We assume the nonlinear polarization is given by

$$P(t) = \varepsilon_0 \chi^{(2)} E^2(t) \quad . \tag{3.33}$$

Because the medium is centrosymmetric, it possesses inversion symmetry, and therefore it must be true that if we change the sign of the electric field, the sign of the polarization must also change. We write

$$-P(t) = \varepsilon_0 \chi^{(2)} \left[-E(t)\right]^2 = \varepsilon_0 \chi^{(2)} E^2(t) \quad . \tag{3.34}$$

Comparing Eq. 3.34 with Eq. 3.33, we see that $P(t)$ must equal $-P(t)$, which can only happen if the polarization density vanishes identically. This shows that

$$\chi^{(2)} = 0 \ . \tag{3.35}$$

It is a general result that for isotropic, centrosymmetric media the 2nd order susceptibility is zero. However, even for an isotropic medium, an asymmetry may be introduced into the system through the application of a static electric or magnetic field, resulting in a nonzero 2nd order susceptibility. The surfaces of isotropic media also exhibit asymmetry, and therefore, at the surface, the 2nd order susceptibility is nonzero. This effect is used to great benefit in nonlinear optical characterization of material surfaces.

However, for the remainder of the chapter, we will investigate nonlinear pulse propagation within bulk media that are isotropic and for which, therefore, the 2nd order susceptibility is zero.

3.2 NONLINEAR REFRACTIVE INDEX

In the following two sections, in which we describe the nonlinear refractive index and the pulse propagation equations through nonlinear media, we assume a medium which has negligible absorption. This is sufficient to describe many nonlinear isotropic media. While it is not strictly accurate for a description of water, the assumption that absorption plays a negligible role simplifies the illustrative physical derivations involved and provides clarity to the resultant equations. While we will work with only real quantities, it should be remembered that, in general, nonlinear susceptibilities and refractive indices are complex quantities. Indeed, the imaginary part of the 3rd order susceptibility is proportional to the two-photon absorption cross section, an important parameter in many experiments. We point out that the phenomenon of absorption may

be recovered within our theoretical treatment in many instances simply by replacing the real linear and nonlinear refractive indices with complex quantities [18,38].

We begin by describing the refractive index n of a nonlinear dispersive and isotropic material as

$$n = n_0 + \bar{n}_2 \left\langle E(t)^2 \right\rangle \ , \tag{3.36}$$

where n_0 is the linear refractive index and

$$E(t) = E(\omega)\exp\left[-i\omega t\right] + c.c. \tag{3.37}$$

Hence we see that

$$\left\langle E(t)^2 \right\rangle = 2E(\omega)E(\omega)^* = 2\left|E(\omega)\right|^2 \ . \tag{3.38}$$

Therefore the refractive index in Eq. 3.36 may be written as

$$n = n_0 + 2\bar{n}_2 \left|E(\omega)\right|^2 \ . \tag{3.39}$$

We recall that the total polarization density of a centrosymmetric medium may be described by

$$\begin{aligned} P_i = {} & \varepsilon_0 \sum_j \chi_{ij}^{(1)}(\omega_p) E_j(\omega_p) \\ & + \varepsilon_0 \sum_{hkj} \sum_{pqr} \chi_{ijkh}^{(3)}(\omega_\sigma, \omega_p, \omega_q, \omega_r) E_j(\omega_r) E_k(\omega_q) E_h(\omega_p) + \ldots \end{aligned} \tag{3.40}$$

For an isotropic, centrosymmetric medium, the nonlinear refractive index that governs propagation of a single beam is dependent on a susceptibility of the form $\chi^{(3)}(\omega = \omega + \omega - \omega)$, such that we may write the total polarization density of the medium as

$$\vec{P} = \varepsilon_0 \chi^{(1)} E(\omega) + 3\varepsilon_0 \chi^{(3)} \left|E(\omega)\right|^2 E(\omega) = \varepsilon_0 \chi_{eff} E(\omega) \ . \tag{3.41}$$

The factor of 3 before $\chi^{(3)}$ in Eq. 3.41 is known as the *degeneracy factor* and represents the number of distinct permutations of the frequencies ω_p, ω_q, and ω_r in Eq. 3.40 with our particular setup in mind. Note that we have defined an effective total susceptibility of the form

$$\chi_{eff} = \chi^{(1)} + 3\chi^{(3)}\left|E(\omega)\right|^2 \ . \tag{3.42}$$

We recall that

$$n^2 = 1 + \chi_{eff} \ , \tag{3.43}$$

so that

$$\left[n_0 + 2\overline{n}_2\left|E(\omega)\right|^2\right]^2 = 1 + \chi^{(1)} + 3\chi^{(3)}\left|E(\omega)\right|^2 \ . \tag{3.44}$$

Collecting terms up to order of $\left|E(\omega)\right|^2$, we see that

$$n_0^2 + 4n_0\overline{n}_2\left|E(\omega)\right|^2 = \left(1 + \chi^{(1)}\right) + 3\chi^{(3)}\left|E(\omega)\right|^2 \ . \tag{3.45}$$

We therefore see that

$$n_0 = \sqrt{1 + \chi^{(1)}} \tag{3.46}$$

$$\overline{n}_2 = \frac{3\chi^{(3)}}{4n_0} \ . \tag{3.47}$$

An alternative definition of the refractive index relies upon the intensity of the electromagnetic field:

$$n = n_0 + n_2 I \ , \tag{3.48}$$

where

$$I = 2n_0\varepsilon_0 c\left|E(\omega)\right|^2 \ . \tag{3.49}$$

By comparing Eqs. 3.39 and 3.48, we see that

$$2\bar{n}_2\left|E(\omega)\right|^2 = n_2 I \ , \tag{3.50}$$

and therefore

$$n_2 = \frac{\bar{n}_2}{n_0\varepsilon_0 c} = \frac{3\chi^{(3)}}{4n_0^2\varepsilon_0 c} \ . \tag{3.51}$$

In the following section, we will see how the nonlinear refractive index n_2 affects pulse propagation within an isotropic nonlinear medium.

3.3 THE NONLINEAR SCHRÖDINGER EQUATON (NLSE)

We would like to derive an equation which describes how an ultrashort pulse of the form

$$E(z,t) = A(z,t)\exp\left[i\left(k_0 z - \omega_0 t\right)\right] + c.c. \tag{3.52}$$

propagates through a nonlinear isotropic medium. In particular, we would like an equation that describes how the pulse envelope function $A(z,t)$ develops as the pulse propagates through the medium. We begin with Maxwell's macroscopic electromagnetic wave equation, which is equivalent to Eq. 2.22:

$$\frac{\partial^2 E}{\partial z^2} - \frac{1}{\varepsilon_0 c^2}\frac{\partial^2 D}{\partial t^2} = 0 \ . \tag{3.53}$$

We point out that because $D = \varepsilon_0 E + P$, Eq. 3.53 contains all of the linear as well as nonlinear responses of the medium to the applied electric field. Both $E(z,t)$ and $D(z,t)$ can be described in terms of their Fourier components in the frequency domain, i.e.

$$E(z,t) = \int_{-\infty}^{\infty} E(z,\omega)\exp\left[-i\omega t\right]d\omega \tag{3.54}$$

$$D(z,t) = \int_{-\infty}^{\infty} D(z,\omega)\exp\left[-i\omega t\right]d\omega \ . \tag{3.55}$$

Analogously to the previous section, where we introduced an effective susceptibility χ_{eff} that included both linear and nonlinear contributions, we introduce an effective relative permittivity $\varepsilon(\omega)$ such that

$$D(z,\omega) = \varepsilon_0\varepsilon(\omega)E(z,\omega) \ . \tag{3.56}$$

Substituting Eqs. 3.54, 3.55, and 3.56 into Eq. 3.53 results in a wave propagation equation of the form

$$\frac{\partial^2 E(z,\omega)}{\partial z^2} + \varepsilon(\omega)\frac{\omega^2}{c^2}E(z,\omega) = 0 \ . \tag{3.57}$$

We now make use of the fact that the pulse envelope $A(z,\omega)$ may also be expressed in terms of the Fourier transform of its temporal behavior:

$$A(z,\omega') = \int_{-\infty}^{\infty} A(z,t)\exp\left[i\omega' t\right]dt \ . \tag{3.58}$$

We find that this is related to the electric field:

$$\begin{aligned} E(z,\omega) &= A(z,\omega-\omega_0)\exp\left[ik_0 z\right] + A^*(z,\omega+\omega_0)\exp\left[-ik_0 z\right] \\ &\simeq A(z,\omega-\omega_0)\exp\left[ik_0 z\right] \end{aligned}, \tag{3.59}$$

where we have used the fact that contributions from high frequencies such as $\omega+\omega_0$ must be negligible, because $A(z,t)$ varies slowly in time. In addition, we assume that the amplitude of $A(z,t)$ cannot change very quickly as a function of propagation distance z,

and so the second derivative of the electric field with respect to z must be very small in comparison to the first derivative. We then substitute Eq. 3.59 into Eq. 3.57 and, taking account of the approximations we have outlined above, find that

$$2ik_0 \frac{\partial A}{\partial z} + \left(k^2 - k_0^2\right) A = 0 \ , \tag{3.60}$$

where $k(\omega) = \sqrt{\varepsilon(\omega)}\,\omega / c$. Often, to a good approximation, k is not very different from k_0, so that we can say

$$k^2 - k_0^2 = \left(k + k_0\right)\left(k - k_0\right) \simeq 2k_0\left(k - k_0\right) \ . \tag{3.61}$$

Substituting Eq. 3.61 into Eq. 3.60 yields

$$\frac{\partial A}{\partial z} - i\left(k - k_0\right) A = 0 \ . \tag{3.62}$$

We now follow a similar method as was outlined in Section 2.7 and expand $k(\omega)$ as a Taylor series centered on ω_0, taking into account the nonlinear contribution :

$$k = k_0 + \Delta k + \beta_1\left(\omega - \omega_0\right) + \frac{1}{2}\beta_2\left(\omega - \omega_0\right)^2 + ... \tag{3.63}$$

where

$$\Delta k = \frac{\Delta n_{NL}\omega_0}{c} + i\frac{\alpha}{2} = \frac{n_2 I\omega_0}{c} + i\frac{\alpha}{2} \tag{3.64}$$

and

$$\beta_n = \left.\frac{\partial^n k}{\partial \omega^n}\right|_{\omega_0} \ . \tag{3.65}$$

The factor α in Eq. 3.64 is a simple way to account for an average absorption coefficient. Substituting Eq. 3.63 into Eq. 3.62 yields

$$\frac{\partial A}{\partial z} - i\Delta k\, A - i\beta_1\left(\omega-\omega_0\right)A - \frac{1}{2}i\beta_2\left(\omega-\omega_0\right)^2 A = 0 \ . \tag{3.66}$$

We now Fourier transform Eq. 3.66 into the time domain:

$$\frac{\partial A}{\partial z} + \beta_1\frac{\partial A}{\partial t} + \frac{1}{2}i\beta_2\frac{\partial^2 A}{\partial t^2} - i\Delta k\, A = 0 \ . \tag{3.67}$$

It is often convenient to describe Eq. 3.67 in the coordinate frame that moves with the pulse at speed $\upsilon_g = \beta_1^{-1}$. We make the substitution

$$T = t - \beta_1 z \ , \tag{3.68}$$

which, after substitution into Eq. 3.67, yields

$$\frac{\partial A_s}{\partial z} + \frac{1}{2}i\beta_2\frac{\partial^2 A_s}{\partial T^2} - i\Delta k\, A_s = 0 \ , \tag{3.69}$$

where $A_s = A_s(z,T) = A(z,t)$. We now recall that

$$\Delta k_{NL} = \frac{n_2\omega_0 I}{c} + i\frac{\alpha}{2} = 2n_0\varepsilon_0 n_2\omega_0\left|A_s\right|^2 + i\frac{\alpha}{2} \equiv \gamma\left|A_s\right|^2 + i\frac{\alpha}{2} \ . \tag{3.70}$$

Substituting this into Eq. 3.69 yields

$$\frac{\partial A_s}{\partial z} + \frac{1}{2}i\beta_2\frac{\partial^2 A_s}{\partial T^2} + \frac{\alpha}{2}A_s = i\gamma\left|A_s\right|^2 A_s \ . \tag{3.71}$$

Eq. 3.71 describes how an ultrashort pulse with envelope $A_s(z,T)$ propagates through an isotropic nonlinear medium. In the limit that $\alpha = 0$, Eq. 3.71 is called the nonlinear Schrödinger equation (NLSE), and it forms the basis upon which many calculations regarding nonlinear pulse propagation are performed.

3.4 SELF-PHASE MODULATION

Self-phase modulation is a change in the phase of an ultrashort laser pulse due due to nonlinear interaction with the propagation medium via the nonlinear refractive index. It results in a broadening of the pulse spectrum. In this section, we investigate a simple theoretical description of self-phase modulation, assuming an ultrashort pulse with zero initial chirp and a pulse envelope function

$$A_s(z,T) = U(z,T)\exp\left[-\alpha z/2\right]\exp\left[i\phi_{NL}\right] , \tag{3.72}$$

where we have taken account of absorption losses through an average absorption coefficient α. The term ϕ_{NL} in Eq. 3.72 describes the phase shift due to the nonlinear interaction. In order to solve for ϕ_{NL} , we substitute Eq. 3.72 into Eq. 3.71, which describes the evolution of the pulse envelope function as it propagates through a nonlinear medium. In the substitution, we assume that effects due to dispersion are negligible, that is, we assume $\beta_2 \to 0$ [18,38]. This results in the equation

$$\begin{aligned} &\frac{\partial U}{\partial z}\exp\left[-\alpha z/2\right]\exp\left[i\phi_{NL}\right] + i\frac{\partial \phi_{NL}}{\partial z}U\exp\left[-\alpha z/2\right]\exp\left[i\phi_{NL}\right] \\ &\qquad = i\gamma|U|^2 U\exp\left[-\alpha z/2\right]\exp\left[i\phi_{NL}\right] \end{aligned} . \tag{3.73}$$

Collecting and equating real and imaginary terms of Eq. 3.73 yields the following equations:

$$\frac{\partial U}{\partial z} = 0 \tag{3.74}$$

$$\frac{\partial \phi_{NL}}{\partial z} = \gamma|U|^2\exp\left[-\alpha z\right] . \tag{3.75}$$

We see that the function $U(z,T)$ does not change with propagation distance. In order to find the nonlinear phase shift ϕ_{NL}, we integrate Eq. 3.75 with respect to z and require that $\phi_{NL}(0)=0$, yielding

$$\phi_{NL}(z,T)=\gamma\left|U(z,T)\right|^2\frac{\left(1-\exp[-\alpha z]\right)}{\alpha}=\frac{n_2\omega_0}{c}I(z=0,T)\frac{\left(1-\exp[-\alpha z]\right)}{\alpha}, \quad (3.76)$$

where we have made use of the definition of γ in Eq. 3.70. We recall that since the function $U(z,T)$ does not change with propagation distance z it is proportional to the initial intensity $I(z=0,T)$ through the relation $I(0,T)=2n_0\varepsilon_0 c\left|U(0,T)\right|^2$. The maximum nonlinear phase shift occurs, for an ultrashort pulse, at $T=0$. It is often convenient to define an effective path length L_{eff} through a nonlinear medium as well as a nonlinear length L_{NL}:

$$L_{eff}(z)\equiv\frac{1-\exp[-\alpha z]}{\alpha} \quad (3.77)$$

$$L_{NL}\equiv\frac{c}{n_2\omega_0 I_0}\ , \quad (3.78)$$

where $I_0=I(0,0)$. Using the above definitions, we can express the maximum nonlinear phase shift as

$$\phi_{NL}^{\max}(z)=\frac{L_{eff}(z)}{L_{NL}}\ , \quad (3.79)$$

where the length z is the distance that the pulse has propagated in the medium.

The physical significance of the nonlinear length L_{NL} is found in the fact that when the effective distance $L_{eff}(z)$ propagated by the pulse is equal to the nonlinear length L_{NL}, the maximum nonlinear phase shift $\phi_{NL}^{\max} = 1$ [38].

It is often useful to calculate the maximum change in the nonlinear phase shift at $z = \infty$ that can be expected from a pulse with initial intensity I_0 propagating through a medium with average absorption coefficient α. In this case, we look for the phase change

$$\Delta\phi_{NL}^{\max} = \phi_{NL}^{\max}(\infty) - \phi_{NL}^{\max}(0) = \frac{1}{\alpha L_{NL}} \quad . \tag{3.80}$$

In Eq. 3.80 we have assumed a medium with infinite dimensions. However, for a medium with a finite propagation length L, the maximum nonlinear phase shift is given by $\Delta\phi_{NL}^{\max} = L_{eff}(L)/L_{NL}$, as shown in Eq. 3.79.

We can investigate how self-phase modulation changes the spectrum of an ultrashort pulse through Fourier transformation of the electric field waveform, taking into account the nonlinear phase shift. We assume a Gaussian pulse envelope function $U(z,T)$ with an intensity FWHM pulse duration τ_0 of 30 fs:

$$U(z,T) = E_0 \exp\left[-\frac{(2\ln 2)T^2}{\tau_0^2}\right], \tag{3.81}$$

resulting in an electric field of the form

$$E(z,T) = E_0 \exp\left[-\frac{(2\ln 2)T^2}{\tau_0^2} - \frac{\alpha z}{2}\right] \exp\left[i\left(k_0 z - \omega_0 T + \phi_{NL}\right)\right], \tag{3.82}$$

where we have used Eqs. 3.52 and 3.72. Utilizing Eq. 3.76, we note that the nonlinear phase shift is

$$\begin{aligned}\phi_{NL}(z,T) &= \frac{n_2\omega_0 I_0}{c}\exp\left[-\frac{(4\ln 2)T^2}{\tau_0^2}\right]\frac{\left(1-\exp[-\alpha z]\right)}{\alpha} \\ &= \phi_{NL}^{\max}(z)\exp\left[-\frac{(4\ln 2)T^2}{\tau_0^2}\right]\end{aligned} . \tag{3.83}$$

We then calculate the spectral intensity $S(\omega)$ according to

$$S(\omega) = |E(\omega)|^2 = E_0^2\exp[-\alpha z]\left|\int_{-\infty}^{\infty}\exp\left[-\frac{(2\ln 2)T^2}{\tau_0^2} - i(\omega_0-\omega)T + i\phi_{NL}(z,T)\right]\right|^2 , \tag{3.84}$$

where $\phi_{NL}(z,T)$ is given by Eq. 3.83. We can rewrite Eq. 3.84 in the form $S(\omega) = E_0^2\exp[-\alpha z]F(\omega)$ where

$$F(\omega) = \left|\int_{-\infty}^{\infty}\exp\left[-\frac{(2\ln 2)T^2}{\tau_0^2} - i(\omega_0-\omega)T + i\phi_{NL}(z,T)\right]\right|^2 . \tag{3.85}$$

Figure 3.1 shows $F(\omega)$ for a 30 fs ultrashort laser pulse centered at $\omega_0 = 2.3562\, fs^{-1}$ ($\lambda_0 = 800\, nm$) as a function of $\phi_{NL}^{\max}(z)$. $\phi_{NL}^{\max}(z)$ ranges from 0 to $9\pi/2$. In Fig. 3.1, the vertical axis shows the quantity $\phi_{NL}^{\max}(z)/\pi$. One can see that as the magnitude of $\phi_{NL}^{\max}(z)$ increases, the spectrum of the pulse spreads and acquires an increasing number of spectral node structures.

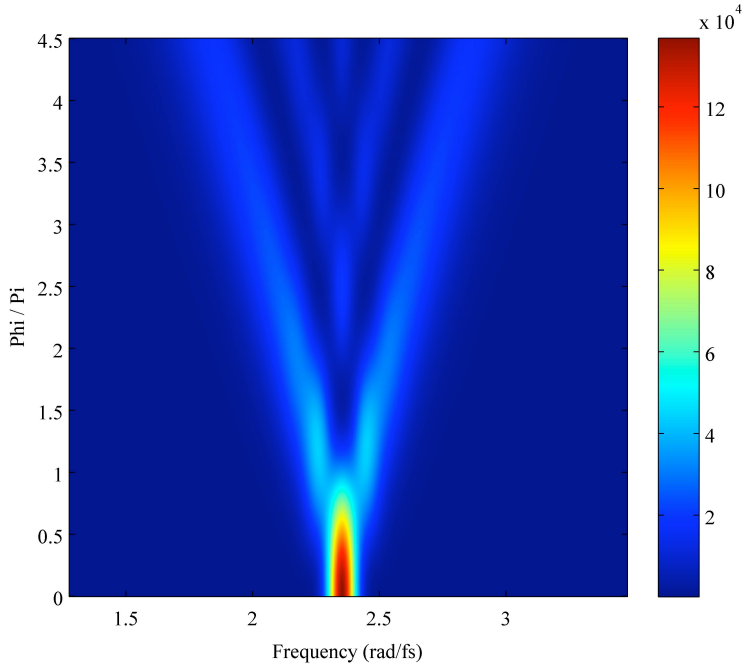

Fig. 3.1 Self-phase modulation of the spectrum of a 30 fs FWHM pulse with central frequency $\omega_0 = 2.3562$ as a function of $\phi_{NL}^{\max}(z)$ as shown in Eq. 3.83. The vertical axis shows the quantity $\phi_{NL}^{\max}(z)/\pi$.

It is important to note that, as the pulse broadens due to self-phase modulation, it does not remain transform-limited: it acquires a frequency chirp. By taking the time derivative of Eq. 3.82, it is easy to show that the instantaneous frequency of the pulse $\omega(t)$ is given by

$$\omega(t) = \omega_0 + \frac{d\phi_{NL}(z,T)}{dT} \quad . \tag{3.86}$$

Since $\phi_{NL}(z,T)$ is given in Eq. 3.83, the time derivative has the form

$$\frac{d\phi_{NL}(z,T)}{dT} = \phi_{NL}^{\max}(z)\left(\frac{(8\ln 2)T}{\tau_0^2}\right)\exp\left[-\frac{(4\ln 2)T^2}{\tau_0^2}\right] . \tag{3.87}$$

In Fig. 3.2 is graphed the normalized intensity of a 30 fs FWHM laser pulse along with the corresponding change in instantaneous frequency as given in Eq. 3.87. The right panel in Fig. 3.2 shows the quantity $\frac{d\phi_{NL}(z,T)}{dT} / \phi_{NL}^{\max}(z)$.

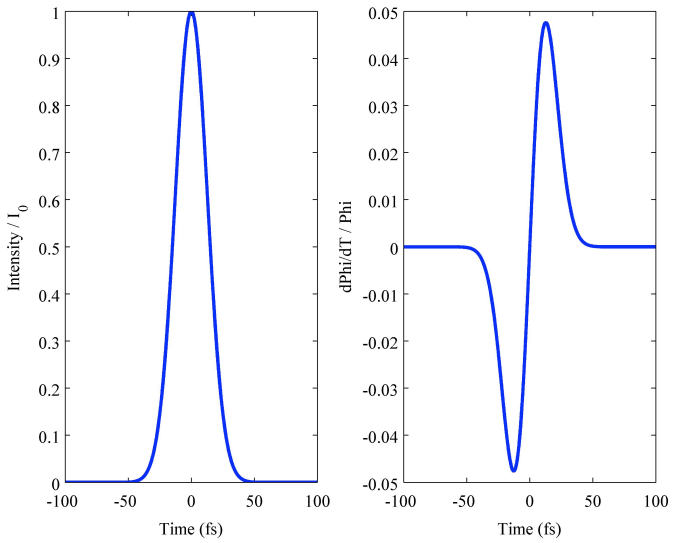

Fig. 3.2 Normalized intensity (left panel) of a 30 fs FWHM pulse with central frequency $\omega_0 = 2.3562$. The right panel shows the change in instantaneous frequency as a function of time. The vertical axis corresponds to the quantity $\left(d\phi_{NL}(z,T)/dT\right)/\phi_{NL}^{\max}(z)$.

We note that, in the above analysis, we have assumed that dispersion is negligible and that the pulse is transform limited at $z = 0, T = 0$. Figure 3.2 illustrates the fact that, independently of dispersion, an initially transform-limited pulse becomes positively chirped as it experiences self-phase modulation, with lower frequencies leading the pulse and higher frequencies trailing the pulse.

We have seen how an ultrashort pulse propagating in a nonlinear medium experiences spectral broadening as a result of a self-induced phase shift due to a nonlinear interaction involving the nonlinear, intensity-dependent refractive index n_2. In the next section, we will investigate how the temporal envelope of the pulse also changes as a result of nonlinear pulse propagation.

3.5 SELF-STEEPENING

Self-steepening results from the intensity dependence of the group velocity of an ultrashort laser pulse. It can be an important effect for femtosecond pulses propagating in a nonlinear medium. Self-steepening results in an asymmetry in the self-phase modulated pulse spectrum [18,38,39].

In order to gain an intuitive understanding of the phenomenon of ultrashort laser pulse self-steepening, we seek to describe it with a simple mathematical model. Self-steepening is due to a higher order term in the nonlinear Schrödinger equation (NLSE) that has been left out of Eq. 3.71. This higher order term describes how the pulse envelope changes in time as the pulse propagates in a nonlinear medium. The modified NLSE, which contains this higher order term, can be written as [38,39]

$$\frac{\partial A_s}{\partial z}+\frac{1}{2}i\beta_2\frac{\partial^2 A_s}{\partial T^2}+\frac{\alpha}{2}A_s=i\gamma\left|A_s\right|^2A_s-\frac{\gamma}{\omega_0}\frac{\partial}{\partial T}\left(\left|A_s\right|^2A_s\right)\ . \tag{3.88}$$

For the sake of simplicity of argument, we assume that both absorption and dispersion are negligible. In this case, Eq. 3.88 may be rewritten as

$$\frac{\partial A_s}{\partial z}=i\gamma\left|A_s\right|^2A_s-\frac{\gamma}{\omega_0}\frac{\partial}{\partial T}\left(\left|A_s\right|^2A_s\right)\ . \tag{3.89}$$

We assume a pulse envelope of the form

$$A_s(z,T) = U(z,T)\exp\left[i\phi_{NL}(z,T)\right] , \tag{3.90}$$

where $U(z,T)$ is a real quantity. Substituting Eq. 3.90 into Eq. 3.89 and equating real and imaginary terms yields the following two equations:

$$\frac{\partial U}{\partial z} + \frac{3\gamma}{\omega_0} U^2 \frac{\partial U}{\partial T} = 0 \tag{3.91}$$

$$\frac{\partial \phi_{NL}}{\partial z} - \gamma U^2 + \frac{\gamma}{\omega_0} U^2 \frac{\partial \phi_{NL}}{\partial T} = 0 \ . \tag{3.92}$$

While Eq. 3.92, which contains information regarding the nonlinear phase ϕ_{NL}, requires an involved detailed analysis to solve [39], Eq. 3.91 may be solved easily because it is independent of ϕ_{NL}. The solution is given in [39] to be

$$U(z,T) = \sqrt{f\left(T - \frac{3\gamma z}{\omega_0} U(z,T)^2\right)} , \tag{3.93}$$

where f is an arbitrary function that is determined by the initial form of the pulse envelope. For a Gaussian pulse with intensity FWHM $\tau_0 = 30\ fs$, we can write the function f as

$$f(z,T) = A_0^2 \exp\left[-\frac{(4\ln 2)\left(T - \frac{3\gamma z}{\omega_0} U(z,T)^2\right)^2}{\tau_0^2} \right] . \tag{3.94}$$

We recall that $I(z,T) = 2n_0\varepsilon_0 c\left|A_s\right|^2$. We can therefore write the intensity of the ultrashort pulse as it propagates through the medium as

$$I(z,T) = I_0 \exp\left[-\frac{(4\ln 2)\left(T - \frac{3z}{\omega_0 I_0 L_{NL}} I(z,T) \right)^2}{\tau_0^2} \right]. \tag{3.95}$$

Figure 3.3 presents a numerical solution to Eq. 3.95 using an iterative algorithm of the form

$$\frac{I(\mu,T_i)}{I_0} = \exp\left[-\frac{(4\ln 2)\left(T - \frac{3\mu}{\omega_0} \frac{I(\mu,T_{i-1})}{I_0} \right)^2}{\tau_0^2} \right], \tag{3.96}$$

where $\mu = z / L_{NL}$ and

$$\frac{I(\mu,T_{i=1})}{I_0} = \exp\left[-\frac{(4\ln 2)(T_{i=1})^2}{\tau_0^2} \right]. \tag{3.97}$$

The calculation was performed for a Gaussian pulse with intensity FWHM $\tau_0 = 30\, fs$, from times spanning -100 fs to 100 fs with a time step of 0.02 fs, which is sufficiently small to produce accurate results.

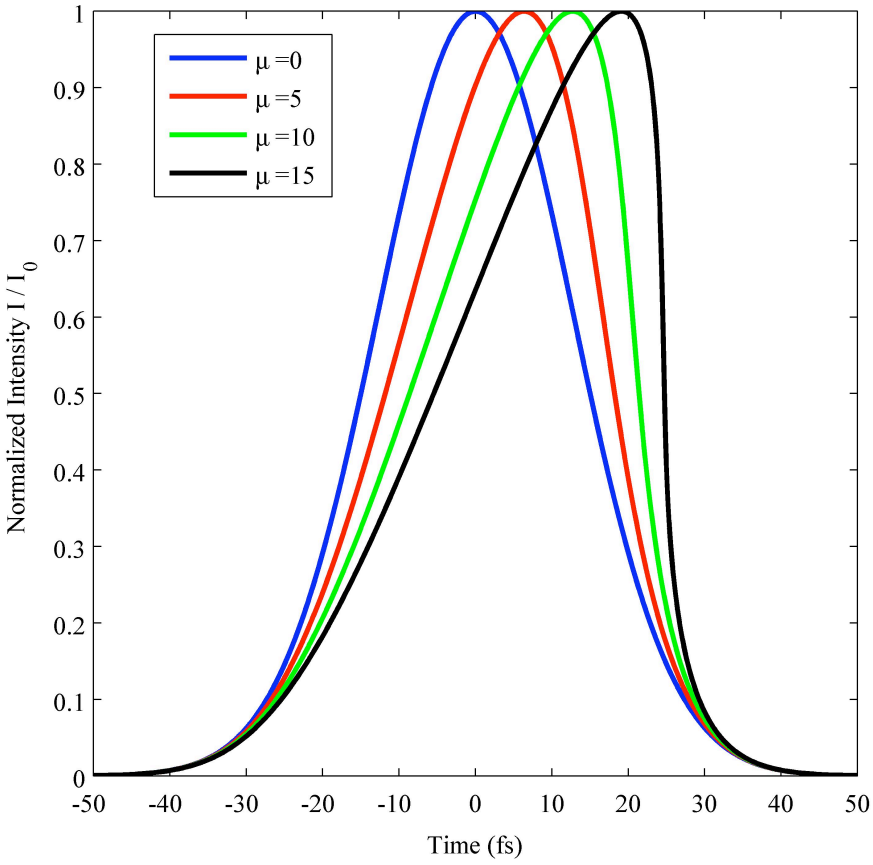

Fig. 3.3 Normalized intensity of a 30 fs FWHM pulse with central frequency $\omega_0 = 2.3562$ which has experienced self-steepening over various values of $\mu = z / L_{NL}$.

In Fig. 3.3, it can be seen that as the pulse propagates to greater $\mu = z / L_{NL}$, the trailing edge of the pulse becomes steeper and steeper. Eventually, in the absence of dispersion and absorption, the trailing edge of the pulse will have an infinite slope, corresponding to an optical shock wave. However, in practice, both dispersion and absorption work keep the slope of the trailing edge finite [38,39].

Self-steepening results in an asymmetric self-phase modulated spectrum. In particular, the higher frequencies toward the blue end of the spectrum experience greater broadening. This may be understood through the shape of the intensity profile. As the trailing edge of the pulse becomes steeper and steeper, it corresponds to greater broadening of high-frequency components, which combine to form the sharp intensity drop on the trailing edge of the pulse. The asymmetric pulse intensity profile and the asymmetric pulse broadening are, then, part of the same phenomenon [38].

In the previous sections, we detailed some important nonlinear phenomena in ultrashort pulse propagation. In the following section, we outline an experiment which details the onset of nonlinear pulse propagation in liquid water using femtosecond laser pulses.

3.6 PROPAGATION OF ULTRASHORT LASER PULSES IN WATER: LINEAR ABSORPTION AND ONSET OF NONLINEAR SPECTRAL TRANSFORMATION

3.6.1 Description of hole filling technique for investigation of nonlinearities

In Section 2.8 we outlined various claims of violations of the Bougeur-Lambert-Beer (BLB) law [30,33,34] and showed, in agreement with several other works [35,36], that these claims of violations of the BLB law within the linear pulse propagation regime were unfounded [8]. In these studies, special care was taken to make sure the light field was sufficiently weak to avoid any possible sources of nonlinearity. Since this subject

area is of substantial fundamental significance and has potential implications to such important applications as underwater communications and biomedical imaging, it warrants further investigation.

The scope of the present study is twofold: (1) We perform a balanced side-by-side comparison of water absorption for weak laser pulses of different duration, aiming to detect small (fraction of a percent level) duration-dependent differences. We employ a spectral hole-filling technique developed by Warren and coworkers [40], where a short pulse and a long pulse (of the same spectral intensity at the same center wavelength but with opposite phase) are added coherently to produce a spectral distribution with a narrow gap (hole). In this situation, any pulse duration dependent absorption is expected to result in "filling" of this hole. (2) We quantify the transition from linear to nonlinear pulse propagation in water. We proceed by first reviewing the basics of our technique, and then we describe experimental results for pulses with peak intensities varied over many orders of magnitude. Electric fields of two coherent laser pulses (a short and a long one) of the same spectral intensity at the same center frequency ω_c, but with opposite phase, add up to produce a spectrum with a hole, since at ω_c the two contributions exactly cancel:

$$E(\omega) = A\left(\exp\left[-\frac{(\omega-\omega_c)^2}{8\ln 2}\tau_1^2 \right] - \exp\left[-\frac{(\omega-\omega_c)^2}{8\ln 2}\tau_2^2 \right] \right) \tag{3.98}$$

$$E(t) = B\left(\exp\left[-(2\ln 2)\left(\frac{t}{\tau_1}\right)^2 \right] - \frac{\tau_1}{\tau_2}\exp\left[-(2\ln 2)\left(\frac{t}{\tau_2}\right)^2 \right] \right)\cos(\omega_c t), \tag{3.99}$$

where $E(\omega)$ is the spectral amplitude, $E(t)$ is the amplitude of the electric field in the time domain, and τ_1 and τ_2 are the intensity full width at half maximum (FWHM) pulse durations. When the resultant waveform is sent through a linear absorbing or scattering medium, this balance will persist if the absorption is independent of pulse duration. Any absorption that would effect the longer and shorter pulses differently would inevitably destroy the perfect destructive interference at the center wavelength and result in the filling of the spectral hole.

3.6.2 Experiments with femtosecond oscillator pulses

To study spectral hole filling experimentally, we use an ultrabroadband mode-locked femtosecond Ti:sapphire oscillator (Rainbow, FemtoLasers) followed by an acousto-optic programmable pulse shaper (Dazzler, FastLite) to obtain a broad, smooth spectrum with a spectral hole whose position and width can be precisely controlled. The laser oscillator produces pulses of 7 fs duration with a spectrum that extends from 660 to 980 nm; its average output power is 340mW, and the repetition rate is 78MHz, so that the energy per pulse is about 4 nJ. We set the Dazzler to reduce the full spectral bandwidth to 80 nm. The width of the hole is chosen to be 10 nm, and for three measurements its center is positioned at three different wavelengths, i.e., at 767 nm, 800 nm, and 827nm. Note that the pulse shaper is capable of compensating additional dispersion (including its own dispersion) and therefore allows synthesis of transform-limited waveforms. Assuming a constant spectral phase, we calculate pulse shapes, which indeed contain long- and short duration components (200 fs and 25 fs,

respectively), as drawn in Fig. 3.4, which also shows an experimental setup.

The resultant shaped pulses are directed to a cylindrical glass cell (1.5 m in length) containing distilled water. Laser light emerging from the water cell is focused by a lens and scatters off a white screen vibrating at a 50 Hz rate; then a fraction of it couples

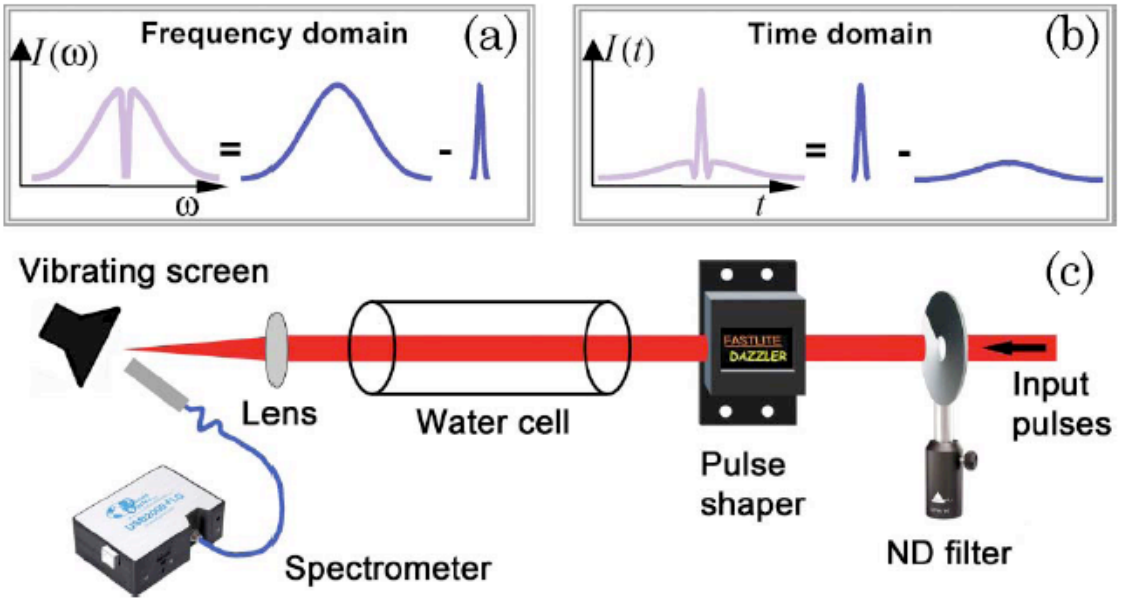

Fig. 3.4 Spectral-hole-filling experiment: (a) Frequency domain and (b) time domain schematics. (c) Experimental setup (femtosecond laser oscillator not shown). Initial 7 fs laser pulses pass through the pulse shaper, which produces a spectral hole and reduces the total spectral bandwidth, and enter the water cell. The transmitted spectra are measured by the spectrometer [9].

into a fiber and is detected by a spectrometer (USB 2000, Ocean Optics). This configuration is used in order to make the measurement insensitive to small variations of laser beam alignment; the screen vibration reduces the possible effects of intensity speckles and diffraction that result in fluctuating modulations of the measured spectrum. We check that the reshaping of the spectra (water cell input, Figs. 3.5(a-c), versus

output, Figs. 3.5(d-f)) is mostly consistent with linear absorption in water (which is strongly wavelength dependent), although these present experiments are not optimized for measuring the wavelength-dependent absorption as reliably as some of our earlier experiments were [8].

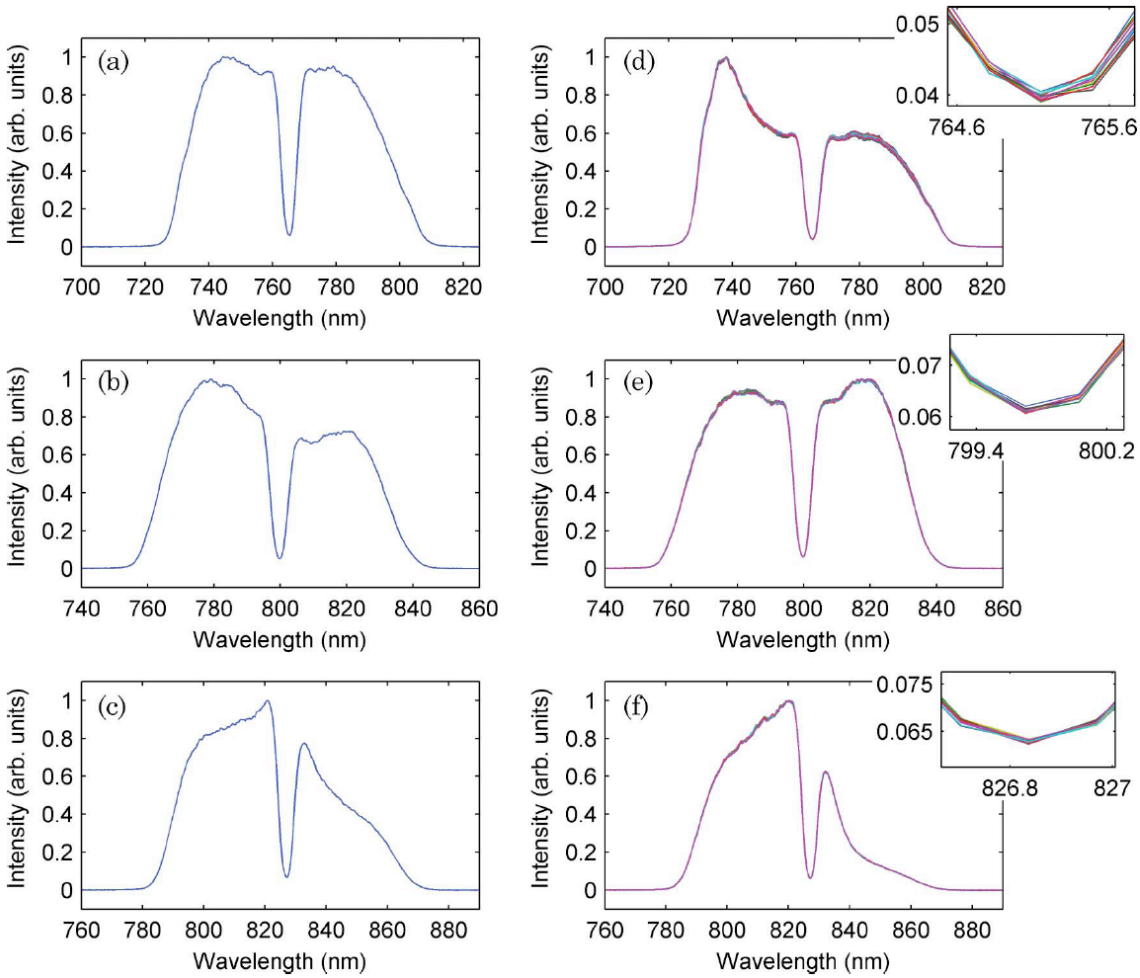

Fig. 3.5 Results from the spectral hole filling experiment with low-power (laser oscillator) shaped pulses. Parts (a)–(c) show input spectra with the spectral hole centered at (a) 767 nm, (b) 800 nm, and (c) 827nm wavelengths. Parts (d)–(f) show the corresponding output spectra after propagation through 1.15m of distilled water; insets show zoomed-in spectral hole regions [9].

We vary laser power at the input of the water cell from 1mW to 12mW in 1mW increments using a neutral density filter while recording the output spectra (Figs. 3.5(d-f)). To compare the shapes of the spectra for different input powers, we first take the data and divide each measured spectral curve by the corresponding input power. This procedure by itself produces curves deviating from each other by no more than the relative uncertainty of our power measurements (with the absolute experimental uncertainty of 0.1mW, the relative uncertainty varies from 10% for 1mW of input power to 0.8% for 12 mW). To avoid these variations due to uncertainty in the power measurements, we normalize each curve to its peak value, in order to be able to look at possible small (well less than 1%) relative variations in the resultant spectral shapes. The insets shown in Figs. 3.5(d-f) illustrate an essential absence of a mismatch among different curves at the spectral hole wavelengths. This mismatch is less than 0.1% of the peak value and is within the spectrometer noise. The above results, to within our precision of 0.1% showing no "hole filling," indicate that absorption affects a 25 fs pulse exactly the same way it affects a 200 fs pulse. For a linear regime this is as expected, since new frequency components can only appear as a result of nonlinear generation. Simple estimates show that in the experiments with the oscillator pulses, we are well below intensity levels required for any nonlinear effects (i.e., self-focusing or self-phase modulation) to occur.

3.6.3 Experiments with amplified pulses: transition to the nonlinear regime

To investigate the propagation of laser pulses in a broad range of intensities and to quantify the transition to nonlinear behavior, we used amplified laser pulses. Figure 3.6 shows a schematic of our experimental setup: after amplification (Femtopower multipass system from Femtolasers) a spectral hole with the central wavelength of 794 nm is produced in the pulse spectrum by placing an obstruction that blocks a narrow spectral interval in the compressor (see Fig. 3.6). The resultant spectrum is centered at 800 nm and has a total bandwidth of about 70 nm and a spectral hole width of 20 nm (corresponding to 30 fs and 100 fs pulse durations, respectively). The pulse repetition rate is 5 kHz. The laser pulses propagate through a variable neutral density filter and then through a telescope, which reduces the beam size by a factor of 3 (to a waist of 2.1 mm). The collimated laser beam passes through the glass window and enters the water sample. After propagating the single-pass length of 1.15 m in distilled water, the pulses are scattered off of a vibrating white screen and measured with a fiber-coupled spectrometer, similar to the above-described experiment with laser oscillator pulses. The input power is measured by redirecting the laser beam to a powermeter (Nova II, Ophir) with a removable mirror just before the water cell.

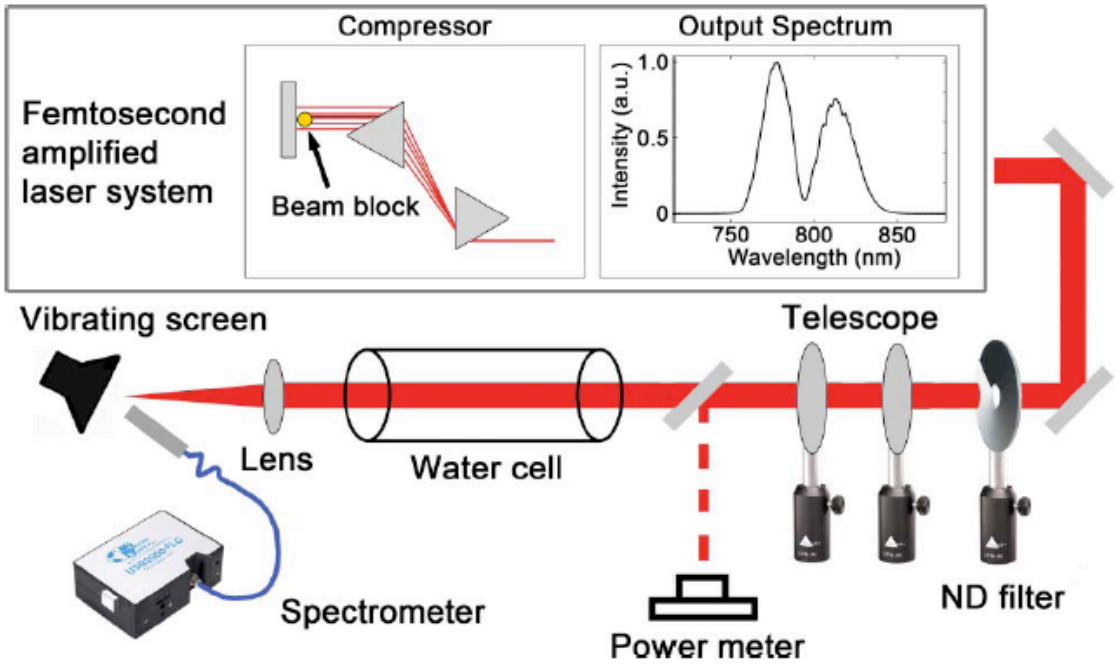

Fig. 3.6 Experimental setup for measuring propagation of amplified laser pulses through water. An obstruction is placed in the compressor to produce a hole in the laser spectrum. Then the pulses propagate through the water cell, and the transmitted spectra are measured by the spectrometer [9].

Figure 3.7(a) shows the dependence of the transmitted pulse spectrum on the input power. Each curve has been normalized to the peak value of the spectrum obtained at 340 mW of input power. The curves are vertically displaced, with greater input powers corresponding to greater upward vertical displacement. It can be seen that, as input power increases, the hole begins to fill in and also shifts somewhat from the initial wavelength of 794 nm toward smaller wavelengths at higher input powers. In addition, the wings of the spectrum experience broadening. Figure 3.7(b) shows the differential changes of the spectrum at different power levels. Each of the shown curves was obtained with the following procedure: a spectrum, calculated assuming linear behavior,

is subtracted from the measured spectrum and divided by the input power; each resultant curve is then scaled relative to the obtained peak value of the curve corresponding to an input power of 200 mW. As can be seen in the figure, the energy from the intense spectral components is transferred to the hole and wings (i.e., to spectral components of low intensity) as the input power increases. We note that this behavior is reminiscent of diffusion, with a spectral diffusion coefficient increasing with the laser power.

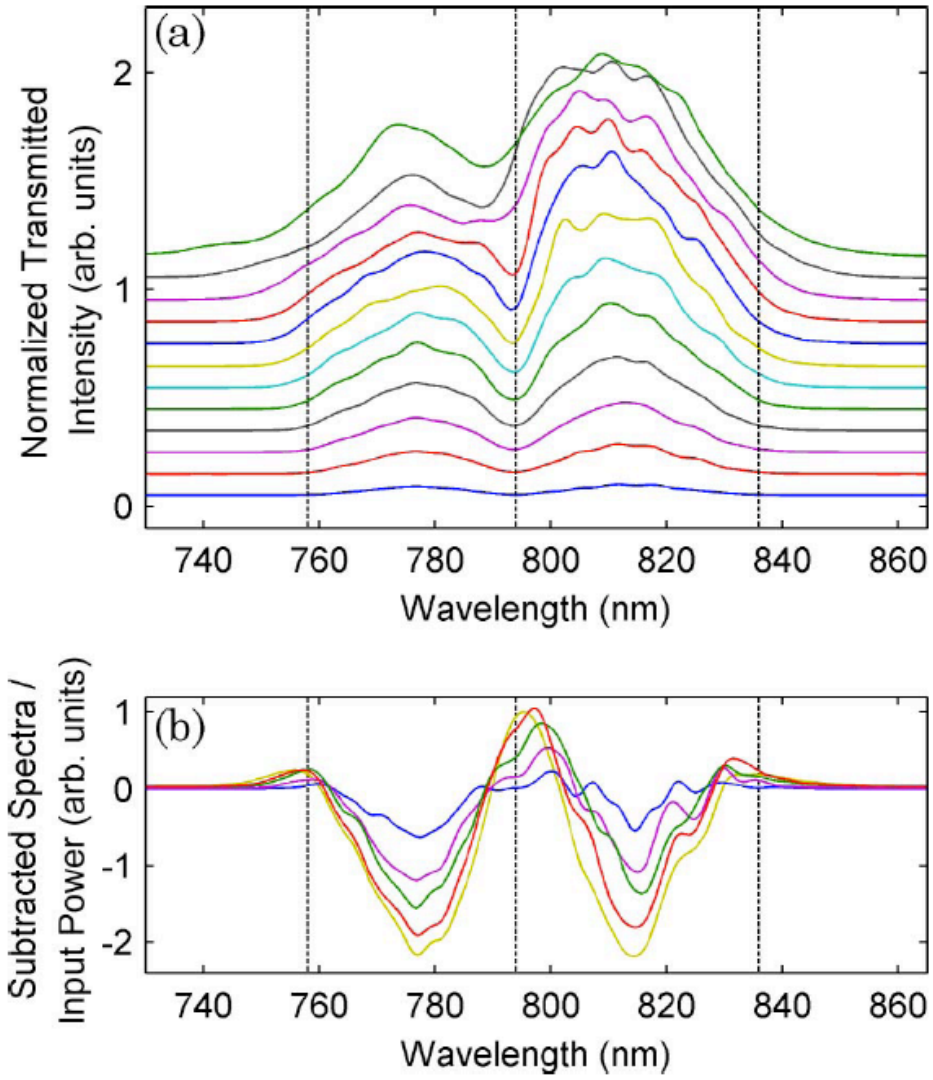

Fig. 3.7 Transformation of transmitted spectra with increasing input laser power: (a) Measured spectra. To aid in visualization, each spectrum has been vertically displaced, with larger upward vertical displacements corresponding to larger input powers. The input powers for the shown spectra are, from bottom to top: 5 mW, 15 mW, 25 mW, 40 mW, 60 mW, 80 mW, 100 mW, 120 mW, 140 mW, 180 mW, 250 mW, and 340 mW. (b) Changes in the spectrum, relative to spectra expected for linear transmission and calculated by scaling the output spectrum obtained for 20 mW input power. These curves are obtained by subtracting the expected linear-transmission spectra from the actual measured spectra, dividing by the input power, and scaling relative to the peak value obtained in the 200 mW curve. The input powers shown, with increasing spectral transformation, are 40 mW, 80 mW, 120 mW, 160 mW, and 200 mW. In both (a) and (b), dotted vertical lines correspond to wavelengths of 794 nm (spectral hole center at low power), and two wavelengths at the wings of the spectrum, 758 and 836 nm [9].

Figure 3.8 shows the measured transmitted spectral intensities at three wavelengths (marked in Fig. 3.7 by dotted vertical lines) as a function of the input power. The three wavelengths correspond to the low-power spectral hole center (794 nm) and two wavelengths at the spectral wings (758 and 836 nm) having, at low input powers, the same spectral intensity as the hole center. At low input powers (below about 40 mW), we observe linear growth of the spectral intensities, turning to nonlinear behavior at higher input powers.

This behavior can be seen especially clearly on the logarithmic plot of the transmitted spectral intensity at the hole central wavelength of 794 nm as a function of the input power (see Fig. 3.9). A significant (1% compared to the peak spectral intensity) deviation from the linear behavior starts at around 40 mW power, which correspond to a peak value of 0.12 mJ/cm^2 of input laser energy fluence and, given the pulse durations used, to a peak intensity of about 10^{10} W/cm^2. Above input powers of 40 mW, the spectral intensity at 794 nm exhibits quadratic growth. A new drastic change in the behavior happens at around 250 mW (which corresponds, for the parameters of our experiment, to a peak input fluence of 0.73mJ/cm^2).

The quadratic power dependence may result from a third-order nonlinear mixing process (please note that second-order nonlinearities are forbidden in centrosymmetric media such as liquid water). As a likely possibility, we consider two-photon processes such as stimulated Raman scattering (SRS). At powers above 100 mW we find that the spectral hole position (the location of the minimum in the output spectrum) shifts toward shorter wavelengths; this behavior is also consistent with SRS, which converts shorter

wavelength photons to longer-wavelength ones. It should be pointed out that even though SRS is a likely process to come into play first, as the laser intensity is gradually increased, many other phenomena such as thermal lensing, self-focusing, self-phase modulation, and medium ionization all become significant at somewhat higher intensities [41–43]. In our experiment we observe an interplay of these effects at powers above 250 mW; however, detailed investigation of these phenomena is beyond the scope of our present work.

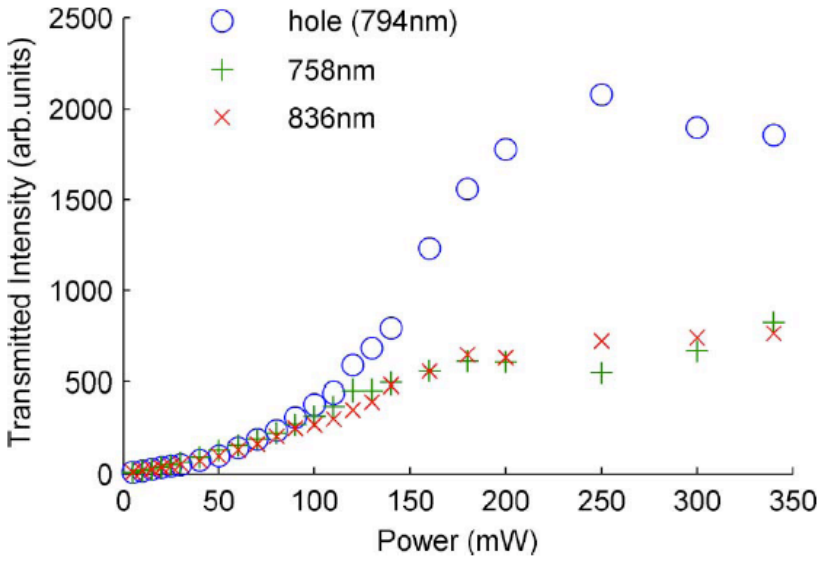

Fig. 3.8 Transmitted intensity for three wavelengths as a function of input laser power. The three wavelengths correspond to the low-power spectral hole center (794 nm) and two wavelengths at the spectral wings (758 and 836 nm) having, at low input powers, the same spectral intensity as the hole center [9].

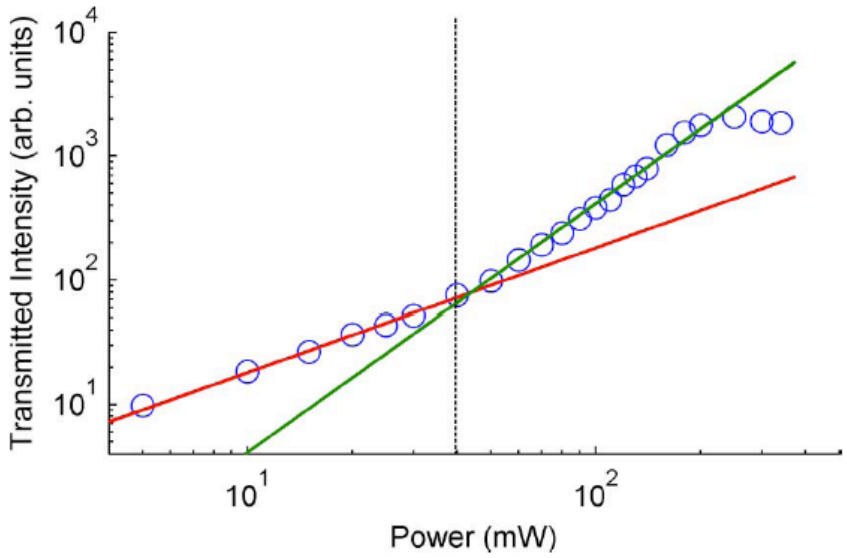

Fig. 3.9 Plot on a log-log scale of transmitted spectral intensity at 794nm (initial spectral hole center) as a function of the input power. The blue circles show the measured data. The red reference line has a slope of 1 and fits well to the data points in the low-power region, indicating a linear dependence. The green reference line has a slope of 2 and fits the data points in the region of intermediate power up to about 250mW, indicating a quadratic dependence. The change from the linear dependence to quadratic dependence can be clearly seen at around 40mW (where a dotted vertical line is drawn) [9].

3.6.4 Onset of nonlinear pulse propagation in water

We have investigated propagation of femtosecond laser pulses with the central wavelength around 800 nm in water by employing a spectral hole filling technique. We showed experimentally and with precision of better than 0.1% that there is no pulse duration dependent absorption for ultrashort pulses of duration around 30 fs in the linear light–matter interaction regime. We then quantified the transition of such pulse behavior from the linear to the nonlinear interaction regime, and we found that this transition occurs at around 0.12 mJ/cm^2. Above this value a quadratic growth of the intensity at the spectral hole was observed up to about 0.73 mJ/cm^2. Also, we found that as the light–

matter interaction becomes increasingly nonlinear, the location of the minimum in the output spectrum shifts toward shorter wavelengths. We suggest stimulated Raman scattering as a possible mechanism for this spectral hole filling and shifting effect. However, it should be pointed out that many other phenomena, such as thermal lensing, self-focusing, self-phase modulation, and medium ionization can affect propagation of short and intense laser pulses in the nonlinear regime, and the detailed investigation of these mechanisms is certainly out of the scope of this study.

The main conclusion is that no violations of the BLB law in the linear light–matter interaction regime was registered in this work. It may still be a matter of debate whether pulses of any duration, most significantly durations that are a small fraction of the vibrational periods of water molecules, will induce a violation of the BLB law; however, we can now state that none have yet been documented. As we have shown, due to dispersion, ultrashort pulses become increasingly fragile as their duration decreases, so that they can maintain their pulse duration on correspondingly decreasing distances (less than a millimeter for sub-10 fs pulses), unless a special compensation of the dispersion spreading is implemented.

CHAPTER IV

FEMTOSECOND LASER PULSE FILAMENTATION*

Femtosecond filamentation is a highly-nonlinear optical phenomenon involving the propagation of intense ultrashort laser pulses through transparent (or mostly transparent) media*. There is now an extensive and continuously increasing body of literature on the subject, and experts in the field have undertaken the writing of basic textbooks on the subject [44]. Potential applications of filamentation include generation of attosecond laser pulses, remote sensing techniques, and a host of other methods that is always increasing. Within the context of this dissertation, femtosecond laser pulse filamentation is included based upon its potential use in remote sensing applications.

Femtosecond laser pulse filamentation involves three basic phenomena: (1) self-focusing of an intense ultrashort laser pulse due to the intensity-dependent nonlinear refractive index n_2, (2) intensity clamping due to atomic and/or molecular ionization and subsequent balance of focusing and defocusing mechanisms, and (3) conical emission of electromagnetic radiation. While all three of these phenomena are often present during the process of filamentation, a minimal definition of the process and phenomenon of filamentation has been suggested to include only (1) and (2), that is, self-focusing and intensity clamping [44].

---

* Reprinted with permission from "Energy transfer between laser filaments in liquid methanol" by B. D. Strycker, M. Springer, C. Trendafilova, X. Hua, M. Zhi, A. A. Kolomenskii, H. Schroeder, J. Strohaber, H. A. Schuessler, G. W. Kattawar, and A. V. Sokolov, 2012. *Optics Letters*, 37, 16-18, Copyright 2012 by Optical Society of America.

This dissertation cannot possibly explore all that there is to know about femtosecond laser filamentation, as the field is now very broad. However, we will investigate the main mechanisms behind the phenomena involved in the minimal definition of filamentation described above, which involves self-focusing and intensity clamping of an intense femtosecond laser pulse. The next two sections detail the processes behind these mechanisms. At the end of the chapter, we describe an experiment involving energy transfer between two crossed filaments in liquid methanol.

4.1 SELF-FOCUSING OF AN INTENSE FEMTOSECOND LASER PULSE

In Section 3.2 we investigated the origin of the nonlinear intensity-dependent refractive index n_2. In this section we investigate how the nonlinear refractive index can lead to self-focusing of an intense femtosecond laser pulse. We define the nonlinear intensity-dependent refractive index as

$$n = n_0 + n_2 I \ , \tag{4.1}$$

where I is the intensity of the pulse. However, most laser pulses propagate within a beam of a particular intensity profile. We assume here a Gaussian beam profile:

$$I(r,T) = I_0 \exp\left[-\frac{2r^2}{w_0^2}\right]\exp\left[-\frac{(4\ln 2)T^2}{\tau_0^2}\right], \tag{4.2}$$

where w_0 is the intensity e^{-2} beam waist, T is the time in the frame moving with the pulse, and τ_0 is the intensity FWHM temporal duration of the pulse. Self-focusing is an action resulting from the transverse spatial profile from a pulse (for example, Eq. 4.2). A complete treatment of self-focusing, then, requires a numerical solution of the NLSE

equation with inclusion of the transverse spatial derivatives. Marburger [45] has provided a thorough treatment of self-focusing through numerical analysis of a nonlinear pulse propagation equation of the form

$$\frac{\partial A_s}{\partial z} + \frac{1}{2}\nabla_\perp^2 A_s = i\gamma \left|A_s\right|^2 A_s \ , \tag{4.3}$$

where

$$\nabla_\perp^2 = \frac{\partial^2}{\partial x^2} + \frac{\partial^2}{\partial y^2} \ . \tag{4.4}$$

In this analysis, he has neglected effects due to dispersion and pulse attenuation; however, his analysis has been proven to be quite accurate and useful in many instances [44]. Other analyses have also been performed investigating equations similar to Eq. 4.3 [46]. While a numerical analysis that does justice to the full evolution of a pulse that propagates according to Eq. 4.3 is beyond the scope of this dissertation, we may obtain an intuitive and insightful understanding of the mechanisms responsible for self-focusing through an analytical analysis of a simplified picture of the following nature: we assume a thin nonlinear medium of length L through which an intense pulse propagates, experiencing neither beam divergence due to diffraction nor spectral dispersion nor attenuation. As such, the pulse acquires only a nonlinear phase shift ϕ_{NL} that is dependent upon the radially-dependent intensity of the pulse, according to Eq. 4.2. After the pulse exits the thin nonlinear medium, it propagates according to linear pulse propagation theory. Such a scenario is indeed greatly simplified; however, it was considered in Marburger's seminal analysis of self-focusing [45] and still provides an

illustration of the key components of self-focusing that are relevant to femtosecond pulse filamentation.

We begin by noting that a thin lens composed of glass, fused-silica, or a similar material imparts a radially-dependent phase shift upon a pulse (as a function of distance from the axis of the lens and, if the pulse axis coincides with that of the lens, the axis of the pulse) of the form [47]:

$$E(r,T)' = \varphi(r)E(r,T) \ , \tag{4.5}$$

where $E(r,T)'$ is the field of the pulse just after the lens, $E(r,T)$ is the pulse just before the lens, and $\varphi(r)$ is the term that contains the phase imparted to the pulse by the lens and is of the form

$$\varphi(r) = \exp\left[-i\frac{k_0}{2f}r^2 \right] . \tag{4.6}$$

In Eq. 4.6, f is the focal length of the lens.

We now consider a thin nonlinear medium of length L, through which a pulse propagates. We assume that the medium is sufficiently thin that divergence, dispersion, and attenuation may be neglected. Then, according to a pulse spatial intensity profile according to Eq. 4.2, and utilizing our knowledge of the nonlinear phase imparted to the pulse due to the nonlinear refractive index n_2 as shown in Eq. 3.76, the phase imparted to the pulse is

$$\phi_{NL}(r,T) = \frac{L}{L_{NL}}\frac{I(r,T)}{I_0} = \frac{L}{L_{NL}}\exp\left[-\frac{2r^2}{w_0^2} \right]\exp\left[-\frac{(4\ln 2)T^2}{\tau_0^2} \right] . \tag{4.7}$$

In Eq. 4.7, we have used the definition of L_{NL} according to Eq. 3.78. We have also used the fact that, in Eq. 3.77, the limit as the absorption coefficient $\alpha \to 0$ is

$$\lim_{\alpha \to 0} \frac{1 - \exp[-\alpha z]}{\alpha} = z \ . \tag{4.8}$$

We now expand the nonlinear phase of Eq. 4.7 into a Taylor series in *r*, retaining only first two terms. This gives us a first order approximation to how the radial profile of the pulse affects the nonlinear phase, resulting in

$$\phi_{NL}(r,T) = \frac{L}{L_{NL}}\left(1 - \frac{2r^2}{w_0^2}\right)\exp\left[-\frac{(4\ln 2)T^2}{\tau_0^2}\right] . \tag{4.9}$$

The field of the pulse just after passing through the nonlinear medium of length L may then be described according to the forms of Eqs. 4.5 and 4.6, where the initial field is modified by a phase term of the form

$$\varphi(r,T) = \exp\left[i\frac{L}{L_{NL}}\exp\left[-\frac{(4\ln 2)T^2}{\tau_0^2}\right]\right]\exp\left[-i\frac{L}{L_{NL}}\frac{2r^2}{w_0^2}\exp\left[-\frac{(4\ln 2)T^2}{\tau_0^2}\right]\right] . \tag{4.10}$$

Only the second exponential term in Eq. 4.10 is proportional to the radial distance from the axis of the pulse. We can rewrite this term in the following form:

$$\exp\left[-i\frac{L}{L_{NL}}\frac{2r^2}{w_0^2}\exp\left[-\frac{(4\ln 2)T^2}{\tau_0^2}\right]\right] = \exp\left[-i\frac{k_0}{2f}r^2\right] , \tag{4.11}$$

where

$$f = \frac{k_0 w_0^2}{4}\frac{L_{NL}}{L}\exp\left[\frac{(4\ln 2)T^2}{\tau_0^2}\right] = \frac{1}{n_2 I_0 L}\frac{w_0^2}{4}\exp\left[\frac{(4\ln 2)T^2}{\tau_0^2}\right] . \tag{4.12}$$

We note that Eq. 4.11 is in the exact form of a phase imparted to a pulse that has passed through a lens, such that the focal length f of the lens is given by Eq. 4.12.

We may gain several important insights from the expression for the focal length given by Eq. 4.12 for the subsequent evolution of pulse that has passed through a thin nonlinear medium of length L. Firstly, we see that the focal length depends on the nonlinear refractive index n_2 : as the nonlinear refractive index increases, the focal length decreases. Secondly, the focal length depends inversely upon the peak intensity I_0 of the pulse. Thirdly, it depends inversely upon the length of the medium L. Fourthly the focal length is proportional to the square of the intensity beam waist w_0^2 : the smaller the beam waist, the smaller the focal length. Fifthly, we see that through the temporal profile of the pulse, different parts of the pulse have different effective focal lengths: The leading and trailing edges of the pulse have much greater focal lengths than the peak of the pulse at T=0, which has the smallest focal length and experiences the strongest self-focusing action. This phenomenon is known as *slice-by-slice self-focusing*, and it is important in the theory of femtosecond pulse filamentation [44]. Specifically, it leads to the formation of an *energy reservoir* that surrounds the filament and has a diameter on the order of a millimeter for pulses propagating in air. We will discuss this particular aspect of filaments more fully in later sections.

In the above greatly-simplified analysis, we have ignored effects due to beam divergence. This was justified because we considered only a thin nonlinear medium of length L. However, self-focusing due to femtosecond filamentation takes place within a bulk medium where the effects of beam divergence are not negligible and must be taken

into account. Indeed, beam defocusing due to divergence is a competing action whose force is opposite in sign to that of self-focusing, that is, divergence tends to work against self-focusing. As a result, if the self-focusing action is not strong enough to overcome divergence due to diffraction, the pulse never self-focuses. There is a point, however, where the pulse peak power is strong enough to exactly balance the forces due to diffraction; this is known as the critical power P_c , and it has the form [44,45]:

$$P_c = \frac{3.77\lambda_0^2}{8\pi n_2 n_0} \ . \tag{4.13}$$

Marburger [45] has numerically solved for the distance z_f at which a pulse with peak power P will self-focus while propagating within a bulk nonlinear medium, according Eq. 4.3. His analysis yielded the quantity

$$z_f = \frac{0.367\, k_0 \left(w_0 / \sqrt{2}\right)^2}{\sqrt{\left[\left(\frac{P}{P_c}\right)^2 - 0.852\right]^2 - 0.0219}} \ . \tag{4.14}$$

We see that Eq. 4.14 has many similarities to our simplified analysis according to Eq. 4.12, with the addition of dependencies upon the wavenumber k_0 and the critical power P_c at which self-focusing equals the defocusing forces due to beam divergence. Equation 4.14 remains accurate for many instances [44]. In practice, however, it is often convenient in experiment to supplement the self-focusing action of a pulse with a lens in order to induce pulse collapse within distances amenable to laboratory analysis. In this case, Eq. 4.14 is modified to be of the form [44]:

$$\frac{1}{z_f'} = \frac{1}{z_f} + \frac{1}{f} \ , \tag{4.15}$$

where z_f' is the new self-focusing distance, z_f is according to Eq. 4.14, and f is the focal length of the lens used.

The above discussion has furnished an intuitive and illustrative understanding of the phenomenon of self-focusing of intense pulses propagating in nonlinear media. Femtosecond filamentation is not only due to self-focusing, however; it is also due to intensity clamping, which is due to ionization of the medium. In the following sections, we will describe ionization and how it contributes to intensity clamping within the phenomenon of filamentation.

4.2 IONIZATION AND LIGHT PROPAGATION IN PLASMA

4.2.1 Mechanisms of ionization

The phenomenon of ionization is best understood within a quantum mechanical framework, in which electrons surrounding an atomic nucleus are found within potential wells. The process of ionization describes how electrons within the potential wells of atoms or molecules escape that bound state and become "free." Within the context of laser-induced ionization, there are three main ionization mechanisms that must be considered in any fair treatment of the subject: tunneling ionization, multi-photon ionization, and avalanche (or laser-induced collisional) ionization. In this subsection we

consider all three mechanisms, first touching upon tunneling and multi-photon ionization (since they are closely related phenomena) and then considering avalanche ionization.

The first to understand the relationship between tunneling and multi-photon ionization was Keldysh [48–50]. We begin by considering an electron within a potential well of depth Φ, with units of energy. We assume that there are no intervening atomic levels between the free ionized state and the bound state of depth Φ: in this manner we eliminate consideration of resonance effects with intervening levels. We also assume that incident upon the atom or molecule is an electric field with amplitude E, intensity $I = \frac{1}{2} c n_0 \varepsilon_0 |E|^2$, and frequency ω. We recall that an electric field distorts the shape of the potential well within which the electron is trapped, thus allowing the electron to tunnel through the potential barrier. The time it takes for an electron to tunnel through is determined by the mean free time of the electron passing through a barrier of width l:

$$l = \Phi / eE \ , \tag{4.16}$$

where e is the charge of the electron. The average electron velocity is of the order $\sqrt{\Phi / m_e}$, where m_e is the electron mass. We can then designate a tunneling frequency (which is the reciprocal of the tunneling time) ω_t:

$$\omega_t = \frac{eE}{\sqrt{2 m_e \Phi}} \ . \tag{4.17}$$

However, we recall that the field with amplitude E has a frequency ω. If the frequency of the field ω is much larger than the tunneling frequency ω_t, the electron will not have enough time to tunnel through the potential barrier within one cycle of the field.

Thus we designate an adiabaticit parameter γ, known as the *Keldysh parameter*, by which we can know the relative magnitude of the field frequency ω and the tunneling frequency ω_t and that is defined as

$$\gamma = \frac{\omega}{\omega_t} = \frac{\omega\sqrt{2m_e\Phi}}{eE} \quad . \tag{4.18}$$

Thus we see that if $\omega \ll \omega_t$, then $\gamma \ll 1$ and tunneling ionization will be the dominant ionization mechanism. However, if $\omega \gg \omega_t$, then $\gamma \gg 1$ and tunneling ionization is not likely to occur. In the latter instance, the dominant ionization mechanism is multi-photon ionization.

Multi-photon ionization is a nonlinear optical process by which an electron absorbs the energy of a number *K* of photons such that the energy gained is greater than the depth of the potential well Φ [49,50]:

$$K\hbar\omega > \Phi \quad . \tag{4.19}$$

As mentioned above, multi-photon ionization is the dominant ionization mechanism when $\gamma \gg 1$.

For an electromagnetic field of fixed frequency ω incident upon a collection of atoms or molecules with fixed ionization energy Φ, the parameter which determines the value of the Keldysh parameter is the magnitude of the electric field E, which itself is determined by the intensity *I* of the laser field. As the intensity of the laser field increases, the value of the Keldysh parameter decreases, such that for intensities great enough the dominant ionization mechanism may switch from multi-photon to tunneling. It is also evident from Eq. 4.18 that laser fields with low frequencies will approach the

limit $\gamma \ll 1$ much faster than fields with high frequencies as the field intensity is increased. Consequently, tunneling ionization is easier to achieve with infrared frequencies than it is with optical frequencies for laser fields of equal intensities.

Keldysh [48] showed that in limiting cases, when $\gamma \ll 1$ and $\gamma \gg 1$, the ionization probability rate W of each ionization mechanism is different. The ionization probability rate describes how the free electron density per unit volume ρ_e changes with time:

$$\frac{d\rho_e}{dt} = W_{TOT} \ , \tag{4.20}$$

where W_{TOT} describes the total contributions to the change in electron density. Figure 4.1 shows the ionization probability rate for liquid water as a function of laser intensity for a wavelength of $\lambda = 800\ nm$. In this simulation, the liquid water has been treated as an amorphous semiconductor as in [51] with a bandgap of $\Delta = 6.5\ eV$ between the valence and conduction band. In condensed matter, the Keldysh parameter takes the following form [48]:

$$\gamma = \frac{\omega\sqrt{2m\Delta}}{eE} \ , \tag{4.21}$$

where we use the reduced mass

$$\frac{1}{m} = \frac{1}{m_e} + \frac{1}{m_h} \ . \tag{4.22}$$

In Eq. 4.22, m_e is the mass of the electron and m_h is the mass of the hole. We here follow the treatment of [51] and let $m = m_e / 2$ for liquid water. Keldysh [48] showed that in condensed media the tunneling ionization probability rate W_T is given by

$$W_T = \frac{2}{9\pi^2}\frac{\Delta}{\hbar}\left(\frac{m\Delta}{\hbar^2}\right)^{3/2}\left(\frac{e\hbar E}{m^{1/2}\Delta^{3/2}}\right)^{1/2} \times \exp\left[-\frac{\pi}{2}\frac{m^{1/2}\Delta^{3/2}}{e\hbar E}\left(1-\frac{1}{8}\frac{m\omega^2\Delta}{e^2E^2}\right)\right], \tag{4.23}$$

for $\gamma \ll 1$. Likewise, he showed that the multi-photon ionization probability rate W_{MP} is given by

$$W_{MP} = \frac{2}{9\pi}\omega\left(\frac{m\omega}{\hbar}\right)^{3/2}\varphi\left[\left(2\left\langle\frac{\tilde{\Delta}}{\hbar\omega}+1\right\rangle-\frac{2\tilde{\Delta}}{\hbar\omega}\right)^{1/2}\right] \times \exp\left[2\left\langle\frac{\tilde{\Delta}}{\hbar\omega}+1\right\rangle\left(1-\frac{e^2E^2}{4m\omega^2\Delta}\right)\right]\left(\frac{e^2E^2}{16m\omega^2\Delta}\right)^{\left\langle\tilde{\Delta}/\hbar\omega+1\right\rangle}, \tag{4.24}$$

where

$$\tilde{\Delta} = \Delta + \frac{e^2E^2}{4m\omega^2} \tag{4.25}$$

$$\varphi(x) = \int_0^x \exp\left[-\left(x^2-y^2\right)\right]dy\ , \tag{4.26}$$

and $\langle ... \rangle$ denotes the integer part of the quantity inside the brackets. Equation 4.26 is known as the Dawson function [52] and can be found as Eq. 7.1.16 in [53]. Equation 4.25 shows how the ionization potential can be affected by a process known as the AC Stark effect, which in general results in an increase in the energy difference of levels that are separated by large potentials [50].

As stated above, Fig. 4.1 shows Eqs. 4.23 (green curve) and 4.24 (blue curve) as a function of intensity $I = \frac{1}{2} c n_0 \varepsilon_0 |E|^2$ in water, with $\Delta = 6.5\ eV$, $\lambda = 800\ nm$, and $n_0 = 1.325874$ at 800 nm [22].

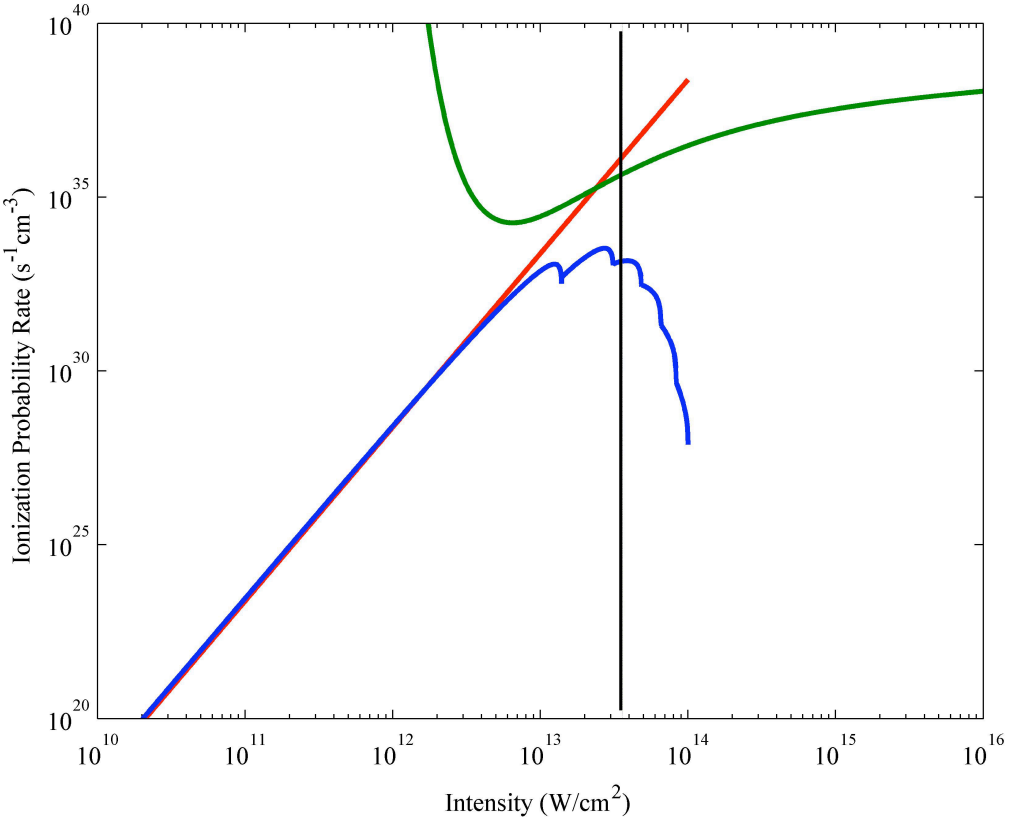

Fig. 4.1 Ionization probability rate for water for tunneling ionization in the limit that $\gamma \ll 1$ (green curve, Eq. 4.23), multi-photon ionization in the limit that $\gamma \gg 1$ (blue curve, Eq. 4.24), and the asymptotic limit for multi-photon ionization according to Eq. 4.27 (red curve). The black line shows the intensity at which $\gamma = 1$. Below this intensity, the blue and red curves are valid, while above this intensity, the green curve is valid.

Also shown in Fig. 4.1 is an asymptotic curve (red curve) for multi-photon ionization at low intensities of the form

$$W_{MP} = \sigma_5 I^5 \rho_{be} \ , \tag{4.27}$$

where the density of bound electrons ρ_{be} for water is $6.22 \times 10^{22}\ cm^{-3}$ [51] and σ_5 is found from a best fit of Eq. 4.2.1.9 to be $\sigma_5 = 3.55894 \times 10^{-55}\ cm^{10} / sW^5$. The factor I^5 in Eq. 4.27 reflects the fact that it takes five photons of wavelength 800 nm to overcome the ionization energy $\Delta = 6.5\ eV$.

Figure 4.1 shows that at low intensities, the multi-photon ionization mechanism dominates in water and therefore the ionization probability rate is best described by Eq. 4.24 (shown as the blue curve in Fig. 4.1) and its approximation Eq. 4.27, shown as the red curve. Also, it should be noted that at intensities below that indicated by the black line (at which point $\gamma = 1$), the green curve that shows Eq. 4.23 is not accurate. However, at intensities higher than that indicated by the black line (again, at which point $\gamma = 1$), tunneling ionization can no longer be considered negligible, and the ionization mechanism is dominated by tunneling. Hence, beginning around 4×10^{13} W/cm^2 intensity, the ionization probability rate is best described by Eq. 4.23, shown as the green curve in Fig. 4.1.

The values in Fig. 4.1 agree with and are similar to those in [51], with the difference that in our analysis we have used a wavelength of radiation of 800 nm, while in [51] a wavelength of 527 nm was considered.

Another very important ionization mechanism is avalanche ionization, which is a laser-induced collisional ionization. Avalanche ionization occurs after tunneling or multi-photon ionization has produced an initial non-zero density of free electrons. The free electrons in the strong laser field absorb photons through collision with heavier particles in the immediate environment (for example, atoms, molecules, or ions). The process by which a free electron absorbs a photon from the laser field through collision with a heavier particle is known as inverse Bremsstrahlung [54]. After several inverse Bremsstrahlung processes, the free electron acquires sufficient energy to ionize the particle with which it collides, resulting in two low-energy free electrons. Each electron then undergoes the same process, each producing an additional electron. The process begins with a single free electron, resulting in two free electrons, which again result in four, then eight, then sixteen free electrons. The population of free electrons then grows exponentially with time. This process is known as avalanche or cascade ionization.

Theoretically, the rate of change of the free electron population ρ_e due to the process of avalanche ionization can be described as [55]:

$$\frac{d\rho_e}{dt} = \eta(E)\rho_e \ , \tag{4.28}$$

where $\eta(E)$ is the probability per unit time for an electron to undergo an ionizing collision and is, in general, a function of the amplitude E of the electric field. For aqueous media, Kennedy [56] has shown that $\eta \propto I$, the intensity of the electric field.

Within the process of femtosecond filamentation, the intensities are often too low for tunneling ionization to be important. Therefore, the dominant ionization mechanisms

are multi-photon ionization quickly followed by avalanche ionization. The first free electrons are generated through multi-photon ionization, and the free electron population is quickly increased through avalanche processes. Yablonovitch and Bloembergen have shown that the diameter of filaments is limited by the process of avalanche ionization [57].

For filaments, therefore, it is often sufficient to describe the time evolution of the free electron population ρ_e in condensed media as [58]:

$$\frac{d\rho_e}{dt} = \sigma_K I^K \left(\rho_{be} - \rho_e\right) + \alpha \rho_e I \ , \tag{4.29}$$

where K is the number of photons needed to exceed the ionization potential Δ, ρ_{be} is the bound electron density, and α is an avalanche coefficient. The first term on the right hand side of Eq. 4.29 describes multi-photon ionization according to the asymptotic law described in Eq. 4.27, while the second term describes avalanche ionization according to the dependence on intensity described by Kennedy [56]. In general, Eq. 4.29 ought to include a term describing the recombination of electrons and ions [59,60]. However, in terms of the evolution of the femtosecond pulse itself, this term can often be neglected as the recombination time is often orders of magnitude longer than the pulse duration itself.

We have given a brief overview of the main mechanisms involved in laser-induced ionization. In the following subsection, we will consider how the susceptibility of a medium is affected by the presence of free electrons and ions.

4.2.2 Lorentz-Drude model of susceptibility of plasmas

A simple model of how light interacts with free electrons and ions (a plasma) was developed by Drude [61]. In this analysis, we assume that the plasma is located in a region with no external electric or magnetic fields except that of the incident light radiation. We also assume that ions are essentially fixed and that only the movement of electrons is significant. This assumption is justified by the fact that the electron mass is several orders of magnitude less than that of ions. This type of plasma is known as a Lorentz plasma [62]. Hence, this plasma model is now known as the Lorentz-Drude model [63]. It begins by considering Maxwell's Equations in the macroscopic limit for a homogeneous isotropic medium of dielectric constant ε, magnetic permeability $\mu = 1$, and nonzero conductivity σ. The conductivity is defined such that

$$\vec{J} = \sigma \vec{E} \ , \tag{4.30}$$

where $\vec{J}$ is the current density. This analysis differs from that in Section 2.2 in that the conductivity is nonzero.

We also assume that the interaction between electromagnetic radiation and the plasma is linear, so that we can write

$$\vec{D} = \tilde{\varepsilon} \vec{E} \tag{4.31}$$

$$\vec{B} = \tilde{\mu} \vec{H} \ , \tag{4.32}$$

where

$$\tilde{\varepsilon} = \varepsilon_0 \left(1 + \tilde{\chi}_e\right) \tag{4.33}$$

$$\tilde{\mu} = \mu_0 \left(1 + \tilde{\chi}_m\right) \ . \tag{4.34}$$

Here, $\tilde{\chi}_e$ is the complex linear electric susceptibility and $\tilde{\chi}_m$ is the complex linear magnetic susceptibility. We can then write the macroscopic Maxwell's Equations as

$$\nabla \cdot \vec{D} = \rho \tag{4.35}$$

$$\nabla \cdot \vec{B} = 0 \tag{4.36}$$

$$\nabla \times \vec{E} = -\frac{\partial \vec{B}}{\partial t} \tag{4.37}$$

$$\nabla \times \vec{H} = \vec{J} + \frac{\partial \vec{D}}{\partial t} \ . \tag{4.38}$$

Since in a plasma there are both positive and negative charges, the overall charge density ρ in Eq. 4.35 can be taken as zero. In reality, the charge density is nonzero for a fraction of a second and decays exponentially in a time of the order of 10^{-18} s for many metals [61]. However, this decay time, known as the *relaxation time*, is typically much shorter than the periodic time of vibration of the incident light wave. Hence, we may take $\rho = 0$.

In a manner analogous to that in Section 2.2, in which we take the curl of Eq. 4.37 and substitute the time derivative of Eq. 4.38, we arrive at the following wave equation:

$$\nabla\left(\nabla \cdot \vec{E}\right) - \nabla^2 \vec{E} = -\tilde{\mu}\left[\frac{\partial \vec{J}}{\partial t} + \frac{\partial^2 \vec{D}}{\partial t^2}\right], \tag{4.39}$$

where we have used the definition of the magnetic flux density in Eq. 4.32. Making use of the fact that we have taken the charge density $\rho = 0$ along with the definition of the

current density in Eq. 4.30 and the electric flux density in Eq. 4.31, we can rewrite the wave equation as

$$\nabla^2 \vec{E} = \tilde{\mu}\left[\sigma \frac{\partial \vec{E}}{\partial t} + \tilde{\varepsilon}\frac{\partial^2 \vec{E}}{\partial t^2}\right] . \tag{4.40}$$

We now consider the case where the electric field propagates in the z direction and is linearly polarized in the x or y directions. We assume that the solution of the wave equation is of the form

$$\vec{E}(z,t) = \vec{E}_0 \exp\left[i\left(\tilde{k}z - \omega t\right)\right] + c.c. , \tag{4.41}$$

in which case we may write Eq. 4.40 as

$$\tilde{k}^2 = \frac{\omega^2 \tilde{\mu}_r}{c^2}\left(\tilde{\varepsilon}_r + i\frac{\sigma}{\varepsilon_0 \omega}\right) . \tag{4.42}$$

Since we assume $\tilde{\mu}_r = 1$ and we recognize that Eq. 4.42 is of the same form as Eq. 2.41, we can write the complex refractive index $\tilde{n}$ of the plasma as

$$\tilde{n}^2 = \tilde{\varepsilon}_r + i\frac{\sigma}{\varepsilon_0 \omega} . \tag{4.43}$$

Utilizing the relationship between the susceptibility, dielectric constant, and refractive index as outlined in Eqs. 2.25-2.28, we can write

$$\tilde{\chi}_{tot}(\omega) = \tilde{\chi}_e(\omega) + i\frac{\sigma}{\varepsilon_0 \omega} , \tag{4.44}$$

where $\tilde{\chi}_e$ is the electric susceptibility of the medium in the absence of plasma (as a function of frequency) and $\tilde{\chi}_{tot}$ is the susceptibility of the medium and plasma together (also as a function of frequency).

It remains for us to find an expression for the conductivity σ in measurable quantities. We consider, as mentioned above, only the motions of the electrons and take the position of the ions to be fixed. The current density $\vec{J}$ may be written as

$$\vec{J} = n_e e \upsilon_e \ , \tag{4.45}$$

where n_e is the number density of electrons per unit volume, e is the charge of the electron, and υ_e is the average velocity of the electrons. The forces acting on the electrons are of the form

$$m_e \frac{\partial \upsilon_e}{\partial t} = e\vec{E} - \nu m_e \upsilon_e \ , \tag{4.46}$$

where m_e is the mass of the electron and ν is a collision frequency that takes account of any damping [61]. We note that in certain circumstances it may be appropriate to replace the electron mass m_e with a reduced mass. In general, the collision frequency ν is a function of the velocity of the electrons and hence of the frequency of the electric field [62,64]. However, in most cases this velocity dependence is negligible and we can regard the collision frequency ν as independent of frequency. The solution to Eq. 4.46 is then

$$\vec{J} = \frac{n_e e^2}{m_e(\nu - i\omega)} \vec{E} \ . \tag{4.47}$$

Comparing Eq. 4.47 to Eq. 4.30, we see that the conductivity is given as

$$\sigma = \frac{n_e e^2}{m_e(\nu - i\omega)} = \frac{n_e e^2}{m_e} \frac{(\nu + i\omega)}{(\nu^2 + \omega^2)} \ . \tag{4.48}$$

With this expression for the conductivity, we can rewrite Eq. 4.44 for the susceptibility as

$$\tilde{\chi}_{tot}(\omega) = \tilde{\chi}_e(\omega) - \frac{\omega_p^2}{\nu^2 + \omega^2} + i\frac{\omega_p^2}{\omega}\frac{\nu}{\left(\nu^2 + \omega^2\right)} \ , \tag{4.49}$$

where we have introduced the *plasma frequency* ω_p as

$$\omega_p^2 = \frac{n_e e^2}{\varepsilon_0 m_e} \ . \tag{4.50}$$

In general, we may write

$$\tilde{\chi}_e(\omega) = \chi'(\omega) + i\chi''(\omega) \ , \tag{4.51}$$

where χ' and χ'' are real, similar to Eq. 2.31. We may then write the total electric susceptibility as

$$\tilde{\chi}_{tot}(\omega) = \chi'(\omega) - \frac{\omega_p^2}{\nu^2 + \omega^2} + i\left(\chi''(\omega) + \frac{\omega_p^2}{\omega}\frac{\nu}{\left(\nu^2 + \omega^2\right)}\right). \tag{4.52}$$

4.2.3 Refractive index of plasmas

In the preceding subsection we solved for the susceptibility of a medium with free electrons and ions. In this subsection, we solve for the refractive index. We begin with the expressions relating the complex susceptibility $\tilde{\chi} = \chi' + i\chi''$ to the complex refractive index $\tilde{n} = n + i\kappa$ shown in Eqs. 2.37 and 2.38. Substituting Eq. 4.52 into these equations yields

$$n = \left[\frac{\sqrt{\left(1+\chi'(\omega)-\frac{\omega_p^2}{\nu^2+\omega^2}\right)^2+\left(\chi''(\omega)+\frac{\omega_p^2}{\omega}\frac{\nu}{\left(\nu^2+\omega^2\right)}\right)^2}+\left(1+\chi'(\omega)-\frac{\omega_p^2}{\nu^2+\omega^2}\right)}{2} \right]^{1/2}$$

(4.53)

$$\kappa = \left[\frac{\sqrt{\left(1+\chi'(\omega)-\frac{\omega_p^2}{\nu^2+\omega^2}\right)^2+\left(\chi''(\omega)+\frac{\omega_p^2}{\omega}\frac{\nu}{\left(\nu^2+\omega^2\right)}\right)^2}-\left(1+\chi'(\omega)-\frac{\omega_p^2}{\nu^2+\omega^2}\right)}{2} \right]^{1/2}.$$

(4.54)

We see, then, that for $\nu \ll \omega$ and $\omega \gg \omega_p$, a plasma tends to decrease the real part of the refractive index and increase the imaginary part of the refractive index.

Shown in Fig. 4.2 is the real part of the refractive index (blue curve) of a plasma in vacuum with incident radiation of wavelength $\lambda = 800$ *nm* as a function of electron density. The collision frequency ν is taken to be zero. Also plotted is the electron density n_p (red curve) at which the plasma frequency ω_p equals the frequency of the incident radiation. One can see that the real part of the refractive index goes to zero as the electron density nears n_p, so that at electron densities above n_p, the incident radiation is completely reflected from the boundary of the plasma.

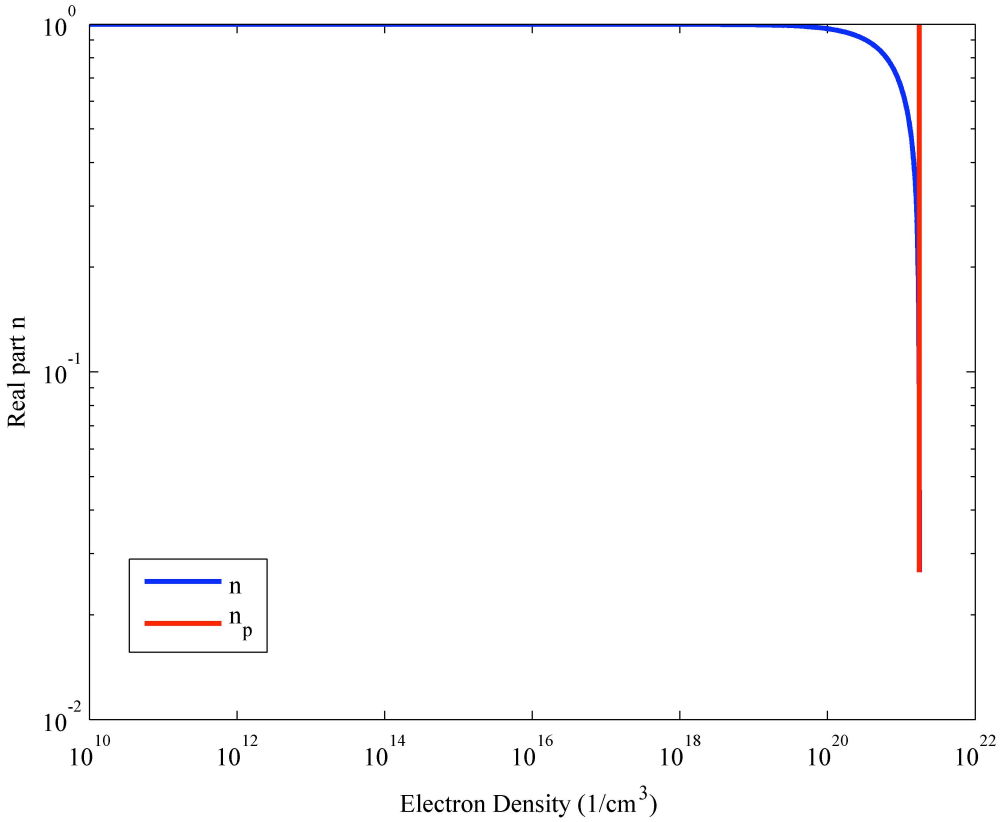

Fig. 4.2 Real part of the refractive index n (blue curve) for a plasma in vacuum with a collision rate $\nu = 0$. Also shown is the electron density n_p at which the plasma frequency equals the frequency of the incident radiation (red curve).

Shown in Fig. 4.3 are the real (blue curve) and imaginary (green curve) parts of the refractive index for a plasma in liquid water for incident radiation with a wavelength of $\lambda = 800\ nm$ as a function of electron density. The collision frequency is taken to be $\nu = 0.625\ fs^{-1}$ according to [63]. Also shown is the electron density n_p at which the plasma frequency ω_p equals the frequency of the incident radiation.

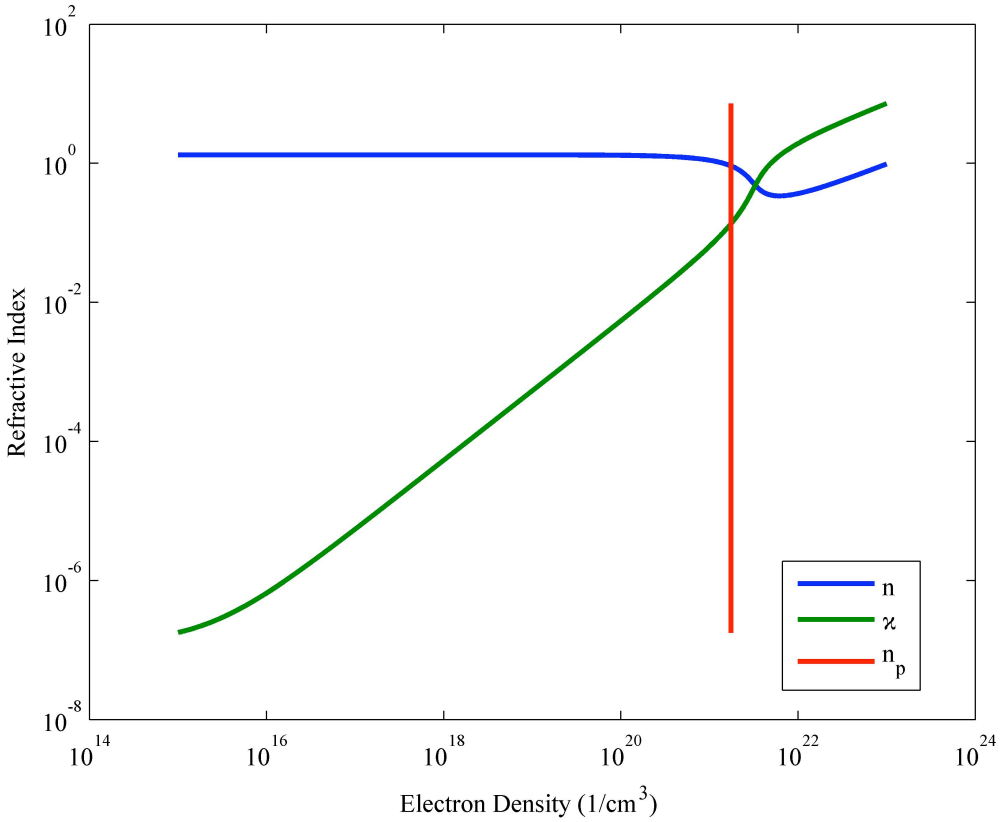

Fig. 4.3 Real part of the refractive index n (blue curve) and imaginary part of the refractive index κ (green curve) for a plasma in liquid water with a collision rate $\nu = 0.625\ fs^{-1}$. Also shown is the electron density n_p at which the plasma frequency equals the frequency of the incident radiation (red curve).

One can see from Fig. 4.3 that for a plasma in liquid water with incident radiation of $\lambda = 800\ nm$, the real part of the refractive index does not go to zero. This is a consequence of the high collision frequency ν, which is a significant fraction of the frequency of the incident radiation. However, the imaginary part of the refractive index sees a significant increase as the electron density increases.

In the preceding three subsections we have investigated the mechanisms of

ionization and how light propagates through a medium in which free electrons and ions are present. In the following section we will consider how these mechanisms contribute to the phenomenon of femtosecond laser pulse filamentation in combination with the phenomenon of self-focusing.

4.3 THE PROCESS OF FEMTOSECOND LASER PULSE FILAMENTATION

Femtosecond laser pulse filamentation at the most basic level is a result of the phenomena described in the preceding two sections: self-focusing and ionization. In Section 4.1 it was shown that an intense laser pulse with a radially-dependent intensity distribution (decreasing intensity with increasing distance from the pulse propagation axis) experiences a nonlinear phase shift due to the nonlinear refractive index n_2 such that the pulse experiences slice-by-slice self-focusing, with the most intense parts of the pulse focusing faster than less intense parts. This results in the formation of a filament energy reservoir. At the center of the filament is a core of high intensity surrounded by a region of more loosely focused radiation. It has been claimed that the vast majority of the pulse energy in a filament is found within the energy reservoir [44]. Also, blocking the energy reservoir with an iris while allowing the intense filament core to pass effectively kills the filament; this is because the energy reservoir contains those elements of the pulse that are more loosely focused but nevertheless are focused into the intense filament core at greater propagation distances.

As the pulse self-focuses, the intensity of the pulse increases, resulting in multi-photon and, subsequently, avalanche ionization of the atoms and/or molecules of the

propagation medium. In Section 4.2 it was shown that free electrons and ions (plasma) within a medium result in a refractive index that is less than that of the surrounding medium. The greater the electron density, in general, the less the refractive index (as shown in Fig. 4.3, this is not always the case; however, for intensities at which filamentation takes place, the described relationship holds to be mostly true). Plasma, then, tends to impart a phase shift onto the femtosecond pulse that is opposite in sign to that of nonlinear self-focusing. Hence, while the nonlinear refractive index n_2 results in self-focusing, the free electrons and plasma generated by the pulse at high intensities tend to defocus the pulse. The interplay between self-focusing and the intensity-dependent phenomenon of ionization (with greater intensities corresponding to greater ionization rates and, therefore, greater electrons densities) results in a phenomenon called *intensity clamping* [44]. Intensity clamping occurs when the forces on a femtosecond laser pulse due to self-focusing and defocusing due to plasma balance; when this happens, the diameter of the pulse remains relatively constant as it propagates. This type of self-guided propagation is a nonlinear phenomenon and is an integral part of the minimal definition of a femtosecond laser pulse filament given at the beginning of this chapter. As mentioned in Subsection 4.2.1, the diameter of filaments that experience intensity clamping is generally determined by the avalanche ionization threshold of the propagation medium [57].

It is worth mentioning here that in recent years, several works have claimed that higher-order Kerr terms such as n_4, n_6, n_8, etc. are the dominant defocusing mechanisms instead of free electrons generated by ionization [65,66]. However, it was

subsequently shown that, while higher-order Kerr terms may indeed exist, the process of defocusing due to ionization effectively limits the pulse intensity such that they do not play a dominant or significant role in pulse filamentation [67]. We can thus say with confidence that the filament diameter is limited by the various ionization thresholds of the medium.

A simple model of laser pulse filamentation in gases is given by Eq. 3.6 in [44]:

$$i\frac{\partial A}{\partial z}+\frac{1}{2k}\nabla_{\perp}^{2}A+n_{2}k_{0}\left|A\right|^{2}A-\frac{2\pi e^{2}N_{e}}{km_{e}c^{2}}A+i\Gamma A=0\ , \tag{4.55}$$

where the intensity I of the pulse is defined as $I=\left|A\right|^{2}$ in units of W/cm^2. The terms N_e and Γ in Eq. 4.55 are the electron density per unit volume and pulse energy losses due to ionization, respectively. Equation 4.55 is coupled with an equation detailing the temporal evolution of the electron density:

$$\frac{\partial N_{e}}{\partial t}=\left(N_{0}-N_{e}\right)R(I)\ , \tag{4.56}$$

where N_0 is the number density per unit volume of neutral atoms and/or molecules and $R(I)$ is the ionization rate as a function of pulse intensity. In combination, Eqs. 4.55 and 4.56 account for self-focusing and intensity clamping due to ionization. They explain the "filament" of free electrons and plasma that is left behind an intensity-clamped laser pulse filament. They also account for pulse energy loss due to the process of ionization. It should be mentioned that in solids and liquids, Eq. 4.55 ought to contain a term accounting for the linear dispersion of the pulse, which also serves as a defocusing mechanism. Regardless, however, the slowly-varying pulse envelope approximation

used in these equations can break down in certain circumstances. It is important to note that the temporal evolution of the pulse within the filament core is highly dynamic. Pulse splitting and x-wave generation have been theoretically and experimentally observed [44].

According to the minimal definition of a femtosecond laser pulse filament given at the beginning of this chapter, we have focused mainly upon the processes of self-focusing and ionization which result in intensity clamping and self-guided pulse propagation. While this dissertation is not sufficient to deal fairly with the many other interesting and important nonlinear phenomena associated with femtosecond laser filaments, we think that several of them bear mentioning. One of the most striking features of femtosecond laser pulse filaments is the phenomenon of conical emission, resulting in a rainbow of colors arranged in a type of bull's-eye pattern seen in the forward propagation direction. Conical emission has been described as self-phase modulation in the radial direction [44]. There is now a large body of literature investigating this phenomenon. Another important feature of femtosecond laser filaments is self-spatial filtering. As the pulse self-focuses, high-order beam modes are filtered out, resulting in a fundamental beam mode within the filament core. Other important phenomena connected with laser pulse filaments are self-pulse compression and self-group-phase locking of other pulses inside the filament. These phenomena have become important in the generation of few-cycle laser pulses.

While a laser filament eventually defocuses, it is possible that it can refocus, thus resulting in several or even many cycles of focusing and defocusing. In this manner, a

laser pulse of high energy may propagated over long distances in a highly-focused beam configuration. Multiple filamentation is also an important phenomenon. This occurs when a laser pulse contains sufficient energy and is of high enough intensity to form more than one filament. Perturbations within the intensity profile of a pulse and the action of self-spatial filtering combined with intensity clamping are mechanisms behind this important phenomenon. Multiple filamentation may find potential applications in many remote sensing setups. Another important phenomenon associated with femtosecond laser pulse filamentation that may find applications in remote sensing is molecular orientation and periodic revival [44].

In this section we have described how the main mechanisms behind laser pulse filamentation come together. We have also mentioned several other important phenomena associated with femtosecond laser filaments. We stress that this basic description is sufficient only to gain an intuitive understand of the main mechanisms behind filamentation. The body of literature describing the many important and interesting aspects of laser pulse filamentation is rapidly increasing. In the next section, we describe an experiment detailing how crossed filaments propagating within liquid methanol may exchange energy.

4.4 ENERGY TRANSFER BETWEEN LASER FILAMENTS IN LIQUID METHANOL

4.4.1 Theoretical background: two-beam coupling

Two-beam coupling is a nonlinear phenomenon in which energy from one beam is transferred into another intersecting beam of different frequency [18]. In this subsection we outline the basic theory in order that the subsequently-described experiment dealing with energy transfer between laser filaments in liquid methanol may be properly understood.

We begin by describing two light beams of wavenumbers $\vec{k}_1$ and $\vec{k}_2$ by a total electromagnetic field

$$E(\vec{r},t) = A_1 \exp\left[i\left(\vec{k}_1 \cdot \vec{r} - \omega_1 t\right)\right] + A_2 \exp\left[i\left(\vec{k}_2 \cdot \vec{r} - \omega_2 t\right)\right] + c.c. \tag{4.57}$$

where the intensity of the pulse I is $I = n_0 \varepsilon_0 c \left\langle E^2 \right\rangle$, where the brackets denote a time average over many optical cycles. The intensity of the electric field given by Eq. 4.57 is then

$$I = 2 n_0 \varepsilon_0 c \left\{ A_1 A_1^* + A_2 A_2^* + \left[A_1 A_2^* \exp\left[i\left(\vec{q} \cdot \vec{r} - \Omega t\right)\right] + c.c.\right]\right\} , \tag{4.58}$$

where we have introduced the quantities

$$\vec{q} = \vec{k}_1 - \vec{k}_2 \tag{4.59}$$

$$\Omega = \omega_1 - \omega_2 \ . \tag{4.60}$$

Energy transfer is possible only when there is finite nonlinear response time τ. The nonlinear response time is related to the imaginary component of the nonlinear refractive index n_{NL} [18]. We here assume that the nonlinear part of the refractive index obeys a relaxation equation of the form

$$\tau \frac{dn_{NL}}{dt} + n_{NL} = n_2 I \ . \tag{4.61}$$

The solution of Eq. 4.61 is

$$n_{NL} = \frac{n_2}{\tau} \int_{-\infty}^{t} I(t') \exp\left[\frac{t'-t}{\tau} \right] dt' \ . \tag{4.62}$$

Substituting Eq. 4.58 into the expression for the intensity of the electric field in Eq. 4.62 yields the equation for the nonlinear refractive index:

$$n_{NL} = 2n_0 n_2 \varepsilon_0 c \left[\left(A_1 A_1^* + A_2 A_2^* \right) + \frac{A_1 A_2^* \exp\left[i\left(\vec{q} \cdot \vec{r} - \Omega t \right) \right]}{1 - i\Omega\tau} + \frac{A_1^* A_2 \exp\left[-i\left(\vec{q} \cdot \vec{r} - \Omega t \right) \right]}{1 + i\Omega\tau} \right] . \tag{4.63}$$

It is necessary that the electric field given in Eq. 4.57 satisfy the wave equation

$$\nabla^2 E - \frac{n^2}{c^2} \frac{\partial^2 E}{\partial t^2} = 0 \ , \tag{4.64}$$

where we define the refractive index as

$$n = n_0 + n_{NL} \ . \tag{4.65}$$

Using the reasonable assumption that $\left| n_{NL} \right| \ll n_0$, we may approximate the square of the refractive index as

$$n^2 = n_0^2 + 2n_0 n_{NL} \ . \tag{4.66}$$

In order to show the energy coupling between the two beams, we substitute the total electric field given in Eq. 4.57 into the wave equation of Eq. 4.64 and consider only terms that have a spatial and temporal dependence given by

$$\exp\left[i\left(\vec{k}_2 \cdot \vec{r} - \omega_2 t\right)\right] \ . \tag{4.67}$$

We make the slowly varying envelope approximation, which allows us to disregard second order derivatives in the spatial domain as negligible. We then find that

$$\frac{dA_2}{dz} = 2in_0 n_2 \frac{\omega}{c}\left[\left(\left|A_1\right|^2 + \left|A_2\right|^2\right)A_2 + \frac{\left|A_1\right|^2 A_2}{1 + i\Omega\tau}\right] , \tag{4.68}$$

where we have to good approximation replaced ω_1 and ω_2 by ω. We now define the intensities

$$I_1 = 2n_0 \varepsilon_0 c A_1 A_1^* \tag{4.69}$$

$$I_2 = 2n_0 \varepsilon_0 c A_2 A_2^* \ . \tag{4.70}$$

Utilizing Eq. 4.68, we find that

$$\frac{dI_2}{dz} = \frac{2n_2\omega}{c}\frac{\Omega\tau}{1+\Omega^2\tau^2} I_1 I_2 \ . \tag{4.71}$$

We see from Eq. 4.71 that the intensity and, therefore, the energy contained within the beam with wavenumber $\vec{k}_2$ changes with propagation distance z and depends both on I_1 and I_2. It is also important to note that should either $\Omega = \omega_1 - \omega_2$ or τ be equal to zero, there is no energy transfer, and the beams are not coupled.

Figure 4.4 shows the general shape of the dependence of Eq. 4.71 on the quantity $\Omega\tau$. This shape is characteristic of beam coupling. For ultrashort laser pulses, the interaction of two beams with frequencies ω_1 and ω_2 may be accomplished by crossing two chirped laser pulses with different time delays. Chirping may be accomplished either through a pulse compressor or through propagation through a dispersive medium. Using such techniques as these, it is possible to reproduce the shape of Fig. 4.4 using crossed, chirped laser pulses [68,69].

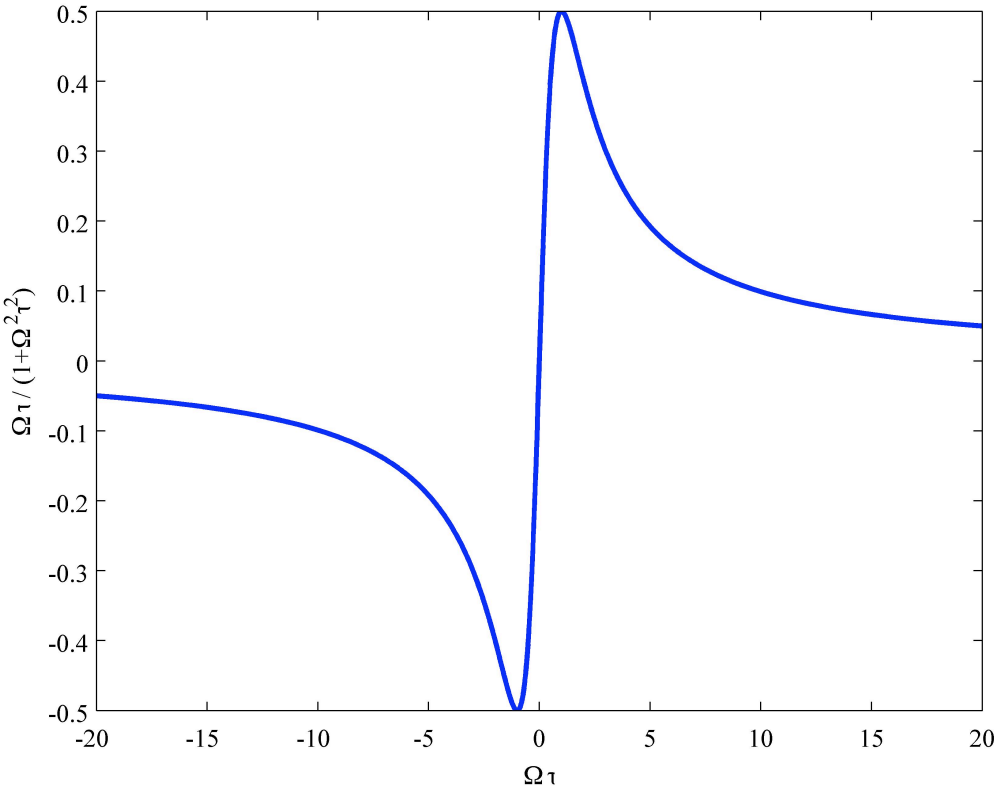

Fig. 4.4 Characteristic shape of the dependence of beam coupling on the quantity $\Omega\tau$ as shown in Eq. 4.71.

4.4.2 Energy transfer as a possible method to control femtosecond laser filaments

Femtosecond filamentation occurs when laser beam power reaches a critical value defined by intrinsic properties of the propagating medium; it is a result of the dynamic balance between Kerr self-focusing and defocusing due to low-density plasma [70]. The control of propagating optical filaments has several important applications associated with sophisticated techniques for remote sensing [5,70]. Propagation control methods include prechirping the femtosecond laser pulse [71,72], variable focusing [73,74], and adaptive optics scenarios [75]. Another potential method of controlling the direction or energy content of a propagating filament is energy coupling between two crossed filament-forming femtosecond laser beams. Energy transfer from one filament to another has recently been demonstrated in a number of experiments involving optical filaments in air [68,69]. It has been shown that the direction of energy flow depends on the relative laser pulse delay. In this experiment, we study filament-coupling behavior in transparent liquid bulk media, keeping in mind potential applications to underwater or atmospheric sensing. We observe a coarse timescale dependence, similar to that described in [68,69], when the pulse delay between the two filament-forming beams is varied over approximately 100 fs. In addition, we find a previously undocumented fine time-scale oscillation in the two-beam energy exchange, which is governed by the relative phase of the filament-forming pulses and has a time-delay period equal to that of the incident radiation (2.6 fs).

4.4.3 Experimental setup for crossed filaments

An experimental schematic is shown in Fig. 4.5. We use a Ti:sapphire-based laser system consisting of an oscillator (Mira, Coherent) and an amplifier (Legend, Coherent: 800 nm center wavelength, 35 fs pulse duration, 1 kHz repetition rate, 1 mJ pulse energy). The beam power is controlled by passing through several neutral density filters; the beam is then incident on identical pinholes of 1 mm diameter; we note that diffraction effects from the pinholes may play a role in subsequent filament formation and propagation. One of the two resultant beams is picked off by a D-shaped mirror and directed toward a focusing lens with a 5 cm focal length. The remaining beam is passed

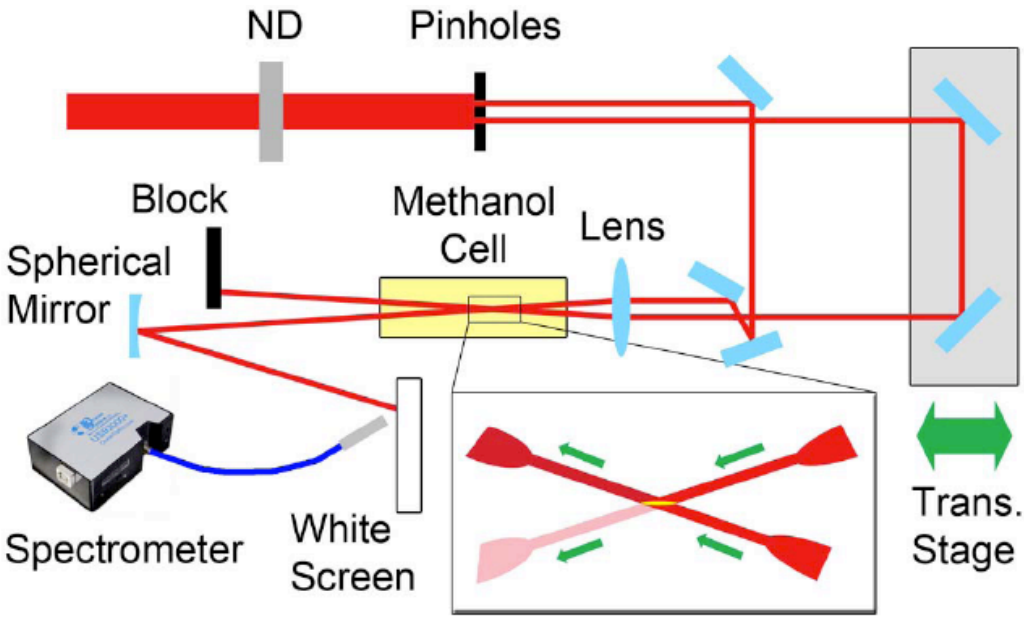

Fig. 4.5. Experimental schematic. ND= neutral density filter. The inset shows the intersection of two filaments involved in energy transfer [10].

through a motorized translation-stage setup (GTS150, ESP301, Newport) and directed parallel to the fixed-path beam. The lateral distance between the two sub-beams may be controlled by adjusting the alignment of the fixed-path mirrors; hence, the angle between the interacting beams may also be varied. The interaction region of the two beams is located within the methanol cell (Fig. 4.5, inset), which is constructed of BK7 glass. The output is then focused by a spherical mirror, projected onto a white screen, and measured with a spectrometer (USB2000, Ocean Optics). Each beam is measured consecutively. We vary the temporal delay between the two pulses by changing the position of the translation stage; the minimal step corresponds to a temporal resolution of 0.33 fs.

In order to make a connection with previous work, we integrate the measured spectra to obtain the total power in each of the output beams. We then calculate the fraction of energy transfer:

$$S = \left(P_{fixed} - P_{trans}\right) / \left(P_{fixed} + P_{trans}\right), \tag{4.72}$$

where P_{fixed} and P_{trans} are the power in the fixed-path and translation-stage beams, respectively.

4.4.4 Energy transfer on two scales

Figure 4.6(a) shows *S* as a function of the relative delay between the pulses in each beam. For this dataset, the angle between the beams within the methanol sample was 3°, while the group delay dispersion (GDD) at the interaction point was about 7000 fs^2 (positive chirp, with lower frequency components leading the higher ones). The

propagation distance within the cell before interaction was 3.5 cm. Formation of single filaments was confirmed for these pulse energy levels upon inspection by adding a fluorescent dye to the methanol sample. The dye was not used for further measurements, which were conducted in pure methanol; formation of single filaments was also verified in the absence of dye by imaging the light exiting the cell with a lens. Filament diameters were measured with knife-edge and fluorescent imaging techniques to be less than 20 μm [76].

In Fig. 4.6(a), the negative delay corresponds to the translation-stage beam delayed with respect to the fixed-path beam. Notice that at lower input energies, such as 1.20 μJ, the energy transfer goes from high- to low-frequency components, which is consistent with the results in [68]. For higher pulse energy levels, such as 1.52 μJ, the energy transfer changes direction and flows from low to high frequency, which is consistent with the results in [69].

Figure 4.6(b) shows the difference between the peaks in the energy transfer curve for several pulse energies. Positive values correspond to energy transfer from high to low frequency, while negative values correspond to energy transfer from low to high frequency. It can be seen that the difference between the peaks can be as great as 30%. The direction of energy transfer changes between a pulse energy of 1.3 and 1.4 μJ, while for high pulse energies, the energy transfer again approaches zero. This behavior at high energies is most likely due to the formation of multiple filaments.

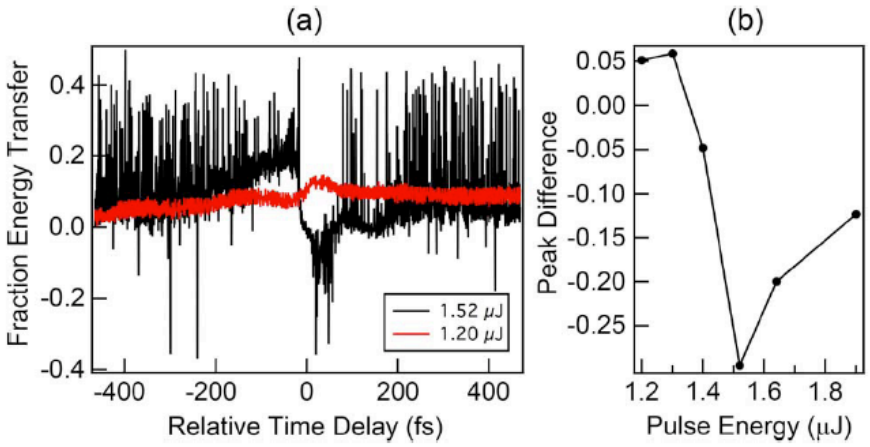

Fig. 4.6 (a) Fraction of energy transfer versus pulse delay for input energies of 1.20 and 1.52 μJ. (b) Difference between fraction of energy transfer curve extrema for several pulse energies [10].

The energy transfer curves shown in Fig. 4.6(a) exhibit a large degree of oscillation; it can be shown that this oscillation is in fact periodic and unique to filament-forming pulses. A typical raw spectral measurement is shown in Fig. 4.7(a) as a function of relative pulse delay. The total time-delay range in the figure is 30 fs, while the two spectral peaks are located at 830 and 780 nm. A fine time-scale energy transfer, on the order of a 1.3 fs pulse delay, can be seen as oscillations in the spectral intensity. The fine time-scale energy transfer spans the entire spectrum. The spectral components of these datasets were integrated to find the power and energy transfer curves (per Eq. 4.72) as a function of relative pulse delay. Figure 4.7(b) shows a typical FFT of an energy transfer curve. The central peak in the FFT at 0.36 fs^{-1} corresponds to the laser carrier frequency. This spectral peak was observed to be entirely absent from energy transfer curves formed from intersecting laser pulses that did not form filaments. This is filament energy exchange on a scale not previously reported.

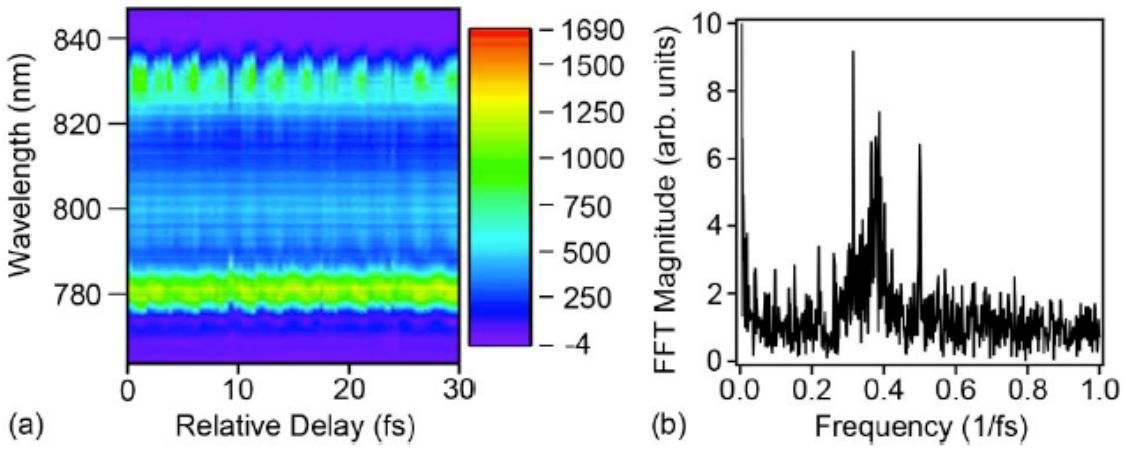

Fig. 4.7 (a) Typical raw spectral measurement of a filament involved in energy transfer in liquid methanol as a function of relative pulse delay. Such raw measurements are spectrally integrated to yield energy transfer curves of Fig. 4.4.4.1(a). (b) Typical FFT of an energy transfer curve for filament-forming, intersecting laser pulses. This FFT peak was completely absent for intersecting pulses that did not form filaments [10].

We next turn to study correlations (or rather anti-correlations) between the output powers for the two beams. Figure 4.8 shows the energy transfer between the fixed and translation-stage beams corresponding to an energy transfer curve at a fine scale, that is, on a time scale on the order of the period of the incident laser pulses. This fine-scale energy transfer is on top of the larger scale energy transfer shown above and which is consistent with results in [68,69]. In Fig. 4.8, data points show the measured energy of each pulse, while the red curves show superimposed, out-of-phase sine functions. The fixed and translation-stage pulse energies are shown by circles and triangles (displaced by 2×10^4 detector counts), respectively. It is important to note that, as can be seen in Fig. 4.8, when one pulse loses energy, the other gains energy, and vice versa.

The presence of fine-scale oscillation was observed for angles between the beams ranging from 1° to 6°, with the observability of the fine-scale oscillation dropping off above 6°. The extreme sensitivity of the phenomenon to alignment makes analysis of this angular dependence a challenge. In addition, we have observed that this fine-scale oscillation in energy transfer between the beams is polarization dependent, and is severely suppressed when the incident beams are orthogonally polarized.

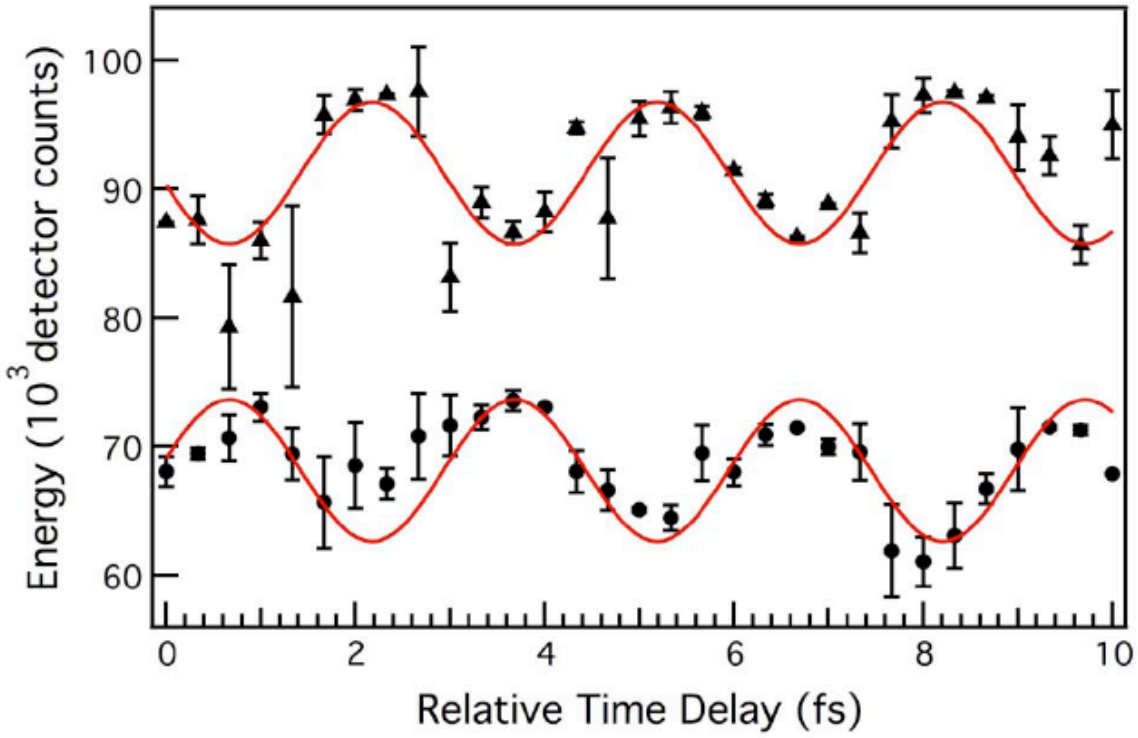

Fig. 4.8 The fine-scale energy transfer between the fixed and translation-stage beams. The measured energies of each pulse are compared to two out-of-phase sine functions. The fixed and translation-stage pulse energies are shown by circles and triangles (displaced by 2×10^4 units), respectively [10].

4.4.5 Crossed filaments as intersecting waveguides

Behavior such as that described above suggests that we have two coherent optical pathways forming a type of a Mach–Zehnder interferometer, where the filament crossing provides the output beam splitter/coupler [77]. The functioning of this beam splitter is possibly similar to the cross-coupling mechanism for a pair of intersecting waveguides. The formation of an intersecting-waveguide structure in a nonlinear Kerr medium has been analyzed by Akhmediev and Ankiewicz [78], who considered linear waves guided by crossed soliton tracks.We find this situation somewhat analogous to our experiment, where the crossed filaments produce a configuration akin to coupled waveguides.
In [78], radiation which probes the resultant intersecting-waveguide structure is found to have crosstalk equal to

$$\frac{T_2}{T_1} = \left(\frac{\tan\theta}{2b} \right)^2 , \tag{4.73}$$

where T_2 and T_1 are the fractional powers of the two output channels when only one input is present, 2θ is the angle between the beams, and b (termed the soliton amplitude) is approximately equal to λ/d, where λ is the wavelength of the radiation and d is a measure of the diameter of the soliton beam. Taking into account that $T_1 + T_2 = 1$ and solving for T_2 yields

$$T_2 = \frac{1}{1 + \left(d \tan\theta / 2\lambda \right)^{-2}} . \tag{4.74}$$

If inputs to both channels are present, the interference visibility V is

$$V = 2\sqrt{T_2 \left(1 - T_2 \right)} . \tag{4.75}$$

Taking the wavelength to be 800 nm and the diameters of the filaments in methanol to be less than 20 μm, the interference visibility has a maximum when the angle between the beams is above 9.1°.

Although we observe the said fine-scale oscillation to be most visible at an angle between the beams of about 2° to 4° and falling off above those values, the overall behavior is similar to the prediction of the above rudimentary intersecting-waveguide analysis in that the visibility of the oscillations increases to a maximum value and then decreases with increasing angle.

CHAPTER V

LASER PULSE ABLATION OF MATERIALS AND LASER-INDUCED BREAKDOWN SPECTROSCOPY (LIBS)*

5.1 LASER PULSE ABLATION OF MATERIALS

Ablation is the removal of a small amount of material from a bulk sample, usually through the mechanism of melting, fusion, sublimation, ionization, erosion, and/or explosion* [79]. Laser pulse ablation of materials, i.e. removing a small part of a bulk sample through laser light/matter interaction, is a highly nonlinear process, and it is useful for many applications. Precision micromachining and laser-induced breakdown spectroscopy (LIBS) are just two examples. In recent years, laser pulse ablation has found applications in space exploration through LIBS instrumentation on the Mars Curiosity rover [80,81]. The body of literature regarding this subject and the applications which spring from it are rapidly increasing. In this section, we discuss the various mechanisms of laser pulse ablation and how laser pulse characteristics such pulse duration can affect them.

The essence of ablation using a laser pulse is the deposition of energy into a small sample of material such that the energy absorbed results in an explosive action. The energy absorption mechanisms depend on pulse duration [79,82]. With nanosecond

---

* Reprinted with permission from "Chemical-specific imaging of shallowly buried objects using femtosecond laser pulses" by B. D. Strycker, K. Wang, M. Springer, and A. V. Sokolov, 2013. *Applied Optics*, 52, 4792-4796, Copyright 2013 by Optical Society of America.

laser pulses, the dominant energy absorption mechanisms are thermal in nature. However, with femtosecond laser pulses, the dominant energy absorption mechanisms are electronic (tunneling ionization, Coulomb explosion, etc.). Picosecond pulses tend to be a combination of these two extremes, exhibiting both thermal and electronic energy absorption mechanisms [79]. We will consider the energy absorption mechanisms that result in ablation in the extremes of nano- and femtosecond laser pulses, understanding that picosecond laser pulse ablation is often a combination of the phenomena exhibited in nano- and femtosecond pulse ablation.

When pulse duration is on the order of a few nanoseconds and the intensity is less than about 10^8 W/cm^2, thermal processes are the dominant ablation mechanisms. These include laser radiation absorption by the material, which results in a temperature increase in that part of the material which absorbs energy. Eventually (and this can happen in a time on the order of a new nanoseconds) the temperature will increase to the point that the material will melt and vaporize. If enough energy is absorbed quickly enough, explosive vaporization will result in ablation of a small portion of the bulk material. The temperature distribution in the target can be calculated according to the heat conduction equation [79]:

$$\frac{\partial T(x,t)}{\partial t} = \frac{\partial}{\partial x}\left[\left(\frac{\kappa}{C_p \rho_s}\right)\frac{\partial T(x,t)}{\partial t}\right] + \frac{\alpha}{C_p \rho_s} I(x,t) \ , \tag{5.1}$$

where T is the temperature inside the target, x is the distance from the surface, κ is the thermal conductivity, C_p is the heat capacity, ρ_s is the mass density, α is the optical absorption coefficient, and I is the intensity of the laser pulse. From this equation it can

be seen that a significant rise in temperature can occur if energy is deposited within a volume faster than the energy can be conducted away from the volume through thermal contact. This is what happens in nanosecond laser pulse ablation where thermal processes are dominant, resulting in explosive vaporization of the material.

The vapor produced by ablation can be ionized by the remainder of the laser pulse, resulting in avalanche ionization and the formation of a plasma. When this happens, the region containing the plasma expands in a direction opposite to the laser pulse propagation, i.e. the plasma shields the material from the remainder of the laser pulse. This is called *plasma shielding*. For nanosecond laser pulses, if the incident pulse peak intensity is greater than about 10^8 W/cm^2, ionization can play a role in the ablation process in addition to the thermal mechanisms described above. For femtosecond laser pulses, however, electronic and ionization processes are dominant.

Because femtosecond laser pulses are so short, any plasma produced in the material by the pulse forms after the pulse has already passed and interacted with the material. Plasma shielding does not, therefore, play a significant role in femtosecond laser pulse ablation. However, it may or may not play a significant role in picosecond laser pulse ablation, depending on the pulse intensity. When a femtosecond laser pulse of sufficient intensity interacts with a material, it can ionize the material through tunneling, multi-photon, and avalanche ionization processes, which we discussed and outlined in Section 4.2. Some of the free, excited electrons have enough energy to leave the material, and when roughly 10% of the valence electrons are removed, the material lattice structure is weakened and begins to melt. This is called non-thermal melting, and

it is caused by high energy electrons and ions [79]. The melted material, consisting of positive ions (which have gained energy through Coulomb interaction with the excited electrons) and negative electrons, expands outward in a type of explosion. Thus the material is ablated.

In nanosecond, picosecond, and femtosecond ablation, the ablated material and plasma is ejected outward and primarily away from the material surface. Since the ejection velocities are often faster than the speed of sound in the surrounding medium, acoustic shockwaves often result from the ablation process. Also of interest is the emission of light from the excited plasma, which can be used to identify the chemical composition of the ablated material. We consider this process in the next section.

5.2 LASER-INDUCED BREAKDOWN SPECTROSCOPY (LIBS)

5.2.1 Generation of signal

In the previous section we discussed the generation of an excited plasma consisting of ions and electrons of the target material. As mentioned above, this plasma is ejected from the material at high velocities. As a result and through possible further interaction with the laser pulse, the ions and electrons emit light into 4π steradians solid angle. We note that plasma interaction with the laser pulse occurs only with nanosecond laser pulses and, depending, in picosecond pulses. Femtosecond pulses are in general so short in duration that any plasma generated by the pulse is formed after the pulse has been absorbed by the target material.

The excited electrons in the plasma emit a continuous Bremsstrahlung emission through collisions with ions. This Bremsstrahlung emission is broadband and incoherent in nature. It effectively functions as a background radiation that can hide the signal of interest. However, as light is emitted, the electrons lose energy, and therefore the intensity of the Bremsstrahlung emission decays with time. The exact decay time is often a function of experimental parameters, but typical decay times for LIBS using nanosecond pulses can range from ten to hundreds of nanoseconds. It should be noted that in femtosecond LIBS, the decay times are much shorter, and the Bremstrahlung emission is much less than it would be if nanosecond pulses were used [79]. This makes it possible to use what is called a non-time-gated LIBS technique, the physical basis for which comes from the different decay times of the light emitted by the electrons (continuum Bremmstrahlung) and the ions, which emit light corresponding to energy differences in atomic and/or molecular levels.

Excited ions typically emit light on a time scale exceeding that of the electron Bremsstrahlung radiation, making it possible to improve the signal to noise ratio of the LIBS signal, which is in practice the light emitted from the ions of interest over the background electron Bremsstrahlung radiation, through use of a time-gating technique. By measuring the spectrum of the light emitted by the excited LIBS plasma tens to hundreds of nanoseconds after the pulse has hit the target, the longer lifetime of ion line emission makes it possible to resolve spectral lines. As mentioned before, this technique is most useful in nanosecond LIBS, as the femtosecond LIBS signal can often be retrieved with time-gating. However, time-gating the LIBS signal almost always results

in an improvement of the signal-to-noise ration. In the LIBS signal, which consists of a measured spectrum, the spectral lines of the ions can be used to identify the target material because they correspond to unique energy levels. The amplitude of spectral lines may also be used to determine the quantity of specific elements or chemicals within a target sample.

Dual pulse LIBS has also been used to boost signal levels. For dual pulse LIBS, the plasma generated by the first laser pulse is then heated by a second pulse, resulting in increased plasma excitation and emitted light. Dual pulse LIBS has been used with success for submerged targets, where laser pulses incident upon an underwater object generate a plasma which subsequently expands into a bubble. A second pulse then heats the gas and plasma inside the bubble, resulting in a greater signal than would be have been retrieved using only one pulse [79]. In general. different experimental geometries for dual pulse LIBS have been utilized, including collinear, orthogonal, and orthogonal pre-ablative spark heating.

The simplicity of LIBS setups lends itself to broad application, both in the laboratory and in the field. In the field, remote LIBS applications are becoming of increasing interest.

5.2.2 Remote operation

Remote LIBS typically has several important components in its experimental setup. A laser that outputs energetic nanosecond to femtosecond laser pulses is mounted on a mobile land-, water-, or air-based platform. The beam is focused by optical

components which may or may not include adaptive schematics. The laser pulse then propagates through the intervening medium which separates the laser and the target. This distance may span tens to hundreds of meters. After the pulse interacts with the target, the LIBS signal is collected at the observation point (which is often in the same location as the laser itself), often using some type of telescope mirror or lens. The collected light is directed into a spectrometer connected to a computer, and the spectrum is recorded.

The simple setup has recently been implemented on the Mars Curiosity rover [80,81]. A challenge that can arise with this setup is the focusing of the energetic laser pulses at large distances. Atmospheric perturbations from turbulence can result in distortion of the wavefront, making it difficult to obtain a focused geometry at the target location. A solution to this problem is the use of femtosecond laser pulse filamentation; energetic femtosecond laser pulses self-focus and generate filaments. When filaments are used in a remote LIBS setup, the focusing optics can be removed from the setup, because the natural self-focusing action of the pulses results in focused propagation over large distances [1–3]. LIBS using femtosecond laser pulse filamentation is often called filament-induced breakdown spectroscopy (FIBS). Applications using FIBS are currently of great interest and may be increasingly implemented in the future.

Having discussed the basic physics and setups of LIBS and FIBS setups, we now describe an experiment which takes advantage of the different breakdown potentials of various materials in using LIBS to image shallowly buried objects in sand with chemical specificity. Although the experiment is performed within the laboratory, in principle the setup and physical processes may be applied in the field to obtain the same results.

5.3 CHEMICAL-SPECIFIC IMAGING OF SHALLOWLY BURIED OBJECTS USING FEMTOSECOND LASER PULSES

5.3.1 Remote sensing of shallowly buried objects

Remote detection and imaging of buried objects has long been a topic of practical interest. Probing of various geologic features, such as ice sheets, soil, and rock with radar technology has now become commonplace [83,84] with applications in the fields of geology, climatology, agriculture, and archaeology. However, one disadvantage of using radar technology to image or detect buried objects is that the resolution of the retrieved images or data is limited by the large wavelength of the probing radiation. Accurate imaging of objects with sizes on the order of 10 cm or less then becomes a significant challenge. One field in which accurate, high-resolution imaging of buried objects would prove useful is landmine detection. Ground-penetrating radar has been used in detection of landmines [85], yet this technique presents several difficulties in that soil inhomogeneities, water pockets, rocks, and various roots can register false positives. Remote identification or differentiation of object materials in addition to accurate information on spatial relationships would reduce the false positive rate and be a boon in the effort to protect civilian and military personnel. This may be achieved through utilizing the laser-induced breakdown spectroscopy (LIBS) signal in constructing images of remote targets.

In LIBS, a small portion of the target sample absorbs energy from an incident

laser pulse and is ablated, resulting in sample vaporization, plasma formation, and ejection of fine particles [79,82,86,87]. The formation of plasma results in an excitation of sample atoms and/or molecules, which subsequently emit characteristic light radiation over time periods ranging from picoseconds to microseconds, depending on the experimental parameters [79,82]. The measured spectrum of emitted light may, therefore, be used to identify the sample. In this experiment, we present a method by which high resolution images of shallowly buried objects may be retrieved, and, in addition, by which their materials and chemical compositions may be differentiated and identified. Our work expands upon the principles Grönlund et al. have used to construct a chemical specific image of an array of metal plates from a distance of 60 m [88]. Their pulses had a duration of 4–5 ns and an energy of 170 mJ. Beam diffraction was compensated with a beam expander and focusing optics; even so, with an expected theoretical beam diameter of 0.7 mm, they achieved an experimental beam diameter of 5 mm at the target distance of 60 meters. We propose that the beam expanding optics may be eliminated and the beam diameter at the target reduced with the use of femtosecond laser filaments. The self-focusing action of intense femtosecond laser pulses leads to filament cores with diameters on the order of 100 μm that persist beyond the Rayleigh length of linear optics and that may be formed remotely at distances of tens to hundreds of meters [44]. The use of filaments in remote LIBS (filament-induced breakdown spectroscopy (FIBS)) is well-documented [1–3]. We have remote sensing applications in mind in our experiment, in which we investigate the use of femtosecond laser pulses in constructing chemical-specific images of shallowly buried objects. We

achieve results similar to those in [88] using pulses with two orders of magnitude less energy and with a technique having potential to achieve 100 μm resolution at distances of hundreds of meters. Such a method may prove useful in a balanced approach to landmine detection and may find uses in various other fields in which high-resolution differentiation and identification of chemical composition is paramount.

5.3.2 Experimental setup for imaging objects buried in sand

Our experimental setup is shown in Fig. 5.1. We use a Ti:sapphire-based laser system consisting of an oscillator (Micra, Coherent) and an amplifier (Legend Elite, Coherent: 800 nm center wavelength, 35 fs pulse duration, 1 kHz repetition rate, 4 mJ pulse energy). A 1 m focal length lens focuses the femtosecond pulses onto the sample (in this case various metallic objects buried in sand), the surface of which is 100 cm from the lens. A collection lens with a 10 cm focal length then collects the laser-induced breakdown signal and couples it to the fiber optic input of a spectrometer (HR4000CG-UV-NIR, Ocean Optics), while a short-wave-pass (SWP) filter ensures that the strong pump-beam signal centered at 800 nm wavelength does not overpower the desired signal in the visible region of the spectrum. The axis of the light-collecting apparatus makes an angle of about 30° with respect to the pump beam. We note that the elements of the light-collecting apparatus may in principle be scaled for use in remote sensing setups. In order to retrieve an image, the sample is scanned in two dimensions with a translation stage (CMA-25CCCL, SMC100, Newport); in remote sensing applications, it is the beam itself that is scanned two-dimensionally across the sample.

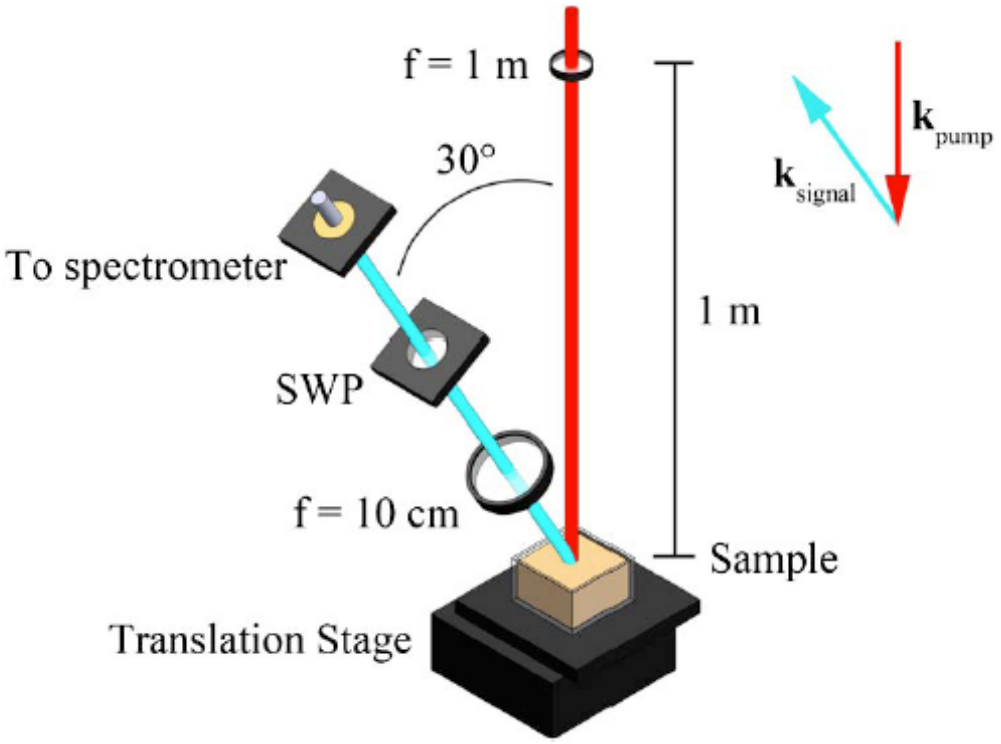

Fig. 5.1 Experimental setup. The pump beam is directed downward and focused by a 1 m lens upon the sample. Upward-directed signal light is collected with a 10 cm lens and passed through a SWP filter before analysis with a spectrometer. For remote sensing applications, the light-collecting apparatus must be scaled appropriately and the beam instead of the sample must be scanned in two dimensions [11].

The sand used to bury the objects is taken from Quickrete Premium Play Sand, Product 1113, composed of crystalline silica. The majority of sand grains are measured to have a diameter of 275 (+150, −75) μm. We measure the linear optical irradiance extinction coefficient at 800 nm in a manner similar to that in [8], in which the transmission through two optical pathlengths is measured. We measure a linear optical irradiance extinction coefficient of $c = 0.55 \pm 0.02$ mm^{-1} at 800 nm, which is the central wavelength of the laser pulse. The top surfaces of the buried objects are placed 2.0 mm below the top edges of the sample container and are covered with unpacked sand. Excess

sand is then scraped off. The uncertainty of the depth of the objects is ± 0.3 mm, which is about the size of two sand grains.

5.3.3 Construction of images from LIBS signals

Figure 5.2 shows the retrieved signal spectra from various metallic objects buried 2.0 ± 0.3 mm deep in sand. Each spectrum has been vertically displaced in order to aid visualization. The black curve is one of several retrieved spectra from sand; being inhomogeneous, there is some variation in the spectrum, particularly in a peak around 600 nm. However, the metallic samples may still be easily distinguished from the sand. The blue curve in Fig. 5.2 is that from buried aluminum. The green and red curves are those belonging to buried copper and stainless steel, respectively. Note the strong spectral peaks in aluminum near 400 nm and the peaks in copper near 520 nm that may be used to identify the metals and which are similar to FIBS spectra seen in [1–3], respectively. Stainless steel is most easily differentiated in our experiment by the broad, continuous spectral emission in the range of 550–700 nm.

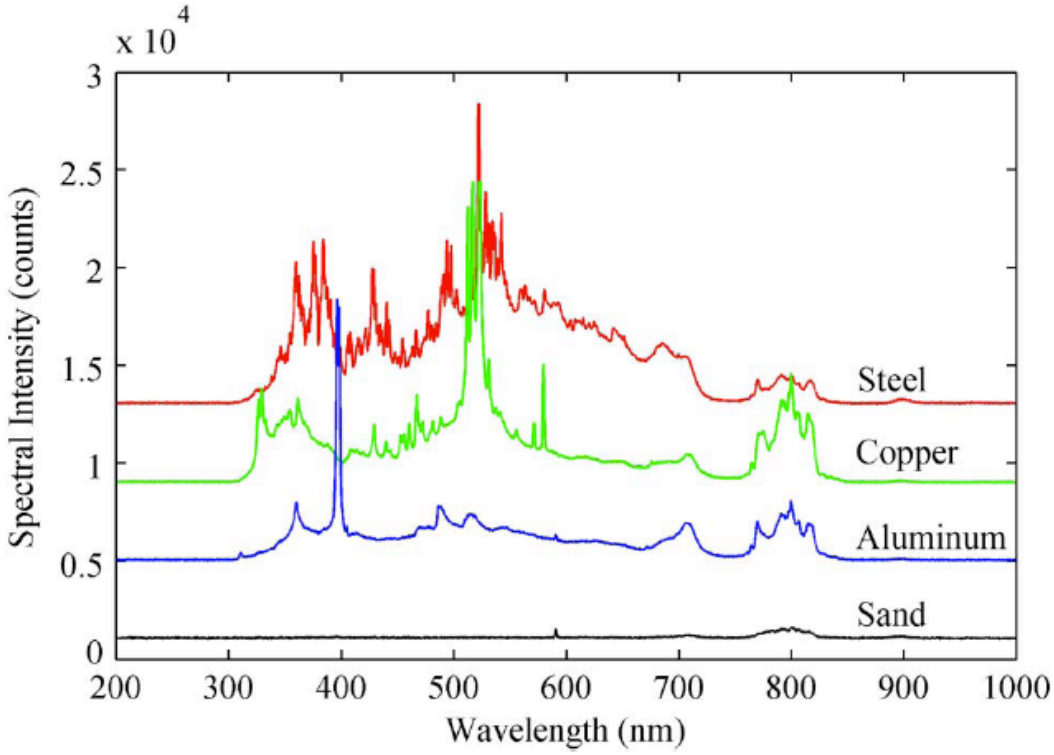

Fig. 5.2 Retrieved spectra of sand (black), aluminum (blue), copper (green), and stainless steel (red) using the setup shown in Fig. 5.1. Each spectrum has been vertically displaced to aid visualization. The metallic samples have been buried beneath 2.0 ± 0.3 mm of sand [11].

The spectra shown in Fig. 5.2 may be used to identify each material in images retrieved by recording spectra generated at different coordinates in the sample. Figure 5.3 shows how such an image may be constructed using femtosecond pulses with 2.5 mJ energy. In Fig. 5.3(a) are shown a circular stainless steel washer (center), copper bar (top), and aluminum bar (right). Figure 5.3(b) shows the same metallic objects after being buried beneath 2.0 ± 0.3 mm of sand. The metallic objects cannot be seen with the eye. Finally, Fig. 5.3(c) shows a composite 31 by 31 pixel RGB image of the buried objects, with the aluminum, copper, and stainless steel metals identified with the blue,

green, and red color components, respectively. The dimensions of each pixel are determined by the stage step size and are 0.4 mm × 0.4 mm, making the total size of the image 12 by 12 mm. In principle even greater spatial resolution may be achieved, since the image in Fig. 5.3(c) is not diffraction-limited. Femtosecond laser filaments might be used to achieve resolution on the order of 100 μm at a distance of tens to hundreds of meters [89] and may prove especially useful in remote sensing applications [1–3]. The RGB components of the composite image in Fig. 5.3(c) are obtained by integrating the retrieved spectra over different spectral windows after ambient background signal has been subtracted. To retrieve the B component, each retrieved spectrum was integrated from 393.9 to 402.0 nm, resulting in an image where aluminum yields the greatest signal intensity. The G component was retrieved by integrating every spectrum over the 508.1 to 528.1 nm spectral window, resulting in an image where copper yields the greatest signal. Finally, the R component, corresponding to stainless steel, was retrieved by integrating over the broad spectral range from 528.1 to 632.2 nm. The combination of the RGB components yields the image shown in Fig. 5.3(c), which not only shows the presence and spatial relationships between objects but also differentiates and identifies the materials from which the objects are made. We note that the above scheme for identifying various metals from retrieved spectra may be improved easily with more sophisticated algorithms, for example utilizing correlations with standard database spectra of various materials [90]. Time-gated measurement techniques may also allow greater spectral resolution and accuracy. However, even with the very simple integration method outlined above, material differentiation is still possible. We note that after

irradiation, the surfaces of the samples had been ablated and blackened, so that the samples were damaged. The sand, however, had not been melted, burned, or significantly changed in color.

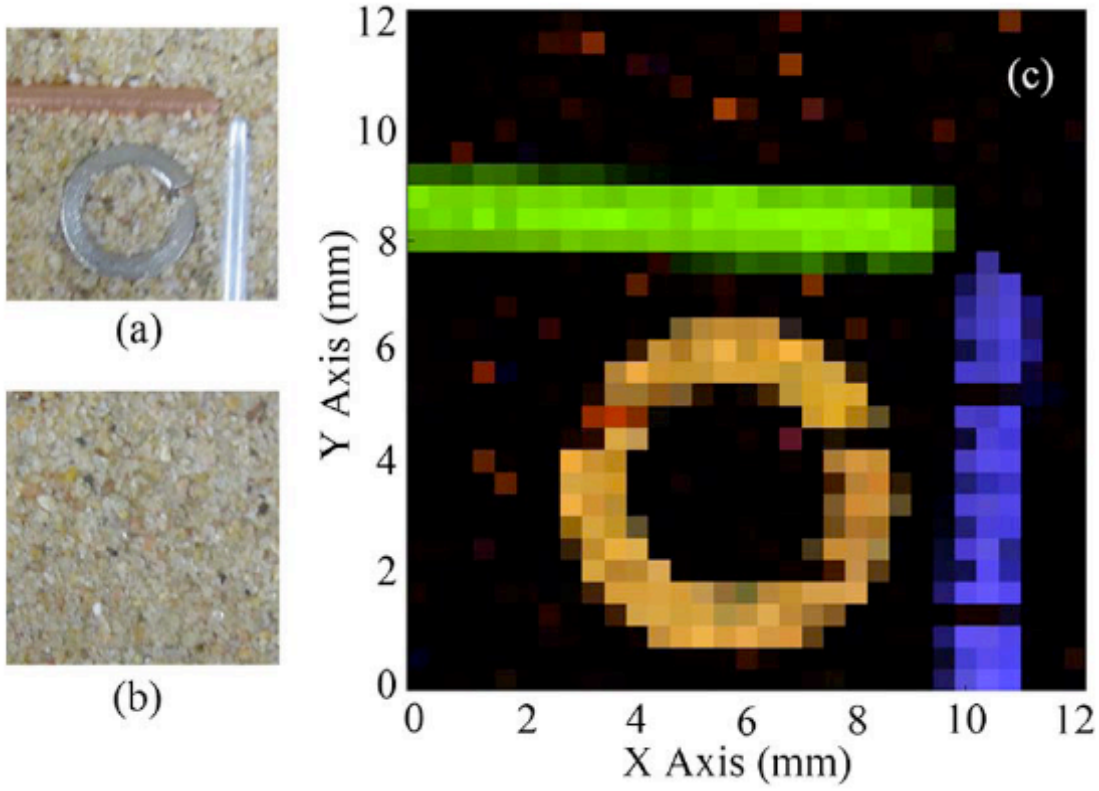

Fig. 5.3 (a) Circular stainless steel washer (center), copper bar (top), and aluminum bar (right). (b) The same metallic objects buried beneath 2.0 ± 0.3 mm of sand. (c) Composite RGB image of the buried objects with aluminum, copper, and stainless steel corresponding to the blue, green, and red color components, respectively [11].

In order to determine the depth from which a useful signal may be retrieved in our setup, we buried an aluminum plate at an angle of about 35° with respect to horizontal. We then performed a one-dimensional scan along the direction of increasing

sand depth from an initial depth of 0 mm, recording each spectrum using the setup shown in Fig. 5.1. Since the target material is aluminum, we define the retrieved signal to be the integral of each spectrum from 393.9 to 402.0 nm (spanning the peak around 400 nm for the aluminum spectrum shown in Fig. 5.2) minus an identical integration window immediately adjacent from 383.5 to 393.9 nm. By passing the beam through a neutral density wheel, pulse energies ranging from 0.200 ± 0.015 mJ to 2.455 ± 0.015 mJ were used with three separate scans performed per pulse energy. The average of the three retrieved signals was taken to determine the relationship of the signal amplitude to the depth from which it was retrieved. These results are shown in Fig. 5.4, which graphs the natural logarithm of the retrieved signal intensity as a function of the pulse energy as well as the depth from which the signal was measured. In Fig. 5.4, the background level is about 5. An appreciable signal cannot be detected from any depth until the pulse energy is greater than or equal to about 0.55 mJ. Notice that at a pulse energy of about 2.3 mJ, a distinguishable signal may still be retrieved from a depth of 3.6 mm. The black curve shows the relationship $E_{th} = E_0 \exp[-cz]$, where E_{th} is the threshold pulse energy 0.55 mJ required for signal detection, E_0 is the incident pulse energy, c = 0.55 mm^{-1} is the linear optical extinction coefficient of the sand measured above, and z is the depth from which the signal is measured. The data follow this relationship well, indicating that pulse propagation dynamics for the pulse energies used appear to be primarily linear in nature.

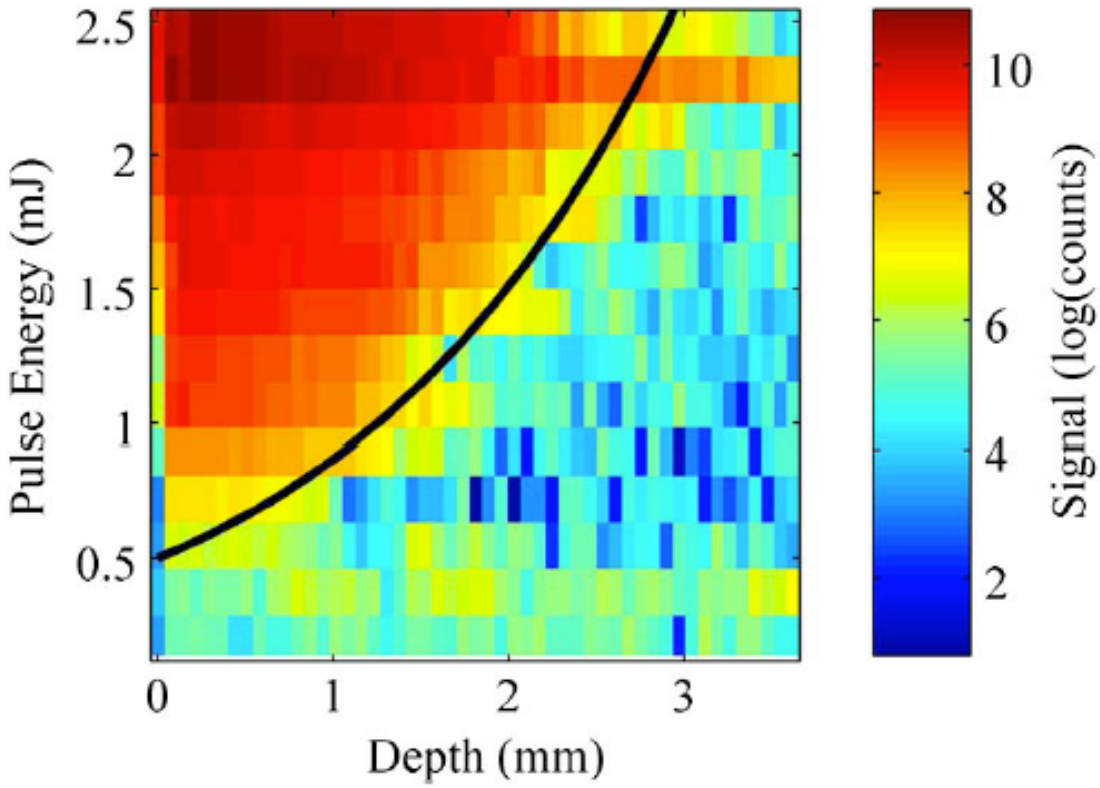

Fig. 5.4 Natural logarithm of the received signal intensity as a function of pulse energy and depth. The curve shows the relationship $E_{th} = E_0 \exp[-cz]$ [11].

The pulse energies used in the above experiment are sufficient to induce laser pulse filamentation through self-focusing in the pulse propagation region before the geometrical focus [44]. Burn-paper analysis of our beam indicates that while filamentation is likely a dominant pulse propagation dynamic in the region before the geometric focus of the lens, within the geometric focus itself the beam diameter is determined by geometric optics.

Our data suggest that, while nonlinearities may be present within the sand grains themselves, the net absorption and scattering experienced by the pulse while propagating

through the sand may be described by linear radiative transfer. Experimental results indicate that the majority of radiation is scattered within 10° of the forward direction, a range of angles that may be described by the small angle scattering approximation. Temporal and spatial pulse spreading due to small angle scattering are described in [91,92]. According to [91], the optical depths involved in our experiment fall within the range of validity of an analytic estimate of the temporal pulse spread due to scattering. For a sample buried z = 2.0 mm in sand, the optical depth is $\tau = cz = 1.1$, where c = 0.55 mm^{-1} is the optical extinction coefficient measured above. According to Eq. (25) of [91], the temporal spread $\langle t \rangle$ of the pulse due to scattering is $\langle t \rangle = z / \tau(1-\omega_0)c_0$, where ω_0 is the single scattering albedo (ratio of scattering to total extinction), and c_0 is the speed of light in the base medium. Assuming that the speed of light does not appreciably differ from that in vacuum, and that the single scattering albedo of the sand has a value between ω_0 = 0.0 and 0.9 [93], the estimated maximum temporal spread of the 35 fs laser pulses due to scattering after propagation through 2.0 mm of sand ranges from $\langle t \rangle$ = 6.1 to 61 ps.

The above estimates of temporal spreading of the pulse due to scattering suggest that, even though the duration of the 35 fs pulse may be increased to as much as 60 ps, the ablation of the metal targets buried beneath 2.0 mm of sand depend mainly on the pulse energy fluence. In our experiments, while a possible significant increase in pulse duration may be a deciding factor in what kind of ablation mechanisms dominate [79], ablation may still occur through various processes regardless of the temporal pulse

spreading. For the range of estimated pulse durations listed above, i.e., 6 to 60 ps at a depth of 2.0 mm in sand, the main factor limiting the onset of target ablation is therefore the energy deposited into the sample during the duration of the pulse. Hence the depth of the detected LIBS signal depends on the linear optical extinction coefficient, as shown in Fig. 5.4, which governs the fluence delivered to the target. This conclusion is supported by additional experiments investigating the effect of pulse chirp on unburied metal target ablation. Pulse chirps resulting in pulse durations on the order of picoseconds still resulted in ablation of the metal targets. The small angles at which radiation is scattered by the sand suggest that, for the depths investigated, significant beam spreading is not a deciding factor in target ablation. The LIBS signal itself, which originates in the ablated plasma at and above the target surface and may therefore originate at slightly lesser depths than the target itself, experiences primarily linear absorption and scattering.

5.3.4 Applications for imaging buried objects

In conclusion, we have demonstrated that shallowly buried objects may be imaged with submillimeter resolution using femtosecond laser pulses having energies two orders of magnitude less than that used in previous works [88]. We have investigated the depth from which a reliable signal may be retrieved using the above configuration. Measurement of laser-induced breakdown signals may in principle be performed in standoff or remote setup geometries. Research in the use of novel beam shapes or drilling techniques may also yield results aiding in retrieval of signals from

greater depths [94,95]. Time-gated measurement techniques, which reduce the background plasma continuum contribution to the measured spectra, may also aid in increasing depth. Dielectric samples may also, in principle, be imaged. We have measured the LIBS signal of PVC using femtosecond laser pulses and find the pulse energy required for ablation is 0.65 ± 0.01 mJ, which is comparable to the pulse energy required for ablation of metals.

We also point out that, in addition to many terrestrial applications, the above method may find ample use in space exploration. One of the advantages of using LIBS in space exploration is the ability to remove dust layers from target samples [79,80]. The above method using femtosecond laser pulses, however, may retrieve useful spectrographic signals from samples buried several millimeters deep in large-grained sediments, which may not be easily removed. Even in finer-grained dust, our results have shown signal retrieval from several millimeters deep. Such an ability may prove useful in many space and planetary environments and is achieved using pulse energies less than those typically used for nanosecond LIBS in the same environments [80,81].

CHAPTER VI

FEMTOSECOND-LASER-INDUCED SHOCKWAVES IN WATER GENERATED AT AN AIR-WATER INTERFACE*

6.1 FEMTOSECOND LASER PULSES FOR MARINE REMOTE SENSING APPLICATIONS

The generation of acoustic shockwaves in optically transparent and absorbing liquids via intense laser radiation has been of interest since shortly after the invention of the laser[*]. In 1963, Askar'yan *et al.* were the first to observe shockwave generation through light absorption and thermal expansion in a liquid [96]. The next year, in 1964, Brewer and Rieckhoff observed shockwaves induced by dielectric breakdown in a liquid [97]. A number of subsequent works investigating the phenomena involved with laser-induced shockwaves in liquids were outlined in a review paper published by Bunkin and Komissarov in 1973 [98]. The next decade saw significantly increased productivity in this area, resulting in two more well referenced review papers published in 1980 and 1981 [99,100]. By this time, three main physical mechanisms for shockwave generation by laser radiation in liquids had been identified: linear optical absorption with subsequent bulk thermal expansion, explosive evaporation, and dielectric breakdown and ionization.

---

[*] Reprinted with permission from "Femtosecond-laser-induced shockwaves generated in water at an air-water interface" by B. D. Strycker, M. Springer, A. J. Traverso, A. A. Kolomenskii, G. W. Kattawar, and A. V. Sokolov, 2013 (in press). *Optics Express*, copyright 2013 by Optical Society of America.

At the end of the 1980's and beginning of the 1990's, the field had become well-established, and definitive monographs and textbooks were written [101–104]. In the 1990's, it was realized that shockwaves in liquids had applications in medical surgery and biological tissue ablation, and renewed interest resulted in several works analyzing the generation of shockwaves in water using nanosecond and picosecond laser pulses [105–108]. By this time, femtosecond laser systems had come into widespread use, and characterization of femtosecond-laser-induced shockwaves in tissue and water for medical purposes was undertaken. In the 2000's, research into femtosecond-laser-induced shockwaves continued along these lines [108–115], with applications broadening into cell processing, optical trapping, and fluidic control [113–115]. Reviews of femtosecond laser nanosurgery and shockwave emission by laser-generated bubbles have also been written [116,117].

Our own interest in femtosecond-laser-induced shockwaves in water stems from the discovery and development of applications involving femtosecond laser filaments [44]. Specifically, we have in mind applications in remote sensing from air-based platforms over oceanic and riverine environments. Femtosecond laser filaments in air are formed from laser pulses having energies on the order of a few millijoules. Several works have sought to characterize the interaction between potentially filament-forming femtosecond laser pulses in air and water-micro-droplets in the atmosphere. Of these, major foci have been the explosion of water micro-droplets by femtosecond laser pulses [118,119] and plasma formation, transmission, harmonic generation, and white-light generation within the micro-droplet [120–127]. Dynamics of plasmas formed by

femtosecond laser pulses incident onto planar water jets have also been studied [63,128,129]. Shockwaves cannot, however, propagate appreciable distances in micro-droplets or water jets, and so, remarkably, little to no work has been done investigating the acoustic phenomena involved when a femtosecond laser pulse with energy on the order of a few millijoules propagates across an air-water interface separating large volumes of bulk media. This basic science is prerequisite to any remote sensing applications that may be developed from femtosecond laser filaments in air interacting with the surface of a body of water. Previous works investigating laser pulse interaction with air-water interfaces have utilized nanosecond pulses with wavelengths in the mid- to far-infrared [130–141]. Oshemkov *et al.* [142] have investigated jet formation at an air-water interface using femtosecond laser pulses in tightly-focused geometry. Acoustical responses were not investigated, however. While many of these works document shockwaves generated from thermal expansion of heated water or explosive evaporation [100], the shockwaves we have generated using femtosecond laser pulses originate from dielectric breakdown and ionization of water at the air-water interface. This experiment is dedicated to reporting and describing the shockwaves generated by femtosecond laser pulses with energies of a few millijoules. Section 6.2 describes our experimental setup. Section 6.3 briefly describes the phenomenological context in which the shockwaves occur, while Section 6.4 focuses on the characteristics of the shockwaves themselves. Section 6.5 discusses the physics and generating mechanisms responsible for the shockwaves and possible applications. Finally, Section 6.6 contains our conclusions.

6.2 EXPERIMENTAL SETUP FOR IMAGING SHOCKWAVES IN WATER

Our experimental setup is shown in Fig. 6.1. The pump laser that is used to generate the shockwaves is a Ti:sapphire-based laser system consisting of an oscillator (Micra, Coherent) and an amplifier (Legend Elite, Coherent: 800 nm center wavelength, 35 fs pulse duration, 1 kHz repetition rate, 4 mJ pulse energy). The pump beam propagates into a tower and is directed downward to the surface of a distilled water sample after passing through a focusing lens with a 100 cm focal length. The surface of the water sample is located 100 cm from the lens. The tower itself may be pivoted such that the angle of incidence θ of the pump beam with respect to the normal of the surface of the water sample can be changed to the desired value. The distance from the surface of the water sample to the lens remains constant at 100 cm. Before entering the tower, the pump beam passes through a waveplate that is rotated to ensure that the pump beam remains p-polarized with respect to the surface of the water sample regardless of the pivoting angle θ of the tower; however, no polarization-dependent phenomena were observed in this experiment. A neutral-density wheel attenuator is utilized to control the energy of the pulses at the water surface. Measurements of pulse energy were taken between the neutral-density wheel attenuator and the first mirror of the tower. All pulse energies and calculated intensities quoted in this work have been corrected for reflection from three mirrors and transmission through the 100 cm focusing lens, yielding the pulse energies and intensities at the water surface.

In order to probe the phenomena induced by the pump pulses, we use the 532 nm

output of a frequency-doubled 1064 nm beam from a Precision II 9000 Nd:YAG laser by Continuum. The 532 nm probing pulse has a FWHM duration of 7.8 ns. The probe beam is horizontally incident onto the water sample and is orthogonal to the incident pump beam; after interacting with the water sample, the probe beam is imaged by a 5 cm focal length lens onto the CCD of a Nikon D40 camera from which all objectives have been removed. The timing between the pump pulse, probe pulse, and camera triggering is controlled electronically. In this manner, we are able to observe phenomena that take place on time scales ranging from a few nanoseconds to milliseconds and beyond.

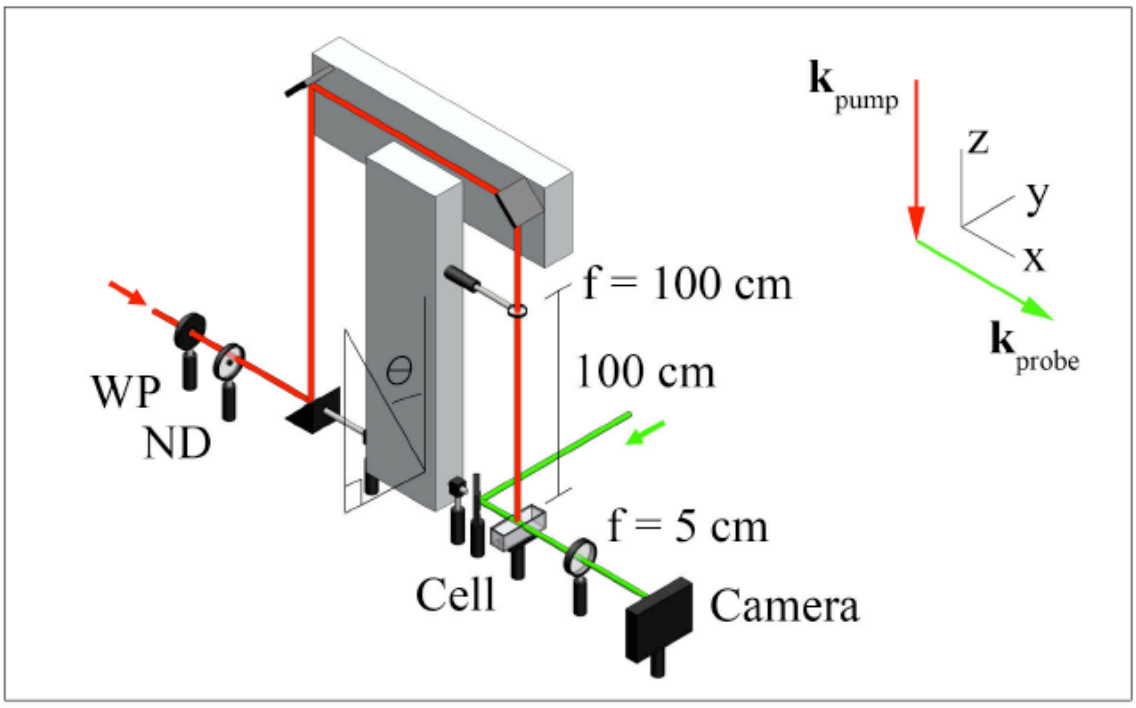

Fig. 6.1 Experimental setup for probing phenomena induced by 800 nm, 35 fs pump pulses with millijoule energies incident upon an air-water interface. The tower can be pivoted through an angle θ, which is also the angle of incidence of the pump pulse with respect to the water surface normal. WP = half wave plate, ND = neutral density filter [12].

6.3 OUTLINE OF PHENOMENA AND CORRESPONDING TIME SCALES

Figure 6.2 illustrates the phenomena involved when a loosely focused femtosecond laser pulse (35 fs duration, 800 nm central wavelength) with an energy of 1 to 2 mJ interacts with the surface of a sample of water. The time scales of the phenomena span at least 12 orders of magnitude, ranging from the femtosecond to the millisecond. On the femtosecond time scale, the loosely-focused, energetic pulse reaches intensities sufficient to ionize many of the water molecules, creating at the surface a region of dense plasma (see Fig. 6.2(a)). The plasma then subsequently expands upward from the surface on the picosecond and nanosecond time scales. In the region directly above the surface of the water into which the plasma has expanded, a light signal is emitted from the excited plasma species (Fig. 6.2(b)). At the same time, acoustic shockwaves in both air and water are generated and expand from the interaction region. Figure 6.2(c) shows shockwaves in both air and water 490 ns after the pulse has passed. A unique feature of the shockwaves we have generated in water is the presence of two shock fronts. The processes giving rise to these different shock fronts are discussed in the following sections. After about 10 microseconds, a cavity (crater) is formed on the surface of the water that expands downward into the bulk. Figure 6.2(d) shows one of these cavities at about 20 μs after the pulse has passed. The downward expansion of the cavity continues until about 100 microseconds, when the surface of the water closes above the cavity and forms a bubble. Figure 6.2(e) shows a bubble at about 200 μs after the initial pulse has passed. The bubble continues to propagate downward into the bulk of the sample for several milliseconds, reaching depths of at least 500 microns, after

which it eventually returns to the surface.

The many time scales over which these phenomena span provide for rich opportunity for ongoing research. On the femtosecond time scale (Fig. 6.2(a)), the mechanisms and dynamics of ionization for these high intensities and their relation to the process of liquid surface ablation remain intriguing areas for additional investigation. On the microsecond time scale, the fluid dynamics responsible for the formation of the cavity at the surface and the subsequent cavity closure and bubble propagation may prove interesting in studies involving fluidic control. Our focus in this experiment, however, remains the mechanisms immediately responsible for shockwave generation and their subsequent characteristics as they propagate away from the air-water interface as a result of femtosecond pulse propagation and interaction across the surface. Consequently, the following sections will focus on the picosecond and nanosecond time scales, during which a portion of the water surface is ablated and leads to the formation of the two shock fronts shown in Fig. 6.2(c).

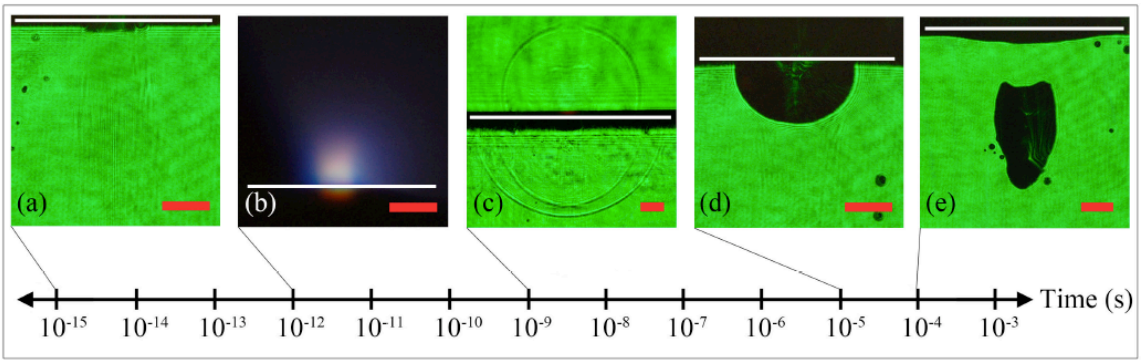

Fig. 6.2 Outline of events induced by femtosecond laser pulses of few millijoule energies incident on an air-water interface. The red scale bars in the lower right corners are 200 μm in length. The white lines show the approximate position of the air-water interface, with air above and water below. Each picture is shown to be associated with an approximate time scale on which the phenomenon may first begin to be observed. (a) Ionization, plasma generation, and electron-ion thermalization at and beneath the surface, corresponding to the slightly darker region of about 200 μm width in the center of the picture. (b) Plasma expansion from the surface and emission of light. This image was taken without the use of the 532 nm probe pulse. (c) Generation of shockwaves both above and below the surface. Notice the two shock fronts generated within the water sample. (d) Cavity formation at the surface. (e) Cavity closure and bubble formation [12].

6.4 CHARACTERISTICS OF FEMTOSECOND-LASER-INDUCED SHOCKWAVES AT AN AIR-WATER INTERFACE

Figure 6.3 shows the evolution of shockwaves induced by loosely-focused femtosecond laser pulses (see experimental setup in Fig. 6.1) in air (top) and water (bottom) at different time delays after the initial passage of the pulse through the air-water interface. The shockwaves in air were generated using pulses with energies and peak on-axis intensities of 2.20 mJ and 1.25×10^{15} W/cm^2, respectively. The Shockwaves in water were generated using pulses with energies and peak on-axis intensities of 2.21 mJ and 1.26×10^{15} W/cm^2, respectively. The images were obtained by very slightly displacing the 5 cm lens, effectively and very slightly defocusing the

Image; in this manner, the phase shifts induced in the 532 nm probe pulse by the pressure differentials in the shockwaves result in light interference and intensity changes at the CCD of the camera. We achieve a magnification of 8.2 at the CCD and a spatial resolution of 1.3 μm.

10 ns after the pump pulse has propagated across the air-water interface, we see the formation of a crater of uniform depth visible just below the water surface, which, at large time scales, develops into the cavity and bubble shown in Figs. 6.2(d) and 6.2(e), respectively. Above the surface, the crater is accompanied by a shockwave in air. After 50 ns, the crater has formed a shockwave in water of planar geometry which propagates away from the surface and becomes visible. Behind the main front can be seen additional shockwaves that propagate from the edges of the crater toward the center and axis of symmetry of the crater. Above the surface, the shockwave in air has separated from a region of heated vapor that is visible in the remainder of the pictures. Notable in the air-shockwave is the presence of a lip directly above the position of the initial generation point, which also corresponds to a region of white light emission (shown in Fig. 6.2(b)) indicative of plasma formation, expansion, and recombination.

At 50 ns, the darker area behind the leading shockwave front can be seen that is confined between the leading and trailing shockwaves and travels with them, corresponding to pressure-induced changes in the refractive index. At 90 ns, the first shock front in water continues to propagate, while the trailing fronts, propagating from the edges of the crater toward the axis of symmetry, cross and begin to form cavitation bubbles.

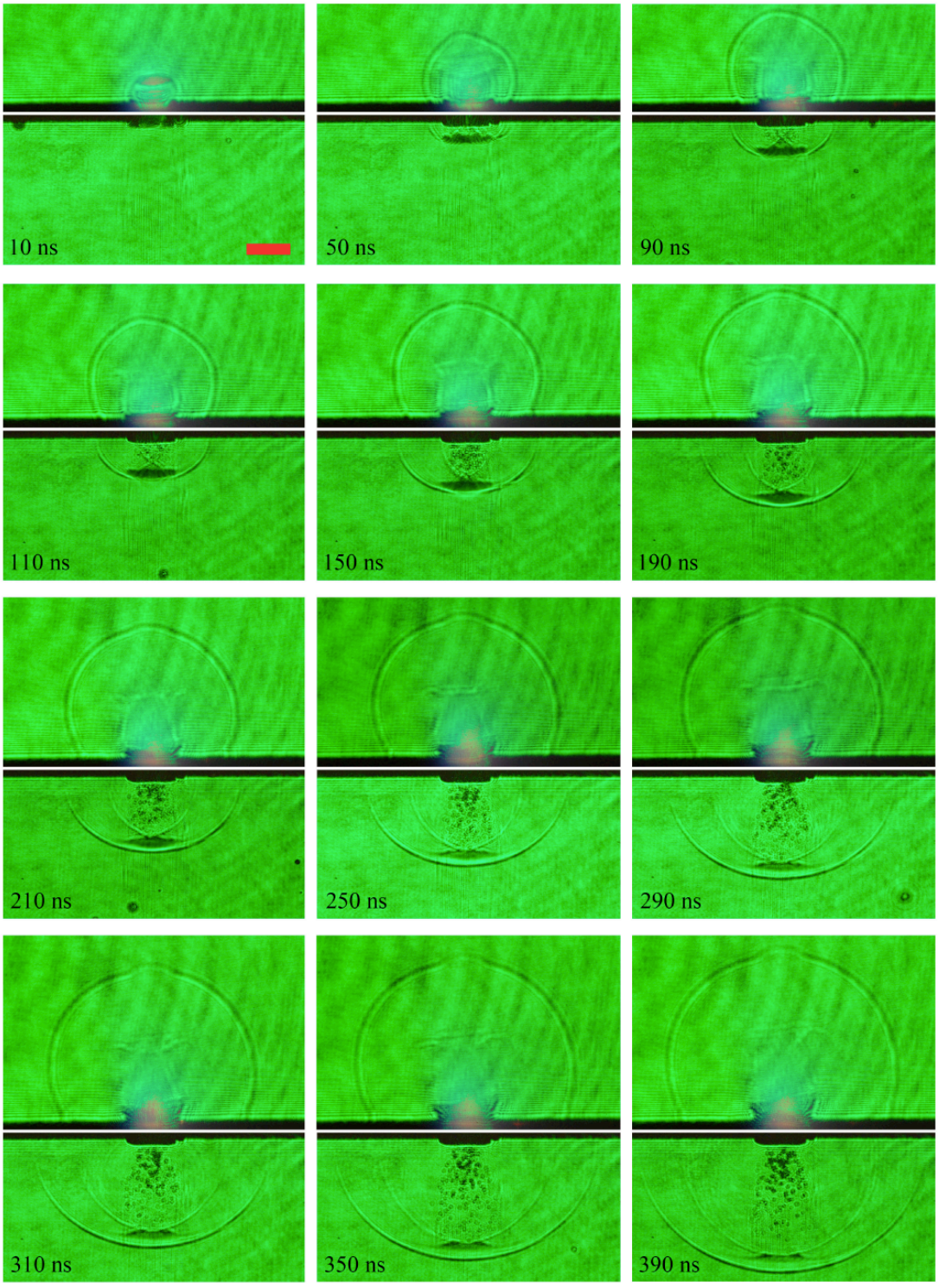

Fig. 6.3 Temporal evolution of shockwaves in air and water using pulses with about 2.2 mJ energy and 1.25×10^{15} W/cm^2 peak on-axis intensity. The red scale bar in the upper left corner is 200 μm in length [12].

This dynamic continues until the trailing shock fronts, having propagated from the edges through the axis of symmetry of the crater, form a roughly hemispherical second shock front behind the first hemispherical shock front.

Above the surface, the air-shockwave continues to propagate, followed by an upward-expanding region of heated vapor. At 90 ns, the beginning of the formation of a crown of liquid around the crater can be observed, which subsequently expands outward from the axis of symmetry.

By pivoting the angle of the tower shown in Fig. 6.1 through an angle θ, we can alter the angle of incidence of the incoming pulse. Figure 6.4 shows the shockwaves generated in water 490 ns after the pulse has propagated through the air-water interface for incidence angles of 0° (Fig. 6.4(a)), 30° (Fig. 6.4(b)), and 45° (Fig. 6.4(c)). The first shock front exhibits a hemispherical shape that is independent of the incident angle of the pump pulse and propagates away from the surface. The second shock front, however, becomes more parabolic in shape and pointed as the angle of incidence is increased. We note that the initial crater visible just below the surface at small times (10 ns)

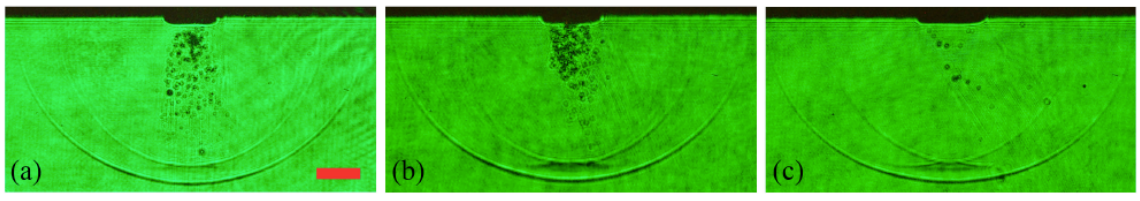

Fig. 6.4 Femtosecond-laser-induced shockwaves in water 490 ns after the pump pulse has propagated through the air-water interface for different angles of incidence: (a) 0°, (b) 30°, (c) 45°. The red scale bar is 200 μm in length. Cavitation bubbles are visible below the crater [12].

after the pump pulse has propagated across the air-water interface has a diameter of 205 ± 3 μm, 228 ± 5 μm, and 287 ± 14 μm for incident angles of 0°, 30°, and 45°, respectively. This behavior follows a simple geometric projection of the form $d = d_0 / \cos\theta$, where d is the diameter of the crater, d_0 is the crater diameter at 0° incidence, and θ is the angle of incidence. The cavitation bubbles tend to form more in the volume irradiated by the laser beam. Also of interest are the most advanced positions of the second shock front, measured from the unperturbed surface position in the region immediately below the crater in Figs. 6.4(a)-6.4(c). These positions are 681 ± 2 μm, 672 ± 2 μm, and 668 ± 2 μm for incident angles of 0°, 30°, and 45°, respectively. These shock front position measurements along the vertical axis form the longer leg of a right triangle, the shorter leg being the crater radius (diameter/2) and the hypotenuse being the distance from the outer edge of the crater to the shock front. The hypotenuse length is an invariant in Figs. 6.4(a)-6.4(c), suggesting the second shock front to be the result of a quasi-linear acoustic superposition of waves propagating from the crater edges.

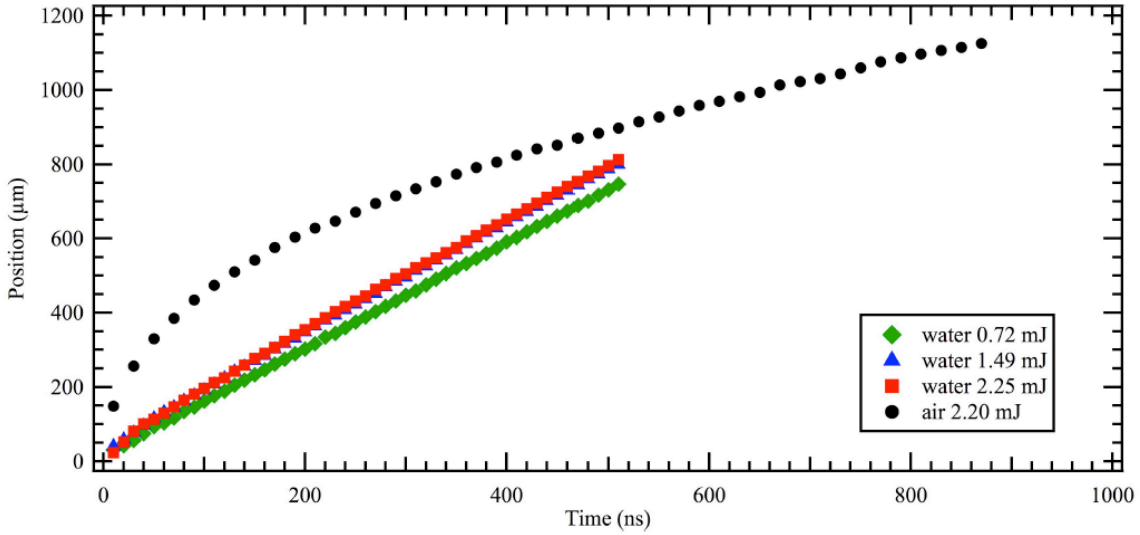

Fig. 6.5 Shock front position as a function of time after the pump pulse has propagated across the air-water interface. The black triangles denote shock front position of shockwaves in air generated by 2.20 mJ pulses. The red squares, blue circles (mostly hidden by the red squares), and green diamonds depict shock front positions generated by pulses with 2.25 mJ, 1.49 mJ, and 0.72 mJ energies [12].

Figure 6.5 shows the position of the most advanced disturbance of the shock front (located directly above and below the crater in the surface for shockwaves in air and water, respectively) as a function of time after the pump pulse has passed; the pulses have an angle of incidence of 0°. Each data point is the average of about 10 measurements, each from a separate image corresponding to the same time delay; the uncertainties are smaller than the data markers. For measurements of shock front position in water, each time step is separated by 10 ns. Measurements were taken of shock fronts generated by pulses of three different energies. In Fig. 6.5, the red squares show the positions of shock fronts generated by pulses with energies of 2.25 mJ and peak on-axis intensities of 1.28×10^{15} W/cm^2. The blue circles (mostly hidden by the red squares) denote positions of shock fronts generated by 1.49 mJ and 8.46×10^{14} W/cm^2

pulses. Finally, the green diamonds mark the positions of shock fronts generated by 0.72 mJ and 4.08×10^{14} W/cm^2 pulses. For water, the shock front position as a function of time after the initial slightly nonlinear portion shows primarily linear behavior, indicating that the shockwave is weak and propagates as a plane wave, not experiencing divergence and noticeable reduction of amplitude at considered distances. We fit the linear portion of the curves (corresponding to time delays of 70 ns and above) with an uncertainty-weighted algorithm to yield the shock front velocities. This procedure yields shock front velocities of 1511 ± 2 m/s, 1491 ± 2 m/s, and 1428 ± 2 m/s for pulse energies of 2.25 mJ, 1.49 mJ, and 0.72 mJ, respectively (see the first paragraph of Section 6.5 for a discussion of these velocity values). According to weak shock theory for underwater shockwaves in a liquid [143], the shock front velocity c_s is

$$c_s = c_0 + \beta u / 2 \ , \tag{6.1}$$

where c_0 is the speed of sound (propagation speed for small-amplitude acoustic waves) with a value of 1494 m/s at 24° C [144], β is the nonlinearity of the liquid (with a value of 3.5 at 20° C in distilled water [145]), and u is the particle velocity. For weak shock waves, the linear impedance relation

$$p = \rho_0 c_0 u \ , \tag{6.2}$$

where p is the pressure and ρ_0 is the density of water, is applicable. Substituting Eq. 6.2 into Eq. 6.1 and solving for the pressure yields for a measured shock front velocity c_s of 1511 m/s (see above) a pressure of 14.5 MPa. Time steps for measurements of shock front position in air were 20 ns; pulse energies and intensities were 2.20 mJ and 1.25×10^{15} W/cm^2, respectively. The shape of the curve representing shock front

position as a function of time indicates that the shockwave in air is a strong shockwave. In order to calculate a lower bound on the initial peak pressure, we use the distance traveled by the shock wave between the first two data points, which is 108 ± 8 μm. Since the data points are separated by 20 ns, this yields a shock front velocity c_s of 5400 ± 400 m/s. Utilizing an approach similar to [131], we calculate the peak pressure through the Rankine-Hugoniot expression for air:

$$\frac{P}{P_0} = \frac{7}{6}\left[\left(\frac{c_s}{c_0}\right)^2 - 1\right], \tag{6.3}$$

where c_0 is the speed of sound in air (344 m/s in air at 20° C [146]), and P_0 is the undisturbed air pressure (101 kPa). This yields a lower limit for the initial peak pressure of 29 MPa.

Figure 6.6 shows the measured positions of the first and second shock fronts 490 ns after the pump pulse has passed as a function of the pulse energy and peak on-axis intensity. The first shock front is denoted by black circles, while the second shock front is denoted by black triangles; each data point is an average of the measurements of about 10 separate images. The uncertainties in the figure are the size of the data markers. Above a pulse energy and peak on-axis intensity of 1.03 mJ and 5.83×10^{14} W/cm^2, respectively, the shock front positions after 490 ns remain almost independent of pulse energy, i.e. constant. This indicates that there is no significant increase in shockwave peak pressure with increasing pulse energy. It is possible that there may be some shielding effect as pulse energy is increased [147]. Below this threshold energy and peak on-axis intensity value, however, the first and second shock fronts converge with

reducing pulse energy until they form a single shock front at a pulse energy and intensity of 0.55 mJ and 3.13×10^{14} W/cm, respectively. This may be due to the fact that the width of the crater just below the surface also decreases below this threshold value, finally becoming unobservable below a pulse energy of 0.55 mJ. Below pulse energies of 0.55 mJ, no shock fronts were detected with our experimental setup. The red line in Fig. 6.6, corresponding to a pulse energy of 1.03 mJ, indicates the energy and intensity value below which no light emission from plasma is observed (see Fig. 6.2(b)). This corresponds to the threshold value of pulse energy and intensity below which the first and second shock fronts begin to converge into a single front. A pulse energy of 0.55 mJ may correspond with an ablation threshold for strong evaporation, while a pulse energy of 1.03 mJ may correspond to dielectric breakdown [58,148]. However, more rigorous study of this question is beyond the scope of this dissertation.

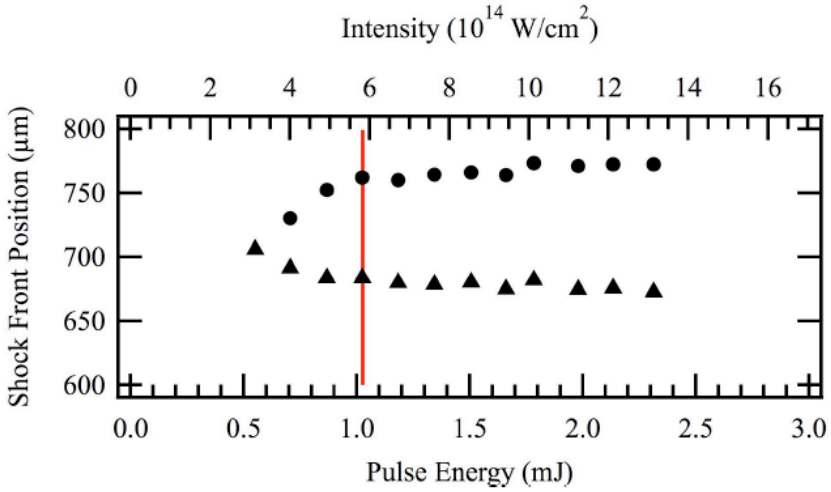

Fig. 6.6 Measured positions at 490 ns of the first (black circles) and second (black triangles) shock fronts as a function of pulse energy and peak on-axis intensity. The red line indicates the pulse energy value below which no light emission from plasma formation is observed (see Fig. 6.2(b)). Also below this energy the width of the crater just below the surface decreases [12].

6.5 ANALYSIS OF SHOCKWAVE STRENGTH AND POSSIBLE APPLICATIONS

We point out that, in Fig. 6.5, the curve corresponding to the shock front position as a function of time for pump pulses with energies of 0.72 mJ yields a shock front velocity of 1428 m/s, which is slower than the observed velocity of sound in water of 1494 m/s at a room temperature of 24° C [144]. This discrepancy is most likely a systematic error resulting from the slight defocusing of the 5 cm imaging lens shown in Fig. 6.1. After a slight defocusing, the object plane no longer contains the axis of symmetry of the crater formed beneath the surface; since we image a two-dimensional slice of a three dimensional shock front, measurements of shock front position are slightly less than the actual values. A sound velocity of 1428 m/s is within 4.5% of the accepted value. Since the generated shockwaves are weak (as evidenced by the linear behavior of the shock front position as a function of time), it is reasonable to conclude that the shock front generated by pulses with 0.72 mJ energy propagates with a velocity very close to the speed of sound. It is therefore reasonable to conclude that the measured quantities retrieved from our images are systematically 4% to 5% less than their actual values. The qualitative and comparative relationships within and between data sets, however, remain accurate.

The shockwaves we have documented are generated at the air-water interface at or just below the surface. The data in Fig. 6.3 show that the shockwaves originate from a crater that is already clearly visible 10 ns after the pump pulse has propagated across the interface. Moreover, the fact that the first shock front remains independent of the

incident angle of pulse as shown in Fig. 6.4 further supports the conclusion that the shockwaves are inherently due to a surface effect which involves the crater. The origin of the crater is most likely optical breakdown at the surface accompanied by ablation and spallation as a result of dense plasma formation and subsequent expansion into the air above the surface [149]. Since the ablation layer (crater) is of the same thickness across the laser beam cross-section, one can conclude that the transfer of the energy to the liquid should be limited after reaching some threshold. The creation of free electrons leads to a reduction of the refractive index n [63]. Thus, when the concentration of electrons reaches some critical value, $n < 0$ and the laser radiation is reflected. In our experiment, the plasma densities may begin to approach this value. Our pulse intensity is high enough to ionize the medium and result in the formation of a dense plasma. Strong dissociation of water can also be expected [150,151]. After ionization, electrons experience oscillating motion in the field of the laser pulse and acquire ponderomotive energy on the order of tens of eV for the laser pulse energies used. The interaction process results in significant deposition of the laser pulse energy in the water surface layer. The hot electron gas exchanges energy with ions and molecules, which results in a high temperature and pressure of the medium in the interaction region. Thus, on this same time scale a strongly nonequilibrium state of an overheated and ionized gas is produced. Subsequently, thermalization, expansion, and cooling down of this plasma occurs, which takes place on the ps-ns time scale. The abruptly produced high pressure pushes the liquid, giving rise to a shock wave in liquid; on the other side it pushes also the gaseous air, forming a shock wave in the air. In view of the much larger density of

the liquid, the overheated layer mostly expands above the water surface, forming an evaporation plume. The generation mechanism in water is thus an abrupt pressure increase in the layer of the energy deposition and recoil momentum due to ablation. This picture is supported by the results of Sarpe-Tudoran *et al.* in [128]. In this work, they observed the electron density at a water surface irradiated by powerful femtosecond laser pulses to be 1.2×10^{21} cm^{-3}. They subsequently observed a 20 ps time delay before plasma expansion at a velocity of 5900 m/s. This is consistent with our observations of the shockwave in air after just 10 ns as well as light emission in the region immediately above the crater as shown in Fig. 6.2(b). Such light emission is consistent with plasma excitation and recombination. It is also consistent with the continuum emission spectrum well-known in laser induced breakdown spectroscopy (LIBS). LIBS analysis of water has been carried out for many years using nanosecond laser pulses in various experimental configurations (see [152] for a well-referenced review of these techniques). Recently, the mineral composition of seawater has been analyzed using femtosecond LIBS in a time-gated technique [153], where the light emission was observed for time intervals greater than one nanosecond, corresponding to similar durations of the recombination process and plasma lifetime. Our work supports the utility of femtosecond laser pulses in remotely analyzing water samples based upon dielectric breakdown and plasma formation at a water surface.

Our work also supports the feasibility of remote thrust generation based upon liquid ablation by femtosecond laser pulses [154,155]. Several works have documented the effects of explosive evaporation at a water surface due to resonant heat deposition

using picosecond and nanosecond laser pulses (see [156] for well-referenced review of these works). These works, however, used light wavelengths in the mid-infrared corresponding to resonances in the water absorption spectrum. Our own pulses, which have a central wavelength of 800 nm, are not centered on a resonance. Nevertheless, the deposition of energy in the liquid is efficient and almost instantaneous due to production of dense plasma. However, this energy deposition can be limited by the screening effect when plasma density exceeds some critical value.

Such an instantaneous planar excitation has significant advantages. On distances smaller than the diffraction length, the leading shockwave front is a plane wave. With propagation distance, it experiences divergence and transforms itself into an expanding hemisphere at larger distances. The observed images of the two tailing wave fronts can be understood from linear sound generation. When a disk-like and almost instantaneous sound source is produced at the surface, the propagating plane wave front of higher pressure arrives first. The wave of high pressure lasts until the sound from the edges of the disk comes to the observation point. This latter corresponds to the tailing front of the pressure wave passing the observation point, and this front has the shape of an expanding half-toroid with its center line coinciding with the edge of the source disk. The change in shape of the second wave front as a function of pulse incident angle as shown in Fig. 6.4 can also be understood within this framework as was discussed above in Section 6.4.

As our results show, a loosely-focused femtosecond laser pulse incident upon an air-water interface produces highly reproducible sound waves capable of being linearly

superimposed upon one another. When multiple pulses are used, synchronized in both time and space, they can produce arrays of sound sources, generating tailored and directionally-controllable acoustic wave fronts. It may even be possible to remotely control a single sound source and subsequent shockwave propagation direction by exploring the pulse parameters such as spatial intensity distribution (beam mode and beam shaping) and pulse chirp.

The conversion of pulsed laser radiation into acoustic energy has been shown to be more efficient at the intensities corresponding to reaching the optical breakdown threshold [157,158]. For femtosecond radiation, the interaction with the medium is so fast and ablation is so efficient that no significant heating of the remaining matter occurs. For the same reason, no significant residual stresses are left in the material, and therefore this channel of laser pulse energy distribution (losses) is not so essential for femtosecond as it is for longer pulses. Femtosecond laser pulses therefore offer unique potential for precise control of acoustic waves. Such control may be of practical interest for acoustic generation within tissues; although it has been shown that nanosecond-laser-induced dielectric breakdown results in qualitatively different responses for water and tissue, with compressive acoustic waves in water and compressive/tensile waves in tissue [159], the possibility for precise control using femtosecond-laser-induced acoustic waves at a surface may be of interest for further research and applications in this area. These properties of femtosecond laser pulses are also important for use in remote sensing applications in oceanic and riverine environments.

6.6 SUMMARY OF EXPERIMENT AND CONCLUSIONS

We have reported the generation of femtosecond-laser-induced shockwaves at an air-water interface using loosely focused millijoule laser pulses. We have reported the phenomenological context in which the shockwaves are generated as well as the characteristics and generating mechanisms of said shockwaves. We point out that interaction of femtosecond laser pulses with aquatic surfaces may be used to remotely characterize the chemical and mineral composition of waters in oceanic and riverine environments through spectral analysis of the laser-induced breakdown spectroscopy (LIBS) signal generated by the plasma at the water surface. We observed, with femtosecond surface optical breakdown, the generation of weak shockwaves in water and their quasi-linear superposition. Thus, remote control of sound wave pulse shape and propagation direction by superposition of waves produced from spatially and temporally synchronized femtosecond laser pulses interacting with a liquid surface is a feasible possibility. Our results can also be of interest for medical applications dealing with tissue ablation by femtosecond laser pulses and for remote acoustic applications in oceanic and riverine environments.

CHAPTER VII

CONCLUSIONS

The primary conclusion of this dissertation is that millijoule femtosecond laser pulses incident upon an air-water interface have potential applications in remote sensing in marine environments, including remote detection of the physical and chemical properties of a body of water via LIBS spectroscopy as well advanced acoustic signal generation and detection through ablation of the water at the surface. The physical phenomena that occur at the air-water interface include linear and nonlinear optical phenomena: refraction, reflection, linear dispersion, self-focusing, ionization and subsequent defocusing, spectral broadening, laser-induced breakdown, and laser-induced ablation. These phenomena have been investigated in the previous chapters:

In Chapter II we discussed linear optics and investigated how an ultrashort laser pulse propagates through water [8].

In Chapter III we discussed nonlinear optics and investigated the onset of nonlinear optical pulse propagation in water [9].

In Chapter IV we discussed the basic properties and mechanisms of femtosecond laser filaments and investigated energy transfer between two intersecting filaments in liquid methanol [10].

In Chapter V we discussed laser-induced ablation of materials and laser-induced breakdown spectroscopy (LIBS). We then demonstrated that different breakdown thresholds of materials can be exploited in order to image shallowly buried objects via

analysis of the LIBS signal [11].

In Chapter VI we brought all of the preceding phenomena together in order to investigate the interaction of millijoule femtosecond laser pulses with an air-water interface [12]. We demonstrated that many potential applications might be implemented toward remote sensing in marine environments, as mentioned above. As such, this dissertation may serve as a springboard for further investigations into the many potential applications that may be developed for remote sensing in marine environments.

REFERENCES

[1] K. Stelmaszczyk, P. Rohwetter, G. Mejean, J. Yu, E. Salmon, J. Kasparian, R. Ackermann, J.-P. Wolf, and L. Woste, Appl. Phys. Lett. **85**, 3977 (2004).

[2] P. Rohwetter, K. Stelmasczyk, L. Woste, R. Ackermann, G. Mejean, E. Salmon, J. Kasparian, J. Yu, and J.-P. Wolf, Spectrochim. Acta B **60**, 1025 (2005).

[3] W. Liu, H. L. Xu, G. Mejean, Y. Kamali, J.-F. Daigle, A. Azarm, P. T. Simard, P. Mathieu, G. Roy, and S. L. Chin, Spectrochim. Acta B **62**, 76 (2007).

[4] H. L. Xu, G. Mejean, W. Liu, Y. Kamali, J.-F. Daigle, A. Azarm, P. T. Simard, P. Mathieu, G. Roy, J.-R. Simard, and S. L. Chin, Appl. Phys. B **87**, 151 (2009).

[5] P. Hemmer, R. B. Miles, P. Polynkin, T. Siebert, A. V. Sokolov, P. Sprangle, and M. O. Scully, Proc. Natl. Acad. Sci. USA **108**, 3130 (2011).

[6] R. R. Musin, M. N. Shneider, A. M. Zheltikov, and R. B. Miles, Appl. Opt. **46**, 5593 (2007).

[7] M. N. Shneider, A. M. Zheltikov, and R. B. Miles, J. Appl. Phys. **108**, 033113 (2010).

[8] L. M. Naveira, B. D. Strycker, J. Wang, G. O. Ariunbold, A. V. Sokolov, and G. W. Kattawar, Appl. Opt. **48**, 1828 (2009).

[9] A. V. Sokolov, L. M. Naveira, M. P. Poudel, J. Strohaber, C. S. Trendafilova, W. C. Buck, J. Wang, B. D. Strycker, C. Wang, H. Schuessler, A. Kolomenskii, and G. W. Kattawar, Appl. Opt. **49**, 513 (2010).

[10] B. D. Strycker, M. Springer, C. Trendafilova, X. Hua, M. Zhi, A. A. Kolomenskii, H. Schroeder, J. Strohaber, H. A. Schuessler, G. W. Kattawar, and A. V. Sokolov, Opt. Lett. **37**, 16 (2012).

[11] B. D. Strycker, K. Wang, M. Springer, and A. V. Sokolov, Appl. Opt. **52**, 4792 (2013).

[12] B. D. Strycker, M. M. Springer, A. J. Traverso, A. A. Kolomenskii, G. W. Kattawar, and A. V. Sokolov, Optics Express (n.d.).

[13] K. E. Oughstun, *Electromagnetic and Optical Pulse Propagation 1* (Springer, New York, 2006).

[14] H. A. Lorentz, *The Theory of Electrons*, 2nd ed. (Teubner, Leipzig, 1916).

[15] K. E. Oughstun and N. A. Cartwright, Optics Express **11**, 1541 (2003).

[16] J. F. James, *A Student's Guide to Fourier Transforms*, 3rd ed. (Cambridge University Press, Cambridge, 2011).

[17] M. O. Scully and M. S. Zubairy, *Quantum Optics* (Cambridge University Press, Cambridge, 1997).

[18] R. W. Boyd, *Nonlinear Optics*, 3rd ed. (Academic Press, USA, 2008).

[19] E. Merzbacher, *Quantum Mechanics*, 3rd ed. (John Wiley & Sons, Inc., USA, 1998).

[20] Y. Marechal, *The Hydrogen Bond and the Water Molecule* (Elsevier, Italy, 2007).

[21] P. D. T. Huibers, Appl. Opt. **36**, 3785 (1997).

[22] D. J. Segelstein, *The Complex Refractive Index of Water* , Master's Thesis, (University of Missouri-- Kansas City, 1981).

[23] L. Kou, D. Labrie, and P. Chylek, Appl. Opt. **32**, 3551 (1993).

[24] R. M. Pope and E. S. Fry, Appl. Opt. **36**, 8710 (1997).

[25] E. S. Fry, G. W. Kattawar, and R. M. Pope, Appl. Opt. **31**, 2055 (1992).

[26] J.-C. Diels and W. Rudolph, *Ultrashort Laser Pulse Phenomena*, 2nd ed. (Academic Press, USA, 2006).

[27] A. M. Weiner, *Ultrafast Optics* (Wiley, USA, 2009).

[28] L. Brillouin, *Wave Propagation and Group Velocity* (Academic Press, New York, 1960).

[29] K. E. Oughstun and G. C. Sherman, J. Opt. Soc. Am. B **5**, 817 (1988).

[30] S. H. Choi and U. Österberg, Phys. Rev. Lett. **92**, 193903 (2004).

[31] R. R. Alfano, J. L. Birman, X. Ni, M. Alrubaiee, and B. B. Das, Phys. Rev. Lett. **94**, 239401 (2005).

[32] T. M. Roberts, Phys. Rev. Lett. **93**, 269401 (2004).

[33] A. E. Fox and U. Österberg, Optics Express **14**, 3688 (2006).

[34] U. J. Gibson and U. L. Österberg, Optics Express **13**, 2105 (2005).

[35] J. C. Li, D. R. Alexander, H. F. Zhang, U. P. Parali, D. W. Doerr, J. C. Bruce III, and H. Wang, Optics Express **15**, 1939 (2007).

[36] Y. Okawachi, A. D. Slepkov, I. H. Agha, D. F. Geraghty, and A. L. Gaeta, J. Opt. Soc. Am. A **24**, 3343 (2007).

[37] A. Owyoung, *The Origins of the Nonlinear Refractive Indices of Liquids and Glasses*, Thesis, (California Institute of Technology, 1971).

[38] G. P. Agrawal, *Nonlinear Fiber Optics*, 4th ed. (Academic Press, USA, 2007).

[39] D. Anderson and M. Lisak, Phys. Rev. A **27**, 1393 (1983).

[40] M. C. Fischer, H. C. Liu, I. R. Piletic, and W. S. Warren, Optics Express **16**, 4192 (2008).

[41] N. Tcherniega, A. Sokolovskaia, A. D. Kudriavtseva, R. Barille, and G. Rivoire, Opt. Commun. **181**, 197 (2000).

[42] A. Brodeur and S. L. Chin, Phys. Rev. Lett. **80**, 4406 (1998).

[43] M. Koselik, G. Katona, J. V. Moloney, and E. M. Wright, Appl. Phys. B **77**, 185 (2003).

[44] S. L. Chin, *Femtosecond Laser Filamentation* (Springer, New York, 2010).

[45] J. H. Marburger, Prog. Quant. Electr. **4**, 35 (1975).

[46] R. W. Boyd, S. G. Lukishova, and Y. R. Shen, *Self-focusing: Past and Present* (Springer, New York, 2009).

[47] J. W. Goodman, *Introduction to Fourier Optics*, 3rd ed. (Roberts and Company Publishers, USA, 2005).

[48] L. V. Keldysh, JETP **20**, 1307 (1965).

[49] S. L. Chin and P. Lambropoulos, *Multiphoton Ionization of Atoms* (Academic Press, USA, 1984).

[50] N. B. Delone and V. P. Krainov, *Multiphoton Processes in Atoms*, 2nd ed. (Springer, Heidelberg, 2000).

[51] A. Dubietis, A. Couairon, E. Kucinskas, G. Tamosauskas, E. Gaizauskas, D. Faccio, and P. Di Trapani, Appl. Phys. B. **84**, 439 (2006).

[52] V. S. Popov, Physics--Uspekhi **47**, 855 (2004).

[53] M. Abramowitz and I. A. Stegun, *Handbook of Mathematical Functions with Formulas, Graphs, and Mathematical Tables* (Dover Publ., USA, 1965).

[54] S. L. Chin, in *Advances in Multi-Photon Processes and Spectroscopy*, edited by S. H. Lin, A. A. Villaeys, and Y. Fujimura (World Scientific, Singapore, 2011), pp. 249–271.

[55] N. Bloembergen, IEEE J. Quant. Elect. **QE-10**, 375 (1974).

[56] P. K. Kennedy, IEEE J. Quant. Elect. **31**, 2241 (1995).

[57] E. Yablonovitch and N. Bloembergen, Phys. Rev. Lett. **29**, 907 (1972).

[58] D. M. Rayner, A. Naumov, and P. B. Corkum, Optics Express **13**, 3208 (2005).

[59] X. M. Zhao, J.-C. Diels, C. Y. Wang, and J. M. Elizondo, IEEE J. Quant. Elect. **31**, 599 (1995).

[60] S. Tzortzakis, B. Prade, M. Franco, and A. Mysyrowicz, Opt. Commun. **181**, 123 (2000).

[61] M. Born and E. Wolf, *Principles of Optics*, 5th ed. (Pergamon Press, Oxford, 1975).

[62] T. P. Hughes, *Plasma and Laser Light* (John Wiley & Sons, Inc., USA, 1975).

[63] C. Sarpe, J. Köhler, T. Winkler, M. Wollenhaupt, and T. Baumert, New J. Phys. **14**, 075021 (2012).

[64] V. L. Ginzburg, *The Propagation of Electromagnetic Waves in Plasmas* (Pergamon Press, Oxford, 1964).

[65] V. Loriot, E. Hertz, O. Faucher, and B. Lavorel, Optics Express **17**, 13429 (2009).

[66] P. Bejot, J. Kasparian, S. Henin, V. Loriot, T. Vieillard, E. Hertz, O. Faucher, B. Lavorel, and J.-P. Wolf, Phys. Rev. Lett. **104**, 103903 (2010).

[67] P. Polynkin, M. Kolesik, E. M. Wright, and J. V. Moloney, Phys. Rev. Lett. **106**, 153902 (2011).

[68] A. C. Bernstein, M. McCormick, G. M. Dyer, J. C. Sanders, and T. Ditmire, Phys. Rev. Lett. **102**, 123902 (2009).

[69] Y. Lui, M. Durand, S. Chen, A. Houard, B. Prade, B. Forestier, and A. Mysyrowicz, Phys. Rev. Lett. **105**, 055003 (2010).

[70] J. Kasparian, M. Rodriguez, G. Mejean, J. Yu, E. Salmon, H. Wille, R. Bourayou, S. Frey, Y.-B. Andre, R. Mysyrowicz, R. Sauerbrey, J.-P. Wolf, and L. Woste, Science **301**, 61 (2003).

[71] G. Mechain, C. D'Amico, Y.-B. Andre, S. Tzortzakis, M. Franco, B. Prade, A. Mysyrowicz, A. Couairon, E. Salmon, and R. Sauerbrey, Opt. Commun. **247**, 171 (2005).

[72] M. Y. Shverdin, S. N. Goda, G. Y. Yin, and S. E. Harris, Opt. Lett. **31**, 1331 (2006).

[73] G. Fibich, Y. Sivan, Y. Erlich, E. Louzon, M. Fraenkel, S. Eisenmann, Y. Katzir, and A. Zigler, Optics Express **14**, 4946 (2006).

[74] W. Liu, F. Theberge, J.-F. Daigle, P. T. Simard, S. M. Safiri, Y. Kamali, H. L. Xu, and S. L. Chin, Appl. Phys. B. **85**, 55 (2006).

[75] J.-F. Daigle, Y. Kamali, M. Chateauneuf, G. Tremblay, F. Theberge, J. Dubois, G. Roy, and S. L. Chin, Appl. Phys. B. **97**, 701 (2009).

[76] H. Schroeder and S. L. Chin, Opt. Commun. **234**, 399 (2004).

[77] M. Segev and G. Stegeman, Phys. Today **51**, 42 (1998).

[78] N. Akhmediev and A. Ankiewicz, Opt. Commun. **100**, 186 (1993).

[79] J. P. Singh and S. N. Thakur, editors, *Laser-Induced Breakdown Spectroscopy* (Elsevier, 2007).

[80] T. G. Graff, R. V. Morris, S. M. Clegg, R. C. Wiens, and R. B. Anderson, 42nd Lunar Planetary Science Conference 1916 (2011).

[81] N. Melikechi, R. Wiens, H. Newsom, and S. Maurice, Opt. Photonics News **24**, 26 (2013).

[82] D. A. Cremers and L. J. Radziemski, *Handbook of Laser-induced Breakdown Spectroscopy* (Wiley, Great Britain, 2006).

[83] H. M. Jol, *Ground Penetrating Radar* (Elsevier, Slovenia, 2009).

[84] C. S. Bristow and H. M. Jol, *Ground Penetrating Radar in Sediments* (Geological Society, United Kingdom, 2003).

[85] J. MacDonald, J. R. Lockwood, J. McFee, T. Altschuler, T. Broach, L. Carin, R. Harmon, C. Rappaport, W. Scott, and R. Weaver, *Alternatives for Landmine Detection* (Rand, Santa Monica, CA, 2003).

[86] F. Anabitarte, A. Cobo, and J. M. Lopez-Higuera, ISRN Spectrosc. **2012**, 1 (2012).

[87] D. W. Hahn and N. Omenetto, Appl. Spectrosc. **64**, 335A (2010).

[88] R. Gronlund, M. Lundqvist, and S. Svanberg, Opt. Lett. **30**, 2882 (2005).

[89] K. Wang, B. D. Strycker, D. V. Voronine, P. K. Jha, M. O. Scully, R. E. Meyers, P. Hemmer, and A. V. Sokolov, Opt. Lett. **37**, 1343 (2012).

[90] R. S. Harmon, F. C. DeLucia, Jr., A. LaPointe, R. J. Winkel, Jr., and A. W. Miziolek, Anal. Bioanal. Chem. **385**, 1140 (2006).

[91] L. B. Stotts, J. Opt. Soc. Am. **67**, 815 (1977).

[92] H. C. van de Hulst and G. W. Kattawar, Appl. Opt. **33**, 5820 (1994).

[93] G. A. D'Almeida, J. Geophys. Res. **92**, 3017 (1987).

[94] J. Chen, J. Ng, and C. T. Chan, Nat. Photonics **5**, 531 (2011).

[95] A. Novitsky, C. W. Qui, and H. Wang, Phys. Rev. Lett. **107**, 203601 (2011).

[96] G. A. Askar'yan, A. M. Prokhorov, G. F. Chanturiya, and G. P. Shipulo, JETP **17**, 1463 (1963).

[97] R. G. Brewer and K. E. Rieckhoff, Phys. Rev. Lett. **13**, 334 (1964).

[98] F. V. Bunkin and V. M. Komissarov, Sov. Phys. Acoust. **19**, 203 (1973).

[99] F. V. Bunkin and M. I. Tribel'skii, Sov. Phys. Usp. **23**, 105 (1980).

[100] L. M. Lyamshev and K. A. Naugol'nykh, Sov. Phys. Acoust. **27**, 357 (1981).

[101] L. M. Lyamshev, Sov. Phys. Usp. **30**, 252 (1987).

[102] B. S. Maccabee, IEEE 1987 Ultrasonics Symposium 1099 (1987).

[103] F. V. Bunkin, A. A. Kolomensky, and V. G. Mikhalevich, *Lasers in Acoustics* (Harwood Academic Publishers, Switzerland, 1991).

[104] V. E. Gusev and A. A. Karabutov, *Laser Optoacoustics* (AIP Press, New York, 1993).

[105] J. Noack and A. Vogel, Proc. SPIE **2391**, (1995).

[106] A. Vogel, S. Busch, and U. Parlitz, J. Acoust. Soc. Am. **100**, 148 (1996).

[107] J. Noack and A. Vogel, Appl. Opt. **37**, 4092 (1998).

[108] E. Abraham, K. Minoshima, and H. Matsumoto, Opt. Comm. **176**, 441 (2000).

[109] C. B. Schaffer, N. Nishimura, E. N. Glezer, A. M.-T. Kim, and E. Mazur, Optics Express **10**, 196 (2002).

[110] E. N. Glezer and E. Mazur, Appl. Phys. Lett. **71**, 882 (1997).

[111] E. N. Glezer, C. B. Schaffer, N. Nishimura, and E. Mazur, Opt. Lett. **22**, 1817 (1997).

[112] R. Petkovsek, J. Mozina, and G. Mocnik, Optics Express **13**, 4107 (2005).

[113] A. Takita and Y. Hayasaki, Proc. SPIE **7201**, 72010J (2009).

[114] A. Takita and Y. Hayasaki, Jpn. J. Appl. Phys. **48**, 09LD04 (2009).

[115] A. Vogel, N. Linz, S. Freidank, and G. Paltauf, Phys. Rev. Lett. **100**, 038102 (2008).

[116] A. Vogel, J. Noack, G. Huttman, and G. Paltauf, Appl. Phys. B **81**, 1015 (2005).

[117] W. Lauterborn and A. Vogel, in *Bubble Dynamics & Shock Waves*, edited by C. F. Delale (Springer-Verlag, New York, 2013), pp. 67–103.

[118] A. Lindinger, J. Hagen, L. D. Socaciu, T. M. Bernhardt, L. Woste, D. Duft, and T. Leisner, Appl. Opt. **43**, 5263 (2004).

[119] A. A. Zemlyanov, Y. E. Geints, and D. V. Apeksimov, Proc. of SPIE **6160**, 61601G (2006).

[120] C. Favre, V. Boutou, S. C. Hill, W. Zimmer, M. Krenz, H. Lambrecht, J. Yu, R. K. Chang, L. Woeste, and J.-P. Wolf, Phys. Rev. Lett. **89**, 035002 (2002).

[121] F. Courvoisier, V. Boutou, C. Favre, S. C. Hill, and J.-P. Wolf, Opt. Lett. **28**, 206 (2003).

[122] F. Courvoisier, V. Boutou, J. Kasparian, E. Salmon, G. Mejean, J. Yu, and J.-P. Wolf, Appl. Phys. Lett. **83**, 213 (2003).

[123] A. Flettner, T. Pfeifer, D. Walter, C. Winterfeldt, C. Spielmann, and G. Gerber, Appl. Phys. B **77**, 747 (2003).

[124] P. Rohwetter, K. Stelmasczyk, M. Queisser, M. Fechner, and L. Woste, Opt. Comm. **281**, 797 (2008).

[125] Y. Q. Liu, J. Zhang, Z. M. Sheng, X. Y. Peng, and Z. Jin, Opt. Comm. **281**, 1244 (2008).

[126] Y. E. Geints, A. M. Kabanov, G. G. Matvienko, V. K. Oshlakov, A. A. Zemlyanov, S. S. Golik, and O. A. Bukin, Opt. Lett. **35**, 2717 (2010).

[127] Y. E. Geints, A. A. Zemlyanov, A. M. Kabanov, E. E. Bykova, D. V. Apeksimov, O. A. Bukin, E. B. Sokolova, S. S. Golik, and A. A. Ilyin, Appl. Opt. **50**, 5291 (2011).

[128] C. Sarpe-Tudoran, A. Assion, M. Wollenhaupt, M. Winter, and T. Baumert, Appl. Phys. Lett. **88**, 261109 (2006).

[129] M. Anija and R. Philip, Opt. Comm. **282**, 3770 (2009).

[130] F. V. Bunkin, N. V. Karlov, V. M. Komissarov, and G. P. Kuz'min, ZhETF Pis. Red. **13**, 479 (1971).

[131] C. E. Bell and B. S. Maccabee, Appl. Opt. **13**, 605 (1974).

[132] D. C. Emmony, Appl. Phys. Lett. **29**, 547 (1976).

[133] D. C. Emmony, B. M. Geerken, and A. Straaijer, Infrared Phys. **16**, 87 (1976).

[134] G. V. Ostrovskaya and E. V. Shedova, Izv. Akad. Nauk, Ser. Fiz. **61**, 1342 (1997).

[135] G. V. Ostrovskaya, I. I. Komissarova, V. N. Philippov, and E. N. Shedova, Proc. SPIE **3093**, 146 (1997).

[136] A. O. Bukin, I. G. Nagorniv, F. P. Yarovenko, S. S. Golik, V. I. Tsarev, and A. N. Pavlov, in (2004), p. 146.

[137] J. Sinko, L. Kodgis, S. Porter, J. Lin, A. V. Pakhomov, C. W. Larson, and F. B. Mead, Jr., Proc. of SPIE **6261**, 62611W (2006).

[138] S. T. Thoroddsen, K. Takehara, T. G. Etoh, and C.-D. Ohl, Phys. Fluids **21**, 112101 (2009).

[139] D. Jang, J.-G. Park, and D. Kim, J. Appl. Phys. **109**, 073101 (2011).

[140] K. Ando, A. Q. Liu, and Ohl, in (Seattle, 2011).

[141] R. C. C. Chen, Y. T. Yu, K. W. Su, J. F. Chen, and Y. F. Chen, Optics Express **21**, 445 (2013).

[142] S. V. Oshemkov, L. P. Dvorkin, and V. Y. Dmitriev, Tech. Phys. Lett. **34**, 408 (2008).

[143] P. H. Rogers, J. Acoust. Soc. Am. **62**, 1412 (1977).

[144] M. Greenspan and C. E. Tschiegg, J. Acoust. Soc. Am. **31**, 75 (1959).

[145] M. F. Hamilton and D. T. Blackstock, *Nonlinear Acoustics* (Academic Press, USA, 1998).

[146] A. J. Zuckerwar, *Handbook of the Speed of Sound in Real Gases* (Elsevier, USA, 2002).

[147] D. X. Hammer, E. D. Jansen, M. Frenz, G. D. Noojin, R. J. Thomas, J. Noack, A. Vogel, B. A. Rockwell, and A. J. Welch, Appl. Opt. **36**, 5630 (1997).

[148] C. H. Fan, J. Sun, and J. P. Longtin, J. Appl. Phys. **91**, 2530 (2002).

[149] M. B. Agranat, S. I. Anisimov, S. I. Ashitkov, V. V. Zhakhovskii, N. A. Inogamov, K. Nishihara, Y. V. Petrov, V. E. Fortov, and V. A. Khokhlov, Appl. Surf. Sci. **253**, 6276 (2007).

[150] S. L. Chin and S. Lagace, Appl. Opt. **35**, 907 (1996).

[151] G. Maatz, A. Heisterkamp, H. Lubatschowski, S. Barcikowski, C. Fallnich, H. Welling, and W. Ertmer, J. Opt. A: Pure Appl. Opt. **2**, 59 (2000).

[152] A. S. Alsulmi, Water Analysis by Laser Induced Breakdown Spectroscopy (LIBS), Thesis, King Saud University, 2008.

[153] A. A. Ilyin, E. B. Sokolova, S. S. Golik, O. A. Bukin, and K. A. Shmirko, J. Appl. Spectrosc. **78**, 861 (2012).

[154] F. V. Bunkin and A. M. Prokhorov, Usp. Fiz. Nauk **199**, 425 (1976).

[155] C. Phipps, M. Birkan, W. Bohn, H.-A. Eckel, H. Horisawa, T. Lippert, M. Michaelis, Y. Rezunkov, A. Sasoh, W. Schall, S. Scharring, and J. Sinko, J. Propul. Power **26**, 609 (2010).

[156] K. Franjic, Studies of Laser Ablation of Liquid Water Under Conditions of Impulsive Heat Deposition Through Vibrational Excitations (IHDVE), University of Toronto, 2010.

[157] V. S. Teslenko, Kvantovaya Elektron. (Moscow) **4**, 1732 (1977).

[158] A. Vogel, J. Noack, K. Nahen, D. Theisen, S. Busch, U. Parlitz, D. X. Hammer, G. D. Noojin, B. A. Rockwell, and R. Birngruber, Appl. Phys. B **68**, 271 (1999).

[159] E.-A. Brujan and A. Vogel, J. Fluid Mech. **558**, 281 (2006).